THE SIGNATURES OF AND FEEDBACKS BETWEEN MAGMATIC AND SURFACE PROCESSES IN VOLCANIC PROVINCES

by

DANIEL O'HARA

A DISSERTATION

Presented to the Department of Earth Sciences
and the Graduate School of the University of Oregon
in partial fulfillment of the requirements
for the degree of
Doctor of Philosophy

December 2020

DISSERTATION APPROVAL PAGE

Student: Daniel O'Hara

Title: The Signatures of and Feedbacks between Magmatic and Surface Processes in Volcanic Provinces

This dissertation has been accepted and approved in partial fulfillment of the requirements for the Doctor of Philosophy degree in the Department of Earth Sciences by:

Leif Karlstrom	Chairperson
Eugene Humphreys	Core Member
Joshua Roering	Core Member
Douglas Toomey	Core Member
Mark Fonstad	Institutional Representative

and

Kate Mondloch	Interim Vice Provost and Dean of the Graduate School

Original approval signatures are on file with the University of Oregon Graduate School.

Degree awarded December 2020

DISSERTATION ABSTRACT

Daniel O'Hara

Doctor of Philosophy

Department of Earth Sciences

December 2020

Title: The Signatures of and Feedbacks between Magmatic and Surface Processes in Volcanic Provinces

In this dissertation, I analyze the relationship between magmatic structures in the upper- to mid-crust and overlying surface topography. Beginning with a theoretical approach, I examine the impact of localized uplift perturbations associated with shallow magmatic intrusions on regional-scale landscape evolution. I find that landscape response varies from simple knickpoint generation to regional river channel reorganization and drainage divide migration. Furthermore, I determine a series of nondimensional numbers that predict transient topographic evolution. Afterwards, I expand on this framework to explore the topographic signatures of regional and long timescale crustal magmatism. Starting from an elastic deformation model of a single intrusion, I simulate the topographic impact of many stochastically-emplaced intrusions. I find that intrusion spatial distribution controls the topographic expression of magmatism and the degree of crustal thickening versus topography generation. Furthermore, I parameterize these results using a thin-plate flexure model, showing that shallower and larger intrusions cause higher surface relief consistent with an effective plate thickness that scales with mean intrusion depth. In the final chapter, I move from theory to observations and analyze the correspondence between surface and subsurface signatures of magmatism in the Cascades Arc (northwestern U.S.) by combining geological and geophysical data. Using a recently-published database of volcanic vents that erupted during the Quaternary, I derive volume estimates for 2835 edifices, and find that these volumes correspond to ~50% of total extruded volumes within the Cascades over the

last 2.6 Myr. Afterwards, I analyze the correlation between edifice volumes, vent spatial distributions, and geophysical datasets that constrain shallow- to mid-crustal structures. I find that both the number and magnitude of correlations increase when datasets are interpolated to volcanic vents. Furthermore, correlation magnitudes are highest with the most-recently active vents, and decrease through time, suggesting transient evolution of crustal magmatic structure over the last 2.6 Myr. Together, these chapters provide new insight into the ability to characterize crustal magmatic systems from topographic form and response, and are broadly applicable to volcanic provinces both on Earth and other planetary bodies.

CURRICULUM VITAE

NAME OF AUTHOR: Daniel O'Hara

GRADUATE AND UNDERGRADUATE SCHOOLS ATTENDED:

University of Oregon, Eugene OR
Indiana University of Pennsylvania, Indiana PA

DEGREES AWARDED:

Doctor of Philosophy, Earth Sciences, 2020, University of Oregon
Bachelor of Science, Geoscience, 2014, Indiana University of Pennsylvania
Bachelor of Science, Computer Science, 2014, Indiana University of Pennsylvania

AREAS OF SPECIAL INTEREST:

Landscape Evolution
Volcanic Geomorphology
Crustal Magmatism

PROFESSIONAL EXPERIENCE:

Graduate Research Assistant, University of Oregon, 2014-2020
Graduate Teaching Assistant, University of Oregon, 2016-2018
Research Assistant, Indiana University of Pennsylvania, 2010-2014

GRANTS, AWARDS, AND HONORS:

Michael H. Freilich Student Visualization Grand Prize Winner, American Geophysical Union, 2020
College of Art and Science Dissertation Fellowship, University of Oregon, 2019
Outstanding Teaching Assistant Award, University of Oregon, 2019
Research Excellence Award, University of Oregon, 2018
Graduate Research Forum First Place Poster Award, University of Oregon, 2018
Baldwin Scholarship, University of Oregon, 2015
Graduate Research Fellowship, National Science Foundation, 2014-2019
Barry M. Goldwater Scholar, Indiana University of Pennsylvania, 2013
McNair Scholar, Indiana University of Pennsylvania, 2011-2014

PUBLICATIONS:

O'Hara, D., Karlstrom, L., & Ramsey, D. W. (2020). Time-evolving surface and subsurface signatures of Quaternary volcanism in the Cascades. *Geology*, 48(11), 1088-1093. https://doi.org/10.1130/G47706.1

Lerner, A., **O'Hara, D.**, Karlstrom, L., Ebmeier, S.K., Hurwitz, S., & Anderson, K.R. (2020). The Prevalence and Significance of Offset Magma Reservoirs at Arc Volcanoes. *Geophysical Research Letters*, 47(14). https://doi.org/10.1029/2020GL087856

O'Hara, D., Karlstrom, L., & Roering, J. J. (2019). Distributed landscape response and the fragility of steady states. *Earth and Planetary Science Letters*, 506, 243-254. https://doi.org/10.1016/j.epsl.2018.11.006

Karlstrom, L., Richardson, P. W., **O'Hara, D.,** & Ebmeier, S. K. (2018). Magmatic landscape construction. *Journal of Geophysical Research: Earth Surface*. 123 (8), 1710-1730. https://doi.org/10.1029/2017JF004369

Hooft, E. E., Nomikou, P., Toomey, D. R., Lampridou, D., Getz, C., Christopoulou, M. E., **O'Hara, D.**, Arnoux, G. M., Bodmer, M., Gray, M., Heath, B. A., & VanderBeek, B. (2017). Backarc tectonism, volcanism, and mass wasting shape seafloor morphology in the Santorini-Christiana-Amorgos region of the Hellenic Volcanic Arc. *Tectonophysics*, 712, 396-414. https://doi.org/10.1016/j.tecto.2017.06.005

Lewis, J. C., **O'Hara, D. J.,** & Rau, R.-J. (2015). Seismogenic strain across the transition from fore-arc slivering to collision in southern Taiwan. Journal of *Geophysical Research: Solid Earth*, 120(6), 4539-4555. https://doi.org/10.1002/2015JB011906

ACKNOWLEDGMENTS

I would like to thank my adviser, Leif Karlstrom, as well as my committee, Eugene Humphreys, Joshua Roering, Douglas Toomey, and Mark Fonstad, for their guidance and mentorship throughout my graduate career. Similarly, I would like to thank colleague David Ramsey for mentoring me during a summer internship at the U.S.G.S., and for his contribution to Chapter IV of this dissertation. I also thank the Department of Earth Sciences administrative staff, Dave Stemple, Sandy Thoms, and Marla Trox, for their help keeping my career on track. Furthermore, I want to extend my gratitude to the department graduate students and their partners for providing an extremely helpful support network that kept my spirits high.

Outside of the UO community, I would like to thank my undergraduate professors, Katherine Farnsworth, Steven Hovan, Jonathan Lewis, Calvin Masilela, and Hilary Staples, for first inspiring me to pursue my PhD, then helping me obtain it. Additionally, I would like to thank my family members and their partners for their support throughout my academic career, including James and Bernice Glass, Daniel A. O'Hara, Debra and Robert Watson, Janice Noonan, Karen Glass, Julie Sipe, Pamela O'Hara, and Annamarie Chantel. Finally, I would like to thank friends Nate Gerber, Ellen Lamont, Jonathan Nicoloff, Tully Spring, Bobby Veneskey, Joey Weakland, and Karl Yauneridge for all their help and support over the past six years.

This dissertation was supported in part by a National Science Foundation (NSF) Graduate Research Fellowship, grant number GRF-1309047, as well as an NSF CAREER grant, 1848554, to Leif Karlstrom.

TABLE OF CONTENTS

LIST OF FIGURES

Figure Page

CHAPTER IV

LIST OF TABLES

CHAPTER I

INTRODUCTION

Volcanic landscapes encode the long-term interaction between plate tectonics, magmatism, and climate. Topography in these terrains grow through a combination of bottom-up (surface uplift associated with magmatic intrusions) and top-down (surface mantling by lava flows and eruptions) processes on timescales shorter than tectonics and erosion; generating landforms that have surface areas spanning ~9 orders of magnitude (Karlstrom et al., 2018). Studies of volcanic surfaces and underlying magmatic systems are typically completed through dense geological (e.g., Sherrod and Smith, 2000; Vanorio et al., 2005) and geophysical (e.g., Hooft et al., 2017; Janiszewski et al., 2019) surveys. However, often neglected in these analyses is the relationship between the topographic form of volcanic regions and the subsurface magmatic structure, which are generally treated as independent systems (e.g., Grosse et al., 2009; Annen et al., 2015). Thus, my research focuses on understanding the relationship between volcanic surface topography and the underlying magma plumbing systems, providing a new perspective with which to analyze and interpret volcanic regions.

My dissertation analyzes to what extent volcanic surfaces can be used to infer the spatial and temporal history of crustal magmatism. This work has partially focused on the western U.S., where Cascade arc volcanism has been active over the last 40 million years (Priest, 1990); however, the results of my research are applicable to both global and planetary volcanism studies. The main questions I explore are (1) what is the topographic signature of magma intrusions and how do such perturbations affect long-term landscape evolution, and (2) can volcanic edifice topography be used to constrain recent (< 2.6 Myr) extrusion rates and crustal magma system evolution within volcanic arcs? I employ various techniques to these answer these questions, including numerical modeling, remote sensing, and statistical analysis of synthesized datasets.

In Chapter II, I analyze the long-term landscape response to transient localized uplift perturbations associated with magmatic intrusions. Using both 1D and 2D numerical landscape evolution models, I explore surface response to perturbations of varying sizes, uplift rates, timescales, and basin positions. I find that landforms associated with this process can create disrupt topography on scales larger than the initial landform, suggesting these meso-scale (10^5 – 10^{10} m^2 planform area) features can compete with larger-scale (> 10^{10} m^2) processes, such as tectonics and climate, to control landscape development. My models show that typical landscape response to localized uplift can range from small channel knickpoint creation to channel beheading, plateau formation, and even basin-scale channel network reconfiguration. Finally, I show that landscape response can be predicted with consideration to both the initial basin conditions and the parameters of the perturbation. This defines a set of quantitative metrics that can be used to better understand landscape evolution in volcanic terrains.

Chapter III builds off of Chapter II and analyzes the topographic signatures of province-scale crustal magmatism. Using a purely elastic model for deformation associated with magma transport, I simulate topographic uplift associated with multiple generations of stochastically-emplaced magmatic intrusions within the crust. I test the effects of varying intrusion depths, sizes, and spatial distributions on surface development. I also assess the ability to estimate intrusion distributions using plate flexure analysis. I find that spatial distribution dominantly controls whether crustal magmatism contributes more to regional crustal thickening or local relief generation, with intrusion size and depth distributions determining the amount of relief generated. Furthermore, I find that spatially-dispersed intrusions can in some circumstances be approximated by a distribution of forces applied to a thin, constant-thickness elastic plate; however, spatial intrusion overlap in more clustered stochastic models limit the information that can be gained from topography alone. These results provide a baseline for understanding the relationship between topography and underlying magmatic systems.

Finally, Chapter IV explores the correspondence between volcanic edifices and the underlying crustal magmatic structure in the Cascades arc (western U.S.). Using a database of 2999 vents that have erupted in the Cascades throughout the Quaternary, I determine edifice boundaries from digital elevation models (DEMs). I then derive edifice volumes using bounded topography and generate new estimates of extruded material for the Cascades, finding that edifices likely represent ~50% of total Quaternary eruptive output. Afterwards, I combine edifice volume and vent spatial density distributions with a diverse set of geophysical data of the upper crust to analyze the correlation between datasets. I find a high degree of correlation between datasets occurring under vents throughout the arc, with the strongest correlations associated with the most-recently active vents, suggesting a transient change in the magmatic structure under the Cascades over the last 2.6 Myr. Finally, I analyze the temporal change in the spatial distribution of active vents throughout the Quaternary. I find temporal trends between localized and distributed volcanism are variable throughout the arc, highlighting the competition between crustal magmatic focusing and tectonic extension. This study presents a range of relationships that are applicable to other arcs worldwide, where geologic or geophysical data may be more scarce.

Chapter II of this dissertation was published in *Earth and Planetary Science Letters* with coauthors Leif Karlstrom and Joshua J. Roering. Chapter III was coauthored by Leif Karlstrom and Nathanial Klema. Chapter IV was published in *Geology* with coauthors Leif Karlstrom and David W. Ramsey.

CHAPTER II

DISTRIBUTED LANDSCAPE RESPONSE TO LOCALIZED UPLIFT AND THE FRAGILITY OF STEADY STATES

From O'Hara, D., Karlstrom, L., and Roering, J. J. (2019). Distributed landscape response and the fragility of steady states. Earth and Planetary Science Letters, 506, 243-254.

https://doi.org/10.1016/j.epsl.2018.11.006

1.0 Introduction

Bedrock landscapes dynamically adjust in response to environmental perturbations on timescales of thousands to millions of years (Sweetkind and Blackwell, 1989). At the core of such landscape evolution is the competition between surface uplift relative to the geoid and erosion. Landscapes are in steady state (in terms of sediment flux) when rates of uplift and erosion are equal at all points on the landscape (e.g., Whipple and Tucker, 1999). Signatures of non-steady state topography are widespread and multiscale, depending on the processes that govern uplift and erosion.

Within fluvial channels, localized convexities (knickpoints, that sometimes propagate upstream as kinematic waves, Seidl and Dietrich, 1992) record and transmit transient changes in uplift or erosion. Outside of channels, topographic adjustment occurs on hillslopes and drainage divides, and through formation of low-relief surfaces (plateaus) (Mudd and Furbish, 2005; Willett et al., 2014; Whipple et al., 2017b)

It is useful to characterize transient topography according to spatial scale. At small scales, adjustment may result from morphologic changes in soil-mantled topography caused by channel incision gradients (Mudd and Furbish, 2005), landslide thresholds (Larsen and Montgomery, 2012), or other localized processes (e.g. vegetation, climate). As spatial scale grows, the potential for transient signals to propagate from far-field sources increases: knickpoint propagation rate in fluvial channels is controlled by upstream drainage area (e.g., Lague et al., 2014); while drainage

divides migrate in response to changes in downstream lithology (Sweeney et al., 2012), faulting (Duvall and Tucker, 2015), uplift (Willett et al., 2014), and precipitation (Bonnet, 2009).

At larger scales still, transient plateaus can record either changes in uplift that generate 'relict topography' (Whipple et al., 2017a), or changes in erosion associated with channel capture and beheading (Willett et al., 2014; Yang et al., 2015). Orogen-scale signals of landscape response to perturbations can span ~ 100 km^2 areas or larger (Kirby and Whipple, 2001; Braun et al., 2013). These include drainage reorganization or channel inversion associated with tilting or subsidence (Braun et al., 2013) and channel network disequilibrium across multiple drainage basins (Willett et al., 2014). Transience suggested by differences between local and regional slopes likely extends to continental scales (Black et al., 2017).

Many landscape evolution studies have focused on response to large-scale perturbations due to tectonics (e.g., Kirby and Whipple, 2001; Willett, 2010), mantle upwelling (e.g., Braun et al., 2013), or climate (Bonnet, 2009). These processes affect multiple catchments, as seen by comparing typical perturbation areas to average Strahler-order basin areas (Figure 2.1) (Strahler, 1957; Shen et al., 2017). For example, variable tectonics affects landscape areas on the order of $\sim 10^{10} - 10^{14}$ m^2, at rates of $\sim 10^{-7} - 10^{-1}$ m/yr (Wilkinson et al., 2009).

However, not all landscape perturbations occur on large scales. Volcanism (Karlstrom et al., 2018), salt domes (Anderson et al., 1973), and landsliding (Guzzetti et al., 2009) occur on sub-catchment scales (Figure 2.1). These meso-scale perturbations are likely small compared to those from mantle upwellings or tectonics, but may have a significant impact on landscape adjustment and induce feedback mechanisms due to their effect on upstream catchments and repeated occurrences in time. Such perturbations dominate land surface uplift in long-lived ($> 1 - 10$ Myr) volcanic terrains, which occupy roughly 10% of current land area globally (Wilkinson et al., 2009).

Understanding landscape response to such meso-scale uplift perturbations motivates this study. We use magmatic landforms as a template for the uplift perturbations. For example,

laccoliths have heights ranging between $\sim 30 - 9500$ m with planform areas $\sim 0.16 - 11000$ km^2 (Figure 2.1, blue line) (Gilbert, 1877; Corry, 1988). These structures form via flexure of near surface rocks due to the emplacement of shallow magmatic sills (de Saint-Blanquat et al., 2006), which may generate local uplift rates of $\sim 1 - 10^3$ m/yr over monthly to 100 yr timescales (de Saint-Blanquat et al., 2006; Castro et al., 2016). Such perturbations are near-instantaneous compared to bedrock erosion on this spatial scale.

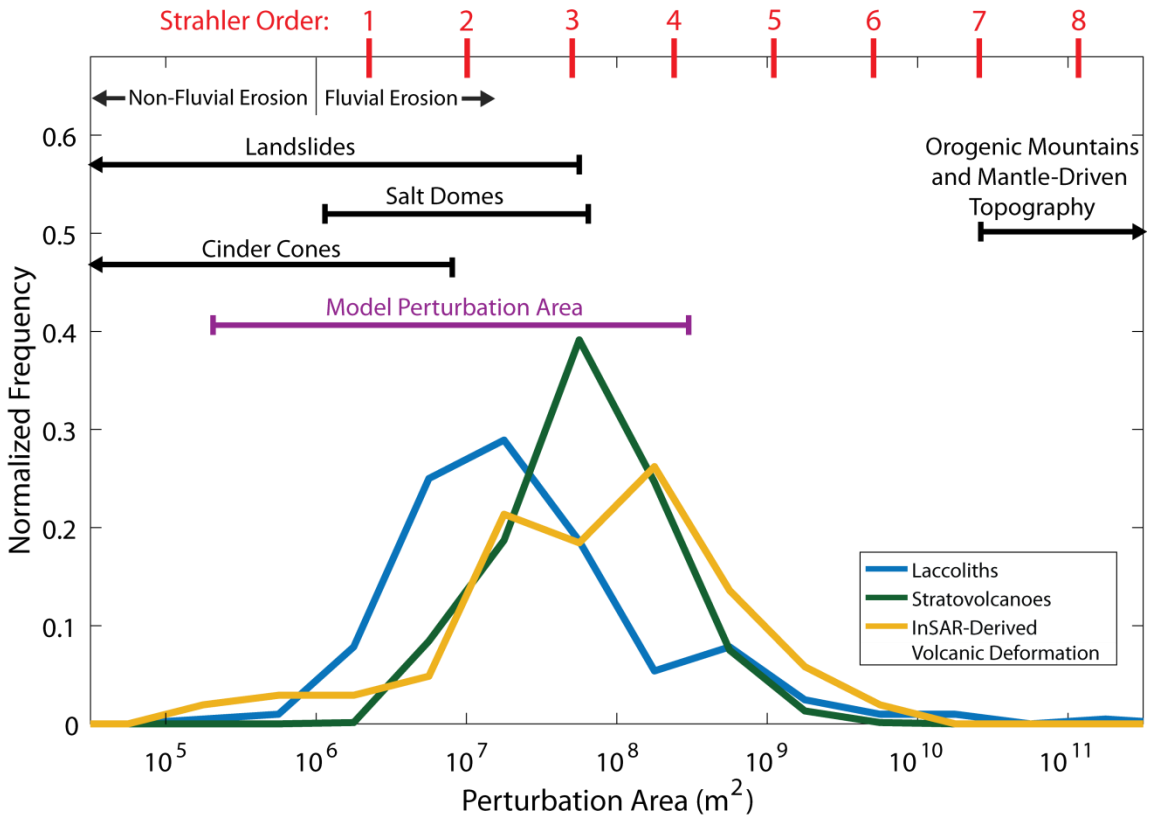

Figure 2.1 – The observed range of uplift scales on Earth, in terms of planform area. Colored lines show distributions of volcanic landform areas that represent a class of important meso-scale uplift perturbations. Black horizontal lines show ranges of other meso-scale perturbations and larger scale tectonic drivers. Sources listed in the text. Arrows indicate range continues beyond limit of the figure. Red vertical lines represent drainage basin areas of Strahler-order catchments for fluvial erosion. Purple horizontal line represents perturbation areas modeled in this study.

In what follows, we explore the response of an initially steady-state landscape to finite uplift that occurs on spatial scales smaller than a typical drainage basin. We use 1D and 2D landscape evolution models to quantify transient landscape response. We find that response can vary from simple knickpoint generation to plateau formation and basin reorganization. Upstream drainage divides adjust to uplift perturbations through lateral migration and amplification. Ridge

migration velocities are well predicted by a model that integrates downstream channel and hillslope processes.

2.0 Methods

We develop numerical landscape evolution models in stages of increasing complexity. 1D models have one steady-state solution, simplifying transient evolution (e.g., Perron and Fagherazzi, 2012). We then develop a 2D model to illustrate similarities and differences in a system with more spatial degrees of freedom. Parameters and variables are provided in Table 2.1.

Changes in surface elevations at a point in response to uplift relative to the geoid and erosion (England and Molnar, 1990) are described by

$$\frac{\partial z}{\partial t} = u - E, \tag{2.1}$$

where $z = z(x, y, t)$ is elevation, $u = u(x, y, t)$ is uplift rate, $E = E(x, y, t)$ is erosion rate, x and y are spatial coordinates, and t is time. We account for both fluvial and hillslope erosion, modeling transient ridge migration within a dominantly detachment-limited fluvial setting.

2.1 Erosion laws

Fluvial bedrock erosion occurs by abrasion and plucking, induced by shear stress acting on the channel bed, and is generally described by the semi-empirical stream power law (e.g., Whipple and Tucker, 1999):

$$E = KA^M|\nabla z|^N, \tag{2.2}$$

where erodibility coefficient $K = K(x, y, t)$ and $A = A(x, y, t)$ is upstream drainage area. M and N are empirical exponents, with $\frac{M}{N}$ often $\sim$0.5 in terrestrial landscapes (Whipple and Tucker, 1999). For simplicity we assume $N = 1$ and $M = 0.5$, although this is not observed for all landscapes (Harel et al., 2016). We further assume uniform lithology and precipitation, and thus constant erodibility $K = 10^{-6}$ m$^{1\text{-}2M}$. In many landscapes, K ranges $\sim 10^{-7} - 10^{-3}$ (Stock and Montgomery, 1999).

The formulation of equation (2.2) requires assumed relations between channel geometry (i.e. width and depth) and basin state (i.e. topology, drainage area, structural state) that are empirically-defined (Whipple and Tucker, 1999). Furthermore, use of equation (2.2) over all channelized portions of the landscape suggests river discharge is always large enough to both transport all sediment loads through the system and create shear stress in excess of that required for bedrock erosion (Whipple and Tucker, 1999). Despite its simplicity, the stream power law is prevalently used in landscape evolution models (e.g., Braun and Willett, 2013; Goren et al., 2014) and to derive metrics that define landscape disequilibrium (e.g., Kirby and Whipple, 2001; Royden and Perron, 2013; Willett et al., 2014). Thus, equation (2.2) permits exploration of localized perturbations on landscape scale without appealing to complex erosion mechanics that are under development and require challenging parameterization.

We assume soil-mantled hillslopes with gentle enough slopes that landsliding does not occur, requiring soil production rates to be in equilibrium with erosion (Roering et al., 2001). Downhill sediment flux through soil creep $\vec{q} = \vec{q}(x, y, t)$ is governed by the negative product of local slope and a diffusivity coefficient $D = D(x, y, t)$:

$$\vec{q} = -D\nabla z, \tag{2.3}$$

D is typically in the range of $\sim 10^{-4} - 10^{-1}$ m^2/yr (Hurst et al., 2013). We assume constant diffusivity (10^{-2} m^2/yr) and linear dependence of soil flux on slope,

$$E = \nabla \cdot \vec{q} = -D\nabla^2 z. \tag{2.4}$$

The assumption of a linear flux model is not ideally suited for rapidly uplifting tectonic settings, where hillslopes are better modeled using a non-linear flux relation (e.g., Roering et al., 2001; Mudd and Furbish, 2005). The distinction between these models is changes in hillslope relief, signal propagation speed, and sediment load entering rivers. However, we justify this simplification as 1) overall landscape relief and response time are predominately set by fluvial erosion, 2) the stream power law, as used, does not include a sediment flux term, negating the

influence of hillslope sediment delivery on channel incision, and 3) the linear flux model has a simple analytic solution which keeps model results and analysis tractable.

Symbol Definitions			
Var.	Description	Var.	Description
Model Parameters			
A	Drainage area (m^2)	M	Stream power drainage area exponent
A_0	Reference drainage area for χ (m^2)	N	Stream power slope exponent
α	Characteristic drainage area scale (m^2)	q	Hillslope sediment flux (m^2/yr)
B_F	Boolean basin pixel values for final state	R_P	Perturbation radius (m)
B_I	Boolean basin pixel values for initial state	u_0	Background uplift rate (m/yr)
C_{diff}	Speed of hillslope diffusion (m/yr)	u_P	Maximum perturbation uplift rate (m/yr)
C_I	Channel advection speed (m/yr)	X	Characteristic horizontal length scale (m)
C_R	Ridge migration speed (m/yr)	x_c	Critical drainage length for fluvial incision (m)
χ	Scaled upstream distance	x_H	Hack's Law distance from divide to perturbation center (m)
D	Soil diffusivity (m^2/yr)	x_L	Basin length (m)
E	Landscape erosion rate (m/yr)	x_P, y_P	Perturbation center coordinates (m)
H	Hack's Law exponent	x_Z	Location of maximum perturbed topography at $t = t_P$ (m)
h_0	Reference elevation for χ (m)	Z	Characteristic vertical length scale (m)
K	Stream power coefficient (m^{1-2M}/yr)	z_0	Initial landscape elevation (m)
k_a	Hack's Law coefficient (m^{2-H})	Z_A	Divide elevation in excess of steady state (m)
L_D	2D model affected drainage divide length (m)	z_b	Base level elevation (m)
L_M	Model divide migration distance (m)	z_P	Elevation of maximum perturbed topography at $t = t_P$ (m)
Nondimensional Parameters			
β	Nondimensional ratio comparing perturbation and initial local relief	J	Jaccard similarity index
d_B	Basin Jaccard distance	Φ_A	Nondimensional divide amplification
d_t	Transient topographic distance	Ψ_D	Nondimensional affected divide length
η	Nondimensional ratio comparing advection wavespeeds	Ψ_M	Nondimensional divide migration distance
γ	Nondimensional ratio comparing perturbed uplift and hillslope diffusion timescales	τ_{SS}	Nondimensional time to steady state
Timescales			
T_{C_I}	Channel advection timescale (yr)	T_{SS}	1D model time to steady state (yr)
T_{C_R}	Ridge migration timescale (yr)	T_W	Erosive wave timescale from local minimum to perturbation top (yr)
T_D	Hillslope diffusion timescale (yr)	T_{X_P}	Characteristic timescale for steady state (yr)
t_P	Uplift perturbation timescale (yr)		
Variables			
r	Radial distance from perturbation center (m)	x, y	Spatial coordinates (m)
t	Time (yr)	z	Landscape elevation (m)
Numerical Parameters			
Δt	Model timestep (yr)	j	Model temporal index
Δx	Model grid spacing (m)	λ	Diffusion discretization coefficient
g	Model spatial index	N_G	Total number of model gridpoints
G	Number of model basin gridpoints	ξ	Advection discretization coefficient
G_C	Model index corresponding to x_c		

Table 2.1 – Summary of parameters and variables.

2.2 Localized uplift

We model transient, localized uplift by parameterizing flexural solutions to thin-plate elasticity (Pollard and Johnson, 1973), mimicking structures seen in laccoliths (Corry, 1988). We assume

$$u(x,y,t) = \begin{cases} u_0 + u_P\left(1 - \left(\frac{r(x,y)}{R_P}\right)^2\right), & r \le R_P, \text{and } 0 < t \le t_P \\ u_0, & \text{else} \end{cases}, \tag{2.5}$$

in which $r(x,y) = \sqrt{(x - x_P)^2 + (y - y_P)^2}$ is radial distance from the perturbation center (x_P, y_P), u_0 is background uplift (10^{-4} m/yr), R_P is perturbation radius, u_P is maximum perturbation uplift rate, and t_P is total perturbation uplift time. When $t > t_P$, u_0 is uniform over the entire landscape. In all models, we assume that localized uplift is confined to one basin and does not overlap spatially with initial drainage divides. This assumption is not valid in all situations of localized uplift, but allows for a simplified geometry with which to systematically track perturbation effects.

Combining (1), (2), (4), and (5) thus gives the landscape evolution equation

$$\frac{\partial z}{\partial t} = u - C_I|\nabla z| + D\nabla^2 z, \tag{2.6}$$

an advection-diffusion equation characterized by spatially variable wavespeed

$$C_I(x,y,t) = KA(x,y,t)^M. \tag{2.7}$$

We assume the advective term is active only in fluvial channels and the diffusive term only on hillslopes, as defined by a critical drainage length (Whipple and Tucker, 1999). Our use of $M = 0.5$ and $N = 1$ is a simplification that is not observed in all landscapes, as Harel et al. (2016) suggest most environments may have a mean slope exponent value greater than 1. Using an N value greater than 1 alters advection wavespeed, influencing landscape adjustment timescales (Whipple and Tucker, 1999), and introduces a dependency of erosion rate on drainage

density (Tucker and Bras, 1998). However, our use of $N = 1$ provides a simplified quantitative approach to analyze and explain regional landscape response to meso-scale perturbations.

2.3 1D Model

To build intuition we first analyze transient uplift in one dimension. We relate drainage area to basin length using Hack's Law (Hack, 1957),

$$A = k_a x^H. \tag{2.8}$$

k_a and H are Hack's coefficient and exponent, respectively, and x here represents the distance from the upstream drainage divide. For simplicity, we use $k_a = 0.57$ m$^{2\text{-}H}$ and $H = 1.67$ (Hack, 1957), implying a dendritic river system; however, these parameters likely depend on local erosion mechanics that define basin topology.

We assume a model domain of length 60 km and grid resolution 50 m, with both ends of the domain fixed at base level z_b. This implies a single steady-state solution with two catchments separated by a divide, which has an analytic solution (Figure 2.2.A). We define the critical drainage length, x_c, as the inflection point between convex fluvial channels and concave hillslopes in steady state (e.g., Perron et al., 2009),

$$x_c = \left(\frac{D}{K(k_a)^M}\right)^{\frac{1}{1+HM}}. \tag{2.9}$$

Localized uplift sometimes generates secondary drainage divides and associated local minima (where down-slope topography converges). We assume local minima are associated with internally-drained basins and do not erode, uplifting at the background rate. Uplift continues until the internally-drained basin is the same elevation as one of the surrounding divides, at which point the divide is captured by its neighboring basin. This method of allowing local minima to act as transient features is qualitatively similar to previous models (Willett, 2010) that assumed sediment deposition fills local minima.

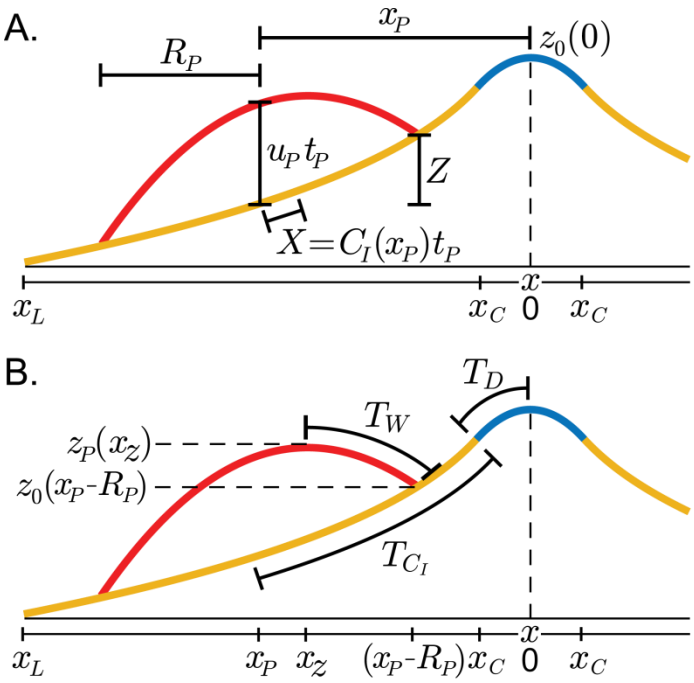

Figure 2.2 – 1D Model setup and symbol definition. **A:** Initial steady-state topography with only one drainage divide (blue and yellow lines), and perturbed topography (red line). Horizontal axis is the local spatial coordinate system. Blue line represents the domain where hillslope processes dominate (bounded by critical drainage length $\boldsymbol{x_c}$), yellow lines represent fluvial domain. Parameters listed are geometric scales for equation (2.13). **B:** Same topography as A, illustrating the geometry of how timescales described in equations (2.17), (2.18), and (2.20) are calculated.

2.3.1 Numerical Formulation

In 1D, we solve the landscape evolution equation (2.6) using a backwards-time, backwards-space and backwards-time, centered-space scheme for the advection and diffusion components, respectively. Using the subscripts g and j for spatial and temporal indices, and defining Δx and Δt as grid spacing and timestep, respectively, the discrete advection and diffusion components of equation (2.6) are

$$z_{g,j-1} + u_{g,j}\Delta t = \left(1 + \xi x_{g,j-1}^{HM}\right) z_{g,j} - \xi x_{g,j-1}^{HM} z_{g+1,j} \quad (2.10a)$$

$$z_{g,j-1} + u_{g,j}\Delta t = z_{g,j}(1 + 2\lambda) - \lambda z_{g-1,j} - \lambda z_{g+1,j}, \quad (2.10b)$$

with $\xi = K k_a^M \Delta t / \Delta x$ and $\lambda = D\Delta t / \Delta x^2$.

We split the global domain, with $N_G = 1201$ total gridpoints, into smaller basin subdomains to calculate erosion. Within the basin domain $g = 0, \Delta x, \ldots, (G-1)\Delta x, G\Delta x$, where $g = 0$ is the divide location and $G < N_G$ is total number of gridpoints in the basin, equation (2.10a) is valid on the interval $g = G_c\Delta x, (G_c + 1)\Delta x, \ldots, G\Delta x$ and (10b) is valid for $g = 0, \Delta x, \ldots, (G_c - 1)\Delta x$, where G_c is the index corresponding to x at critical drainage length x_c.

Boundary conditions for equation (2.10a) are determined by the location of the local channel base level at the outlet of the basin. If the base level is located at one of the model domain edges, a Dirichlet boundary condition is used. If the channel base is not at a model domain edge (i.e., it is a local minimum), slope, and thus erosion, is assumed to be zero (a Neumann boundary condition), such that the node's elevation increases by the background uplift rate. Together, equation (2.10) and accompanying boundary conditions are solved numerically as a system of linear equations for the vector of unknown elevations $\overrightarrow{z_J}$ at each timestep. Hillslope domains are always bounded by channel nodes, such that typical Neumann boundary conditions for the diffusion component at G_c are not needed.

2.3.2 Numerical Convergence

We assess the model rate of numerical convergence using a scenario of transient background uplift. Starting with the analytic topographic solution of landscape evolution, defined as (Whipple and Tucker, 1999)

$$z(x \geq x_c) = z_b + \frac{u_0(x_L^{1-HM} - x^{1-HM})}{Kk_a^M(1-HM)} \tag{2.11a}$$

$$z(x < x_c) = z_b + \frac{u_0(x_L^{1-HM} - x_c^{1-HM})}{Kk_a^M(1-HM)} + \frac{u_0(x_c^2 - x^2)}{2D}, \tag{2.11b}$$

the background uplift rate is increased by one order of magnitude and the model is allowed to evolve back to steady state. We then compare the numerical solution to the analytic solution for the new uplift rate at a single channel node $x = 300$ m. Comparing models of resolution $\Delta x = 25, 50, 100$ m, we find the error converges linearly at a rate of approximately 1 (Figure 2.3.A), as expected for a first-order finite-difference scheme, although we are not testing spatial and temporal convergence independently with this approach.

Finally, although the configuration of the 1D model forces the steady-state topography to be symmetric with the divide in the center of the domain, numerical error limits the ability of the divide to migrate to the true analytic steady state position. Δx determines how close the model

can get to symmetric basins, although larger x_c at fixed Δx results in closer numerical approximation to the analytic divide position (Figure 2.3.B).

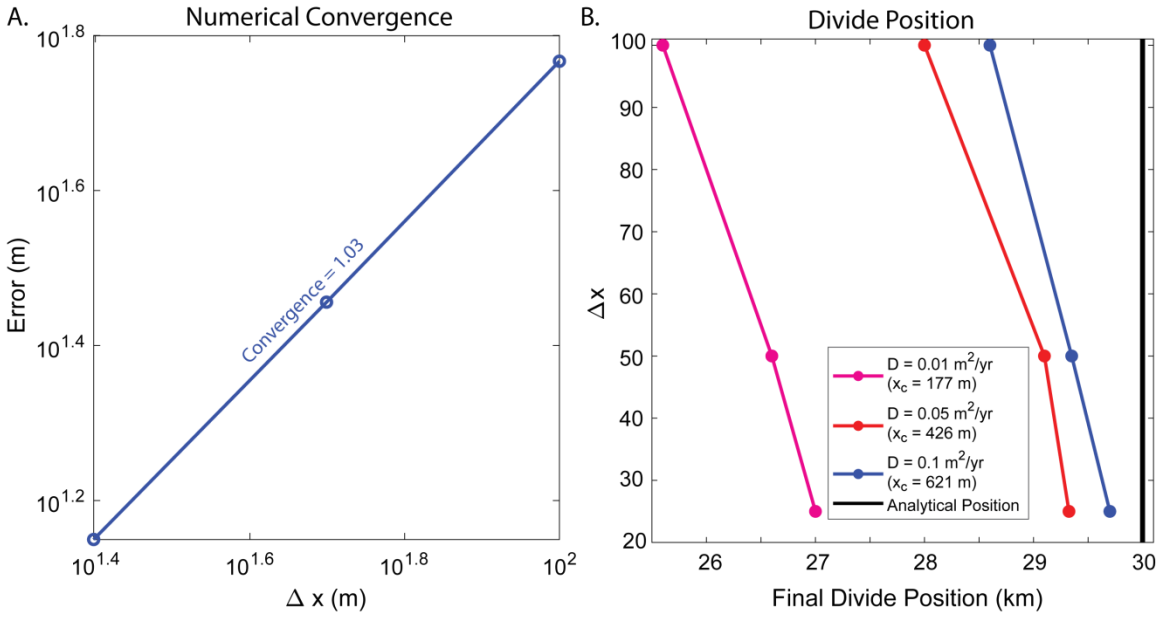

Figure 2.3 – **A:** 1D model convergence rate of the advection component for grid spacing $\boldsymbol{\Delta x = 25, 50, 100}$ m. **B:** 1D model final position for same grid spacing as A and soil soil diffusivity $\boldsymbol{D = 0.01, 0.05, 0.1}$ m^2/yr.

2.4 2D Model

We model landscape response in 2D using FastScape (Braun and Willett, 2013), which solves equation (2.6) using an implicit finite difference scheme for fluvial and hillslope erosion. The landscape is modeled on a grid of length 60 km and resolution 150 m in both x and y with base level defined as points centered on each grid boundary face, creating four basins in steady state. Initial steady-state is found by uplifting flat topography at u_0 until mean topography is constant in time. Similar to 1D, we allow local minima to act as internally-drained basins.

2.5 Non-dimensionalization and transient response metrics

We nondimensionalize equation (2.6) as

$$t = t_P t^*, \quad u = u_P u^*, \quad x = X x^*, \quad y = Y y^*, \\ A = \alpha A^*, \quad z = Z z^*, \tag{2.12}$$

where stars indicate dimensionless variables. Characteristic scales are defined by the perturbation maximum uplift rate (u_P) and timescale (t_P); $X = C_I(x_P, y_P)t_P$, distance upstream of the

perturbation center calculated using the steady-state wavespeed implied by equation (2.7) evaluated at (x_P, y_P) (Figure 2.2.A); $\alpha = k_a(R_P)^H$, local drainage area on the perturbation given by Hack's Law. Z is defined as initial local relief between the center and upstream edge of the perturbation (Figure 2.2.A). In 1D, this is

$$Z = \frac{u_0((x_P)^{1-HM} - (x_P - R_P)^{1-HM})}{K(k_a)^M(1 - HM)}. \tag{2.13}$$

In 2D multiple channels and subcatchments may exist within the perturbed region, so we take this value as the relief of the highest-order channel within the constraints of the perturbation.

Substituting (12) into (6) and rearranging gives

$$\frac{\partial z^*}{\partial t^*} = \beta u^* - \eta A^{*M}|\nabla z^*| + \gamma \nabla^2 z^*, \tag{2.14}$$

where

$$\beta = \frac{u_P t_P}{Z}, \quad \eta = \frac{K\alpha^M t_P}{X} = \frac{C_I(R_P)}{C_I(x_P, y_P)} = \left(\frac{R_P}{x_P}\right)^{HM}, \quad \gamma = \frac{D t_P}{X^2}. \tag{2.15}$$

Nondimensional control parameters in equation (2.15) are simply interpreted: β compares perturbation relief to initial local relief. η is a ratio of channel wave velocities, comparing drainage area of the perturbation with that of the initial channel. γ compares perturbation uplift timescale to the hillslope diffusion timescale X^2/D.

3.0 Results

We analyze landscape transient response using a series of metrics and a grid search over u_P, t_P, R_P, x_P, and y_P, keeping all other parameters constant. Parameter ranges are defined by laccolith spatial scales and uplift rates (Figure 2.1, purple line) (Corry, 1988; de Saint-Blanquat et al., 2006). Variable model perturbation parameters are listed in Table 2.2. In total, we run 10347 1D and 25 2D models.

1D Model Parameters	
Parameter	Values
x_P	[0.63, 1.22, 1.67, 2.00, 2.25, 2.44, 2.58, 2.68, 2.76, 2.82, 2.87, 2.90] $\times 10^4$ m
R_P	[316, 562, 1000, 1778, 3162, 5623, 10000] m
u_P	[0.010, 0.018, 0.032, 0.056, 0.100, 0.178, 0.316, 0.562, 1.00, 1.78, 3.16, 5.62, 10.0] m/yr
t_P	[40, 60, 100, 180, 320, 570, 1000] yr
2D Model Parameters	
Parameter	Values
x_P	[30000, 30750] m
y_P	[47700, 56550] m
R_P	[500, 1500, 5000, 10000] m
u_P	[0.001, 0.003, 0.005, 0.01, 0.03, 0.05, 0.1, 0.3, 0.5, 1, 3, 5] m/yr
t_P	1000 yr

Table 2.2 – Variable parameters used in the 1D and 2D model grid search.

We focus specifically on the $\beta - \eta$ parameter space, as little variation is observed with γ for the assumed hillslope parameters. This does not imply that hillslopes are not important, as we will demonstrate. Within the $\beta - \eta$ space, higher perturbation uplift rates (u_P) and timescales (t_P) correspond to higher β values, and perturbations closer to the basin mouth (higher x_P) or lower perturbation sizes (R_P) correspond to both higher β and lower η values (Figure 2.4.A).

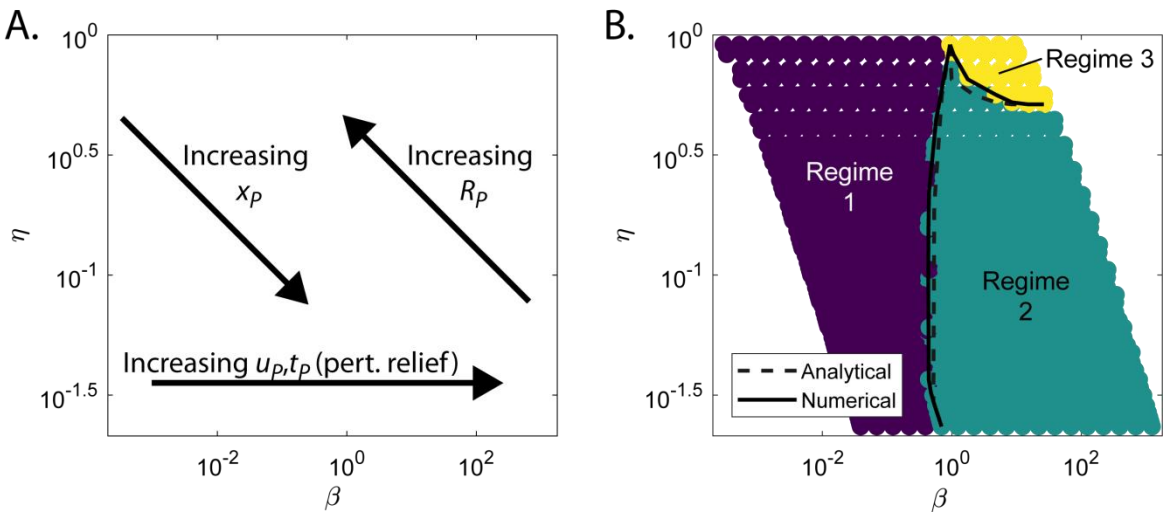

Figure 2.4 – A: Nondimensional space showing how dimensional perturbation parameters affect dimensionless numbers $\boldsymbol{\eta}$ and $\boldsymbol{\beta}$. **B:** Grid search results showing model regimes defined in the text and described in Figure 2.5. Solid black lines indicate regime boundaries. Dashed black lines show regime boundaries determined analytically, as described in the text.

3.1 1D Models

Three regimes of transient landscape behavior are observed in 1D (Figure 2.5):

Regime 1, No ridge formation (Figure 2.5.A): The perturbation creates positive topography on the landscape that is lower in relief than the initial upstream channel, and advects upstream as a knickpoint. Upon reaching the divide, the knickpoint perturbs the divide by amplifying topography and inducing lateral divide migration towards the perturbed basin. The divide then returns to its pre-perturbation steady-state position.

Regime 2, Initial topography dominates (Figure 2.5.B): The perturbation forms a new ridge and local minimum in the previously upstream channel. The local minimum is erosion-deficient and uplifts as a plateau, while headward erosion propagates upstream on both sides of the perturbation in response to channel length change. After localized uplift has stopped, the perturbation uplifts at background rate u_0 until headward erosion reaches the new ridge and erodes it. Erosion continues until the perturbation and adjoining plateau have equal elevation and the perturbation becomes captured by the initial divide. Upon capture, the plateau erodes via headward erosion. The amount of divide amplification and migration is increased compared to Regime 1.

Regime 3, Perturbation dominates (Figure 2.5.C): Similar to Regime 2, the perturbation forms a new ridge and upstream local minimum that uplifts as a plateau. However, headward erosion is unable to degrade the ridge before the plateau reaches the same elevation as the initial divide. The perturbation captures the initial ridge, forming a knickpoint that migrates towards the perturbation and amplifies it. The divide then migrates back to the center of the domain.

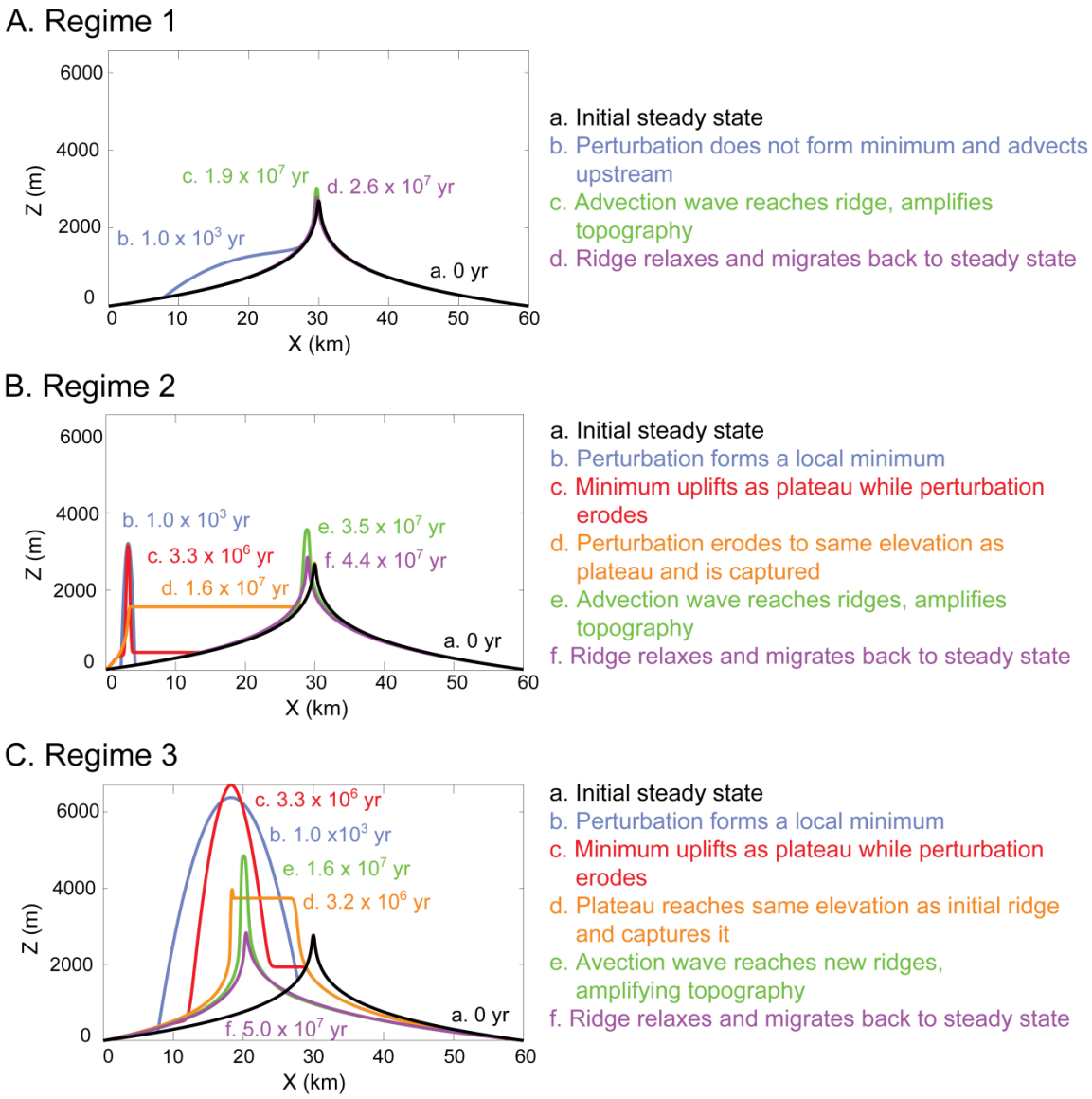

Figure 2.5 – Transient behavior defining the three regimes observed in 1D models. Panels show model topography, with colored lines for model times associated with significant events and associated text.

Model behaviors classified above cleanly separate in $\beta - \eta$ space (Figure 2.4.B). In general, the perturbation forms a new ridge when $\beta > \sim 1$, which can be understood from geometry: transition out of Regime 1 requires the maximum elevation of the perturbation on the landscape to be larger than the elevation of the initial channel at the upstream edge of the perturbation:

$$z_P(x_Z) > z_0(x_P - R_P), \tag{2.16}$$

where $z_P(x_Z)$ is the elevation and location of the highest perturbed topography (Figure 2.2.B)

$$z_P(x_Z) = \max[z_0(x) + u(x, t_P)t_P], \quad x_P - R_P \leq x \leq x_P. \tag{2.17}$$

The perturbation dominates for large β and η. Transition from Regime 2 to Regime 3 can be predicted analytically by comparing the initial divide elevation to the maximum amount of background uplift during the time taken for a wave to travel from the local minimum to the perturbation peak. Regime 2 occurs if

$$z_0(0) > z_0(x_P - R_P) + u_0 T_W, \tag{2.18}$$

where T_W is the erosive signal transit time from the local minimum to the top of the perturbation (Figure 2.2.B):

$$\begin{aligned} T_W &= \int_{R_P + x_Z - x_P}^{x_c} \frac{dx}{C_I(x)} + T_D \\ &= \frac{(R_P + x_Z - x_P)^{1-HM} - (x_c)^{1-HM}}{k(k_a)^M(1-HM)}, \end{aligned} \tag{2.19}$$

and T_D is the hillslope diffusion timescale (Figure 2.2.B)

$$T_D = \frac{(x_c)^2}{D}. \tag{2.20}$$

Regime transitions predicted by these analytic values compare well with numerical model results (Figure 2.4.B, dashed lines). Discrepancies between analytic and numerical regime boundaries are attributed both to neglecting erosion in the analytic predictions and the spatial grid resolution of the numerical models (Figure 2.3).

3.1.1 Time to steady state

We assume the landscape is in steady state when topography does not change in time, which is also a steady state in sediment flux in our model (Willett and Brandon, 2002). Time until the profile reestablishes steady state is a predictive metric for transient response. It has been

proposed that the transit time of advective kinematic waves in (6) controls this timescale (Whipple and Tucker, 1999; Royden and Perron, 2013).

However, in our simulations, kinematic wave transit competes with drainage divide migration, at speed $C_R(t)$, to set the timescale of landscape adjustment. We compute the time to steady state (T_{SS}) numerically as the time elapsed between $t = 0$ and when the primary drainage divide has migrated to within a small fraction of the initial position. We then compare T_{SS} with a characteristic erosion time after any local minima have eroded, defined by

$$T_{x_P} = \max\left(T_{C_R}, T_{C_I}\right), \tag{2.21}$$

where T_{C_R} is the ridge migration timescale and T_{C_I} is the advection time between the perturbation center and channel head of the initial divide (Figure 2.2.B)

$$T_{C_I} = \int_{x_P}^{x_c} \frac{dx}{C_I(x)}. \tag{2.22}$$

T_{C_R} is computed numerically as the time between when any local minima have eroded and when the ridge is at its final steady-state position. Because Regime 1 does not involve local minima formation, T_{C_R} is zero according to this definition (although some ridge migration does occur). Nondimensional time to steady state is then $\tau_{SS} = T_{SS}/T_{x_P}$, near unity if either channel or ridge transit time approaches T_{SS}.

We find this scaling explains the three transient regimes in our 1D simulations (Figure 2.6.A). In Regime 1, $\tau_{SS} \approx 1$, as the steady-state timescale is controlled by T_{C_I}. In Regime 2, steady state is still dominantly controlled by T_{C_I}, but τ_{SS} increases beyond 1 with increasing β and η as T_{C_R} begins influencing response time. As η increases in Regime 2, γ also begins influencing time to steady state with lower γ causing T_{C_R} to sometimes become the dominant timescale (hatched zone of Figure 2.6.A). In Regime 3, divide migration is slow compared to channel adjustment and so again $\tau_{SS} \approx 1$, but here T_{C_R} dominates response.

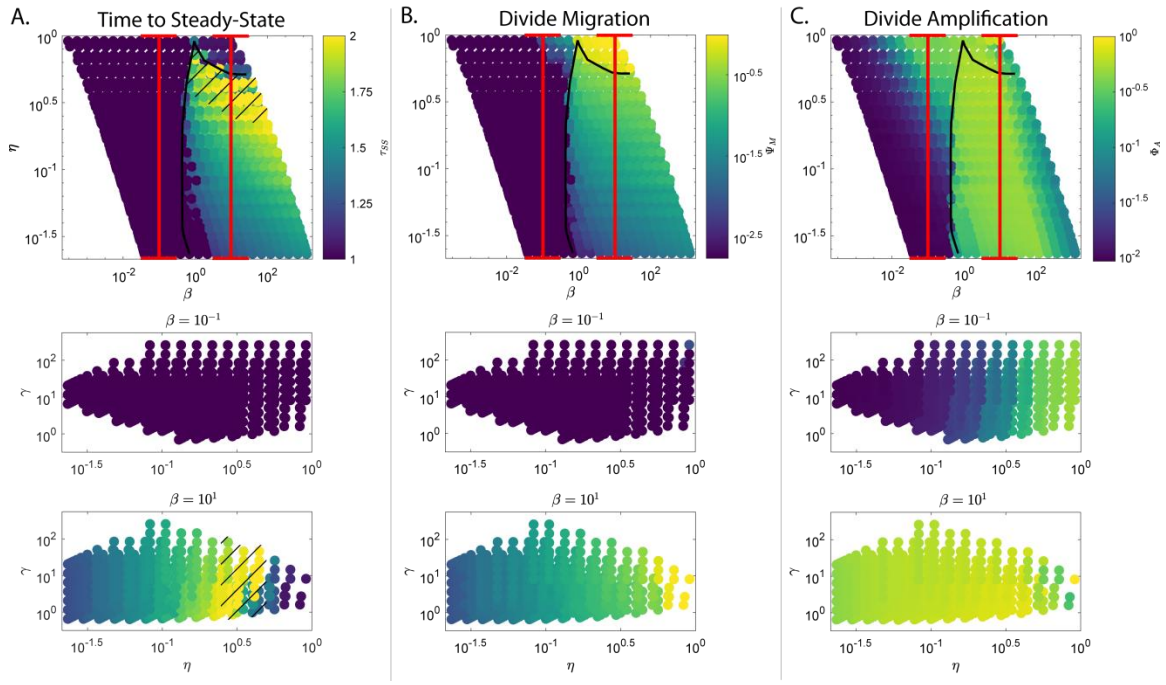

Figure 2.6 – 1D model regime diagrams as in Figure 2.4, with colors corresponding to nondimensional metrics defined in text. Black lines in upper panels show model regime boundaries. Lower panels show $\boldsymbol{\eta - \gamma}$ cross-sections of the nondimensional parameter space for $\boldsymbol{\beta = 10^{-1}}$ (middle panels) and $\boldsymbol{\beta = 10^{1}}$ (bottom panels), corresponding to red lines of upper panels. **A:** Time to steady state, scaled by the longest of channel advection or ridge migration timescales ($\boldsymbol{\tau_{SS}}$). Hatched zone represents models in Regime 2 where divide migration becomes dominant timescale. **B:** Maximum ridge migration from steady state scaled by perturbation center location within the basin ($\boldsymbol{\Psi_M}$. **C:** Maximum ridge amplification relative to steady state scaled by the maximum model topographic deviation from steady state through time ($\boldsymbol{\Phi_A}$).

Whipple et al. (2017b) suggests the ratio of divide migration timescale (T_{C_R}) compared to channel knickpoint advection timescale (T_{C_I}) influences landscape behavior. Within our models, this ratio determines the scaling for steady state timescales, and whether the initial topography (Regime 2) or perturbation (Regime 3) dominate the transient response (Figure 2.7). In general, Regime 2 has low (< 1) T_{C_R}/T_{C_I} ratios as the knickpoint transit time is the dominant timescale (Figure 2.7). The divide migration number increases with larger η and lower γ values as perturbation size, position, and timescale begin generating response controlled by divide migration. Near the Regime 2-3 boundary, T_{C_R}/T_{C_I} may be less than or greater than unity (hatched zone), such that perturbations cause large enough topographic disruption that divide migration becomes the dominant timescale, even if the initial topography is the dominant

landform. Regime 3 represents the highest divide migration numbers and is thus dominated by T_{C_R}.

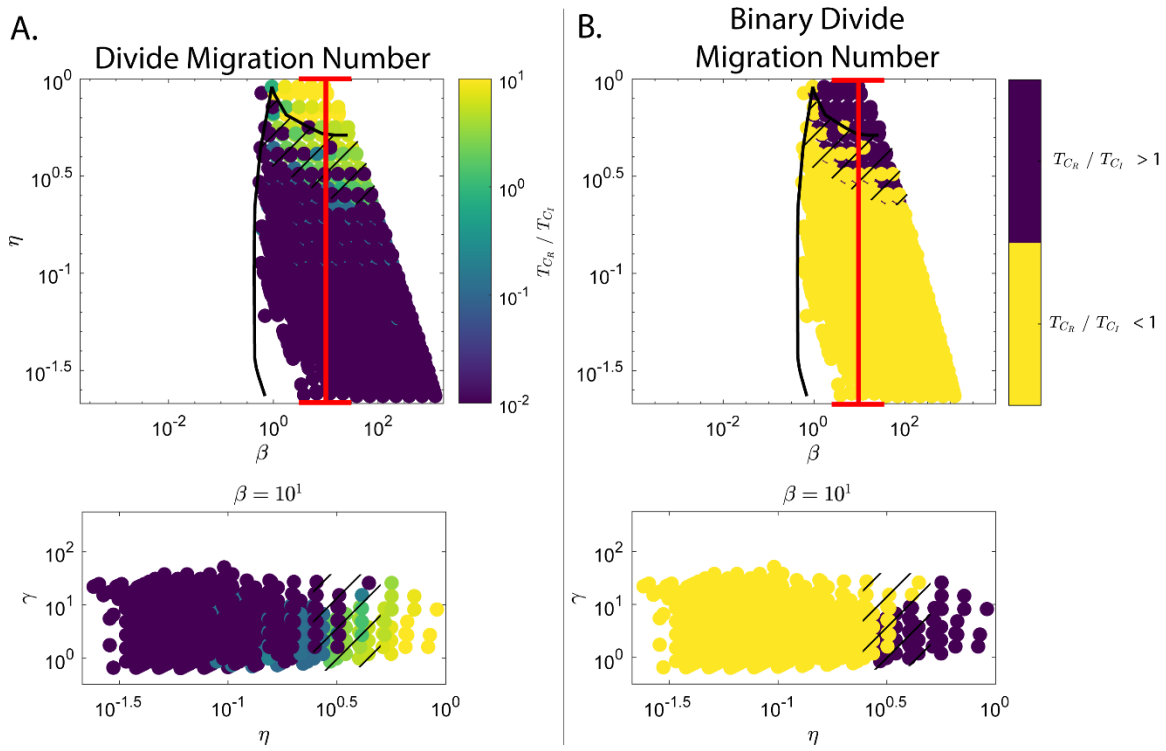

Figure 2.7 – Ratios of divide migration to advection timescales ('Divide Migration Number'; Whipple et al., 2017b) within the $\boldsymbol{\beta - \eta}$ space (top panels) and through an $\boldsymbol{\eta - \gamma}$ cross-section at $\boldsymbol{\beta = 10^1}$ (bottom panels). Hatching represents 'transition zone' in Regime 2 where divide migration bcomes the dominant timescale. **A:** Raw divide migration numbers. **B:** Binary values for the divide migration numbers less than or greater than 1.

3.1.2 Maximum divide migration

Uplift perturbations induce transient lateral response of the initial drainage divide. We define the maximum amount of divide migration (L_M) by the difference between the maximum length of the unperturbed basin and the initial basin length. We scale this value by the perturbation center location

$$\Psi_M = \frac{L_M}{x_P}, \tag{2.23}$$

as this represents the maximum horizontal distance the divide can be perturbed.

In all regimes, higher β and η correspond to higher Ψ_M, with a distinct break occurring at the Regime 1 boundary (Figure 2.6.B). In Regime 1, divide migration is negligible compared to

perturbation position for all except the highest β and η. Mudd and Furbish (2005) analyzed this behavior in detail to show differences in channel incision across hillslopes cause the divide to migrate toward lower erosion rates. Here, the concave knickpoint induces lower slopes as it propagates to the hillcrest, thus lowering local erosion rates of the perturbed basin and causing the divide to migrate towards the perturbation.

Regime 2 exhibits larger degrees of ridge migration, and shows the tradeoff between perturbation relief, size, and position in affecting the ridge. η can be approximated as $R_P \,/\, x_P$, such that low η values represent small perturbations near the channel base. In such scenarios, even if a perturbation creates large relief (high β), its proximity to base level means that headward erosion reaches the ridge before the upstream plateau reaches the initial divide. As η increases in Regime 2, plateaus that capture the perturbation have higher relief. Higher relief of the upstream channel, and larger amount of time needed to erode the perturbation after it initially uplifts, result in larger divide migration (Mudd and Furbish, 2005).

Regime 3 corresponds to perturbations that have sizes approximately equal to the distance from divide ($\eta \approx 1$). Although these perturbations have the largest amounts of scaled ridge disruption, Ψ_M is less than 1 such that the maximum transient divide position never corresponds to the location of maximum uplift. This results from the initial channel topography, which offsets maximum perturbed topography from the perturbation center (x_Z in equation 2.19).

3.1.3 Maximum divide amplification

Uplift perturbations also drive transient amplification of drainage divide elevations when the perturbation signal propagates up channels to the divide. We quantify vertical divide disruption by measuring the maximum amount of divide amplification (Z_A) compared to the maximum topographic deviation from steady state anywhere within the profile at any time

$$\Phi_A = \frac{Z_A}{\max(|z(x,0) - z(x,t)|)}. \tag{2.24}$$

Vertical disruption is not monotonic with β and η (Figure 2.6.C). In Regime 1, although the channel response is limited to knickpoint propagation, perturbations induce increasing ridge amplification with higher β and η. Perturbations that form higher relief and occur closer to the divide produce larger transient signals that persist as they propagate upstream (Mudd and Furbish, 2005).

A clear increase in $\Phi_A$occurs at the Regime 1 boundary, but Regime 2 and 3 are indistinguishable. Rather, increasing β results in decreasing Φ_A. This zone of Φ_A, which is largely independent of η, is controlled by the amount of relief, relative to the perturbation, that the uplifting plateau can generate before its adjacent ridge is captured and it is propagated upstream as a knickpoint to the dominant divide. For $\beta \approx 10^1$, the uplifting plateau captures the perturbation by generating a higher-relief landform than the initial perturbation relief ($u_P t_P$). Conversely, for $\beta > \sim 10^2$, the incision wave associated with channel beheading is able to propagate from base level to the initially high-relief perturbation and erode it before the plateau uplifts to the height of the ridge, thus forming a relatively lower-relief knickpoint compared to the perturbation relief. This metric thus distinguishes whether the perturbation or the subsequent basin disruption is the dominant feature that drives divide transience

3.2 2D Models

In real landscapes, localized uplift is observed to generate lateral channel migration (Perkins et al., 2016a) and spatially variable ridge migration (Willett et al., 2014). Such complex behavior is not possible in 1D, but can arise in 2D models.

We do not attempt a complete characterization of transient response to localized uplift in 2D, but use a coarse grid search to demonstrate that 2D models exhibit broadly similar transient landscape adjustment to localized uplift as 1D models. Models with low β and η generate negligible landscape response. As β and η increase, disruption magnitude also increases.

However, there is also significant additional complexity in 2D, due to the additional spatial degree of freedom.

Most significant transient adjustments to localized uplift are spatially anisotropic (Figure 2.8). Model channels with high drainage areas, although initially beheaded by the perturbation, often retain their original configuration in the new steady state (Whipple et al., 2017a). Low drainage area channels, however, are influenced by the perturbation and reorganize to form radial drainages that persist into the new steady state. We do not attempt to constrain pre-existing channel sizes that remain stable to perturbations, as numerical landscape evolution models are known to be more stable to lateral channel migration than real landscapes (Goren et al., 2014).

Plateaus form upstream of the perturbation in response to channel beheading, mechanistically similar to that proposed to occur by tectonically-driven stream capture (Yang et al., 2015). Finally, ridge migration is spatially localized upstream from the perturbation (Figure 2.8). All models that experience basin adjustment do not evolve back to the initial network geometry, but adopt a new configuration of channels and ridges which balance background uplift and erosion everywhere.

3.2.1 Fragility of steady-state solutions in 2D

Occurrence of different steady-state solutions before and after transient uplift suggests that 2D topographic steady states are unstable to sufficiently large perturbations. Drainage divide response demonstrates a systematic metric of change. We measure the maximum amount of divide migration (L_M) and the affected initial divide length (L_D) at initial and final steady state by calculating the Euclidean distance between every point of the longest continuously differing divide sections (Figure 2.9.A). L_M is defined as the maximum distance between nearest neighbor points in initial versus final steady state (Figure 2.9.A, solid red line). L_D is calculated as the summed Euclidean distance along the initial, unmatched divide section (Figure 2.9.A, dashed red line). Both metrics are nondimensionalized by the Hack's Law distance ($x_H = (A(x_P, y_P)/$

$k_a)^{1/H}$) between perturbation center and the initial upstream divide ($\Psi_M = L_M/x_H$, equivalent to equation (2.23) in 1D; $\Psi_D = L_D/x_H$, which has no 1D analogue).

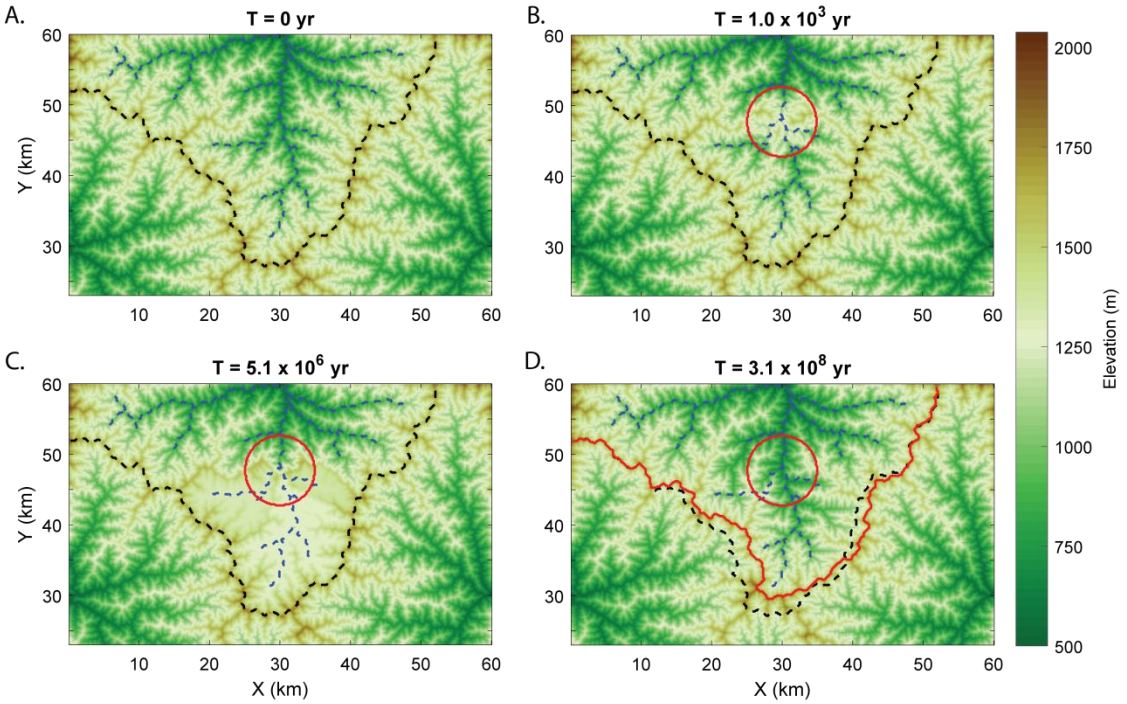

Figure 2.8 – 2D model exhibiting Regime 3 behavior, plotting the upper half of the model domain. Dashed black and blue lines represent initial divide locations and river channel positions, respectively. Red circles represent perturbation boundary within landscape. Solid red line indicates final steady-state divide location. Panel titles indicate model times at (**A**) initial steady-state topography; (**B**) after perturbation uplift has ended; (**C**) transient topography showing upstream plateau uplift; and (**D**) final steady-state topography.

Ψ_M and $\Psi_D$capture the magnitude and extent of divide migration, but do not quantify channel network topology associated with basin area change. Thus, we calculate the basin areal difference, on a pixel-by-pixel basis, between initial and final steady states. This change is measured by the basin Jaccard distance (Jaccard, 1901) defined as

$$d_B = 1 - J(B_I, B_F) = 1 - \frac{|B_I \cap B_F|}{|B_I| + |B_F| - |B_I \cap B_F|}, \tag{2.25}$$

where $J(B_I, B_F)$ is the Boolean Jaccard similarity index between the initial (B_I) and final (B_F) sets of model catchment pixels; $|B_I|$ is the total number of perturbed-basin pixels in the initial topography, $|B_F|$ is the total number in the final topography, and $|B_I \cap B_F|$ is the number of

pixels that exist in both states (Figure 2.9.A, shaded regions). Values of d_B closer to 1 correspond to greater dissimilarity between model domains.

We find that low β and η produce negligible disruption (we impose a threshold of 2 altered pixels to register a signal) between states (Figure 2.9). Ψ_M and Ψ_D increase with increasing β and η, suggesting perturbation locations control the extent of drainage divide response, and overall stability of the initial steady state. Maximum response magnitudes are always less than the distance between the perturbation and divide, but ridges always migrate towards the perturbation (similar to the 1D behavior).

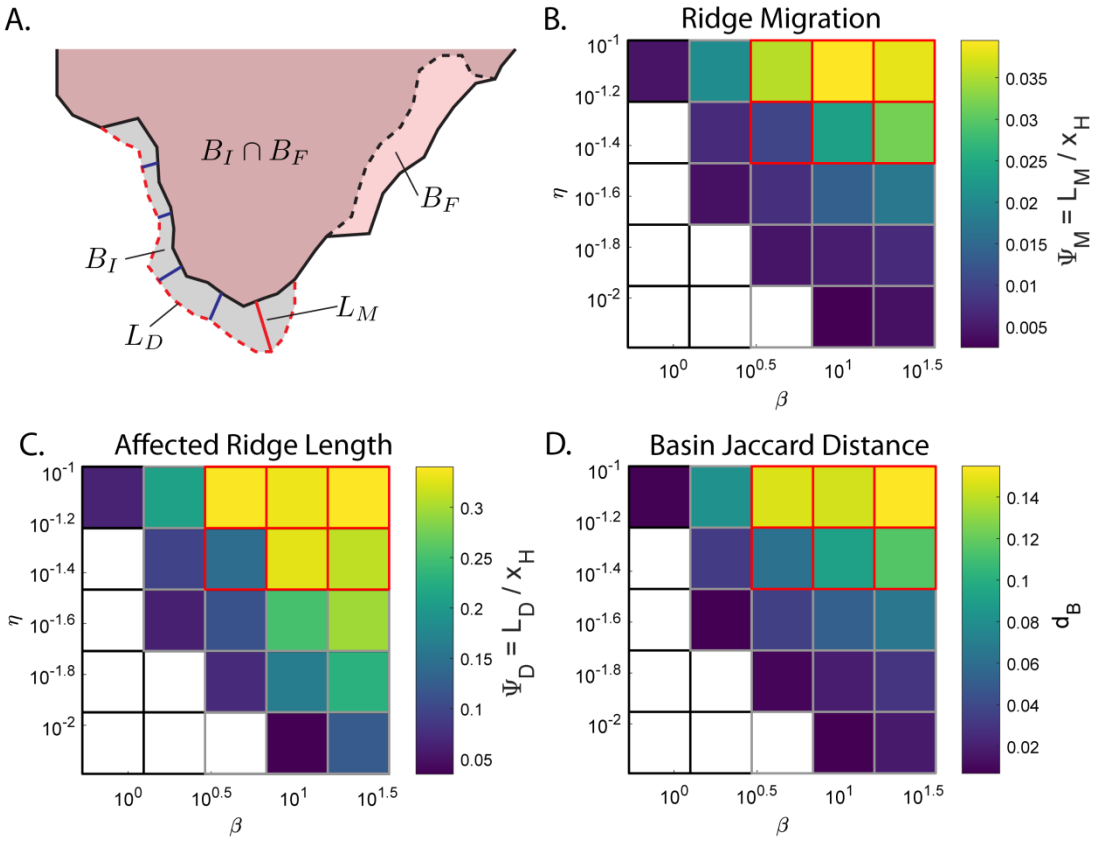

Figure 2.9 – Regime diagrams for a grid search of 25 2D models. Colored panels correspond to specific nondimensional metrics between initial and final steady states, with borders representing model behavior regimes (black is Regime 1, gray is Regime 2, red is Regime 3), as described in the text. White panels exhibit no change between initial and final steady states. **A:** Metric schematic, shaded areas are initial and final perturbed basin, dashed lines are initial basin divide, and solid black line is final basin divide. Blue lines are shortest distance between initial and final ridge points, with solid red line being the longest distance ($\boldsymbol{L_M}$). Dashed red line represents longest segment of initial divide that is separated from the final ($\boldsymbol{L_D}$). **B:** Maximum divide migration ($\boldsymbol{L_M}$, solid red line of A), scaled by Hack's Law distance to divide ($\boldsymbol{x_H}$). **C:** Length of initial divide that experienced migration ($\boldsymbol{L_D}$, red dashed line of A), scaled by Hack's Law distance to divide. **D:** Jaccard distance $\boldsymbol{d_b}$ (equation (2.25)) between initial and final pixels of the perturbed basin (shaded regions of A).

The Jaccard distance d_B shows a similar pattern (Figure 2.9.D), and captures an important difference to 1D model results: in 2D, localized transient uplift perturbations cause significant and distributed disruption even after completion of the perturbation and the landscape has adjusted back to topographic steady state. Maximum d_B for the 25 simulations we show here is 0.16, which represents 16.9% area adjustment of the perturbed basin between initial and final steady states. This value corresponds to a perturbation size (as a fraction of initial basin size) of 32.4%, and an adjusted basin area to perturbation area ratio of 0.52. Across all models, this ratio ranges from 0.002 to 8.2.

Furthermore, we observe model behaviors that are qualitatively-analogous to the 1D model regimes again separate in the nondimensional parameter space (Figure 2.9.B-D, borders). Low β and η values generate Regime 1 behaviors defined by no plateau formation and minimum disruption (black borders). Mid-ranged values follow Regime 2, where the perturbation creates plateaus that are subsequently dissected by the perturbed basin's main channel when the perturbation erodes (gray borders). Finally, high β and η cause Regime 3 behavior where plateaus persist until they are dissected on all sides by the surrounding basins, causing a large degree of divide migration (red borders).

3.2.2 Transient topographic adjustment

Landscape disruption also occurs transiently during and after the uplift perturbation. As with 1D models, we observe a landscape evolution that involves knickpoints and plateau formation. We also observe lateral internal channel reorganization that is not possible in 1D models. To illustrate the effect of single perturbation parameters on topographic adjustment through time, we calculate a topographic derivation d_t between the initial steady state $z(x, y, 0)$ and time-varying elevations $z(x, y, t)$ as

$$d_t = 1 - \frac{|z(x, y, 0) \cap z(x, y, t)|}{|z(x, y, 0)|}, \tag{2.26}$$

limited to grid cell differences less than 5% topographic change from the initial state. Thus, $|z(x,y,0)|$ is the total number of model grid cells and $|z(x,y,0) \cap z(x,y,t)|$ is the total number of grid cells where $|z(x,y,0) - z(x,y,t)|/z(x,y,0) < 0.05$.

Figure 2.10 illustrates the difference in transient landscape response to local perturbation disruption between Regime 2 and 3 behaviors. Regime 2 response is characterized by non-monotonic increases in $d_t$through time (Figure 2.10.A). Rather, d_t initially increases when local minima upstream of the perturbation uplift as a plateau; followed by a decrease in d_t as the perturbation and plateau are eroded by the perturbed-basin channels; and finally small increases in d_t as the landscape adjusts to minor disequilibrium. Conversely, Regime 3 response is characterized by a monotonic increase in d_t as the perturbation creates a plateau that continuously uplifts until it is dissected by the surrounding basins (Figure 2.10.B-C, red lines).

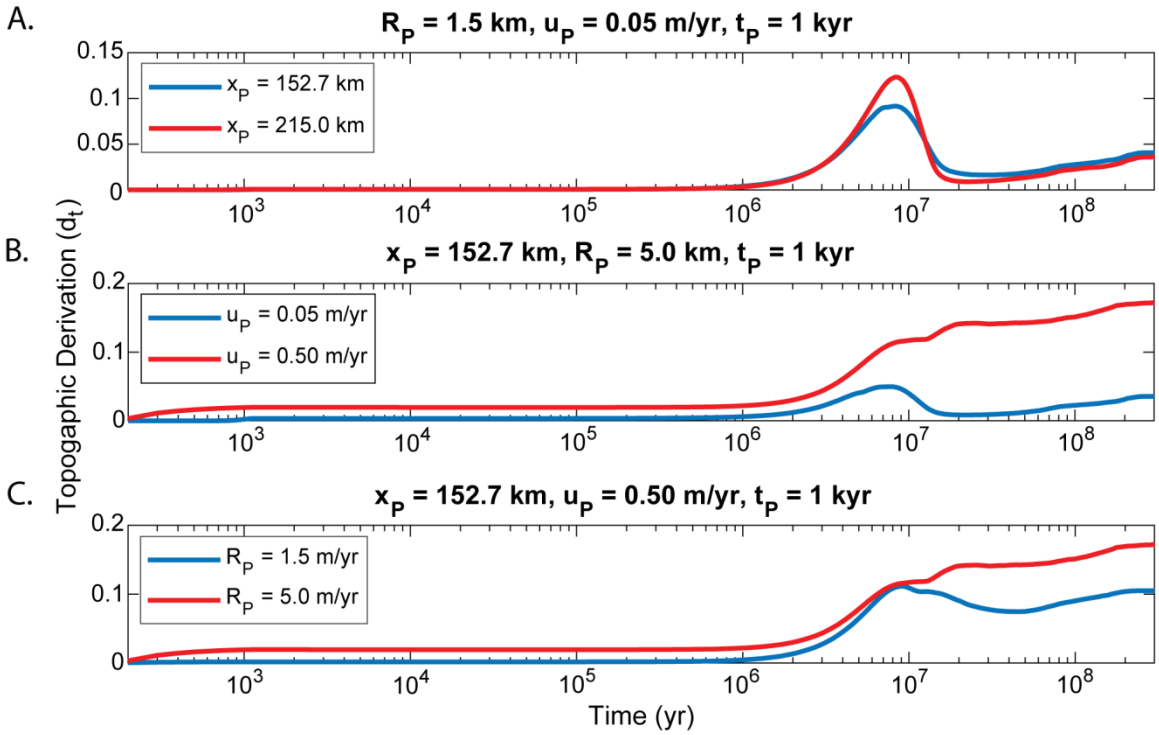

Figure 2.10 – Transient topographic distance $\boldsymbol{d_t}$ through time for 2D models, panels represent differences in a single parameter. **A:** Differences in perturbation location ($\boldsymbol{x_P}$). **B:** Differences in maximum perturbation uplift rate ($\boldsymbol{u_P}$). **C:** Differences in perturbation radius ($\boldsymbol{R_P}$).

Figure 2.10 also demonstrates parameter dependencies that are convolved through the nondimensional η and β. We see that perturbations forming close to the divide have smaller initial influence on topographic change than those from further down the basin, which are able to affect more upstream sub-catchments (Figure 2.10.A); however, long-term adjustments are equivalent. Similarly, low uplift rates are less disruptive compared to higher rates (Figure 2.10.B), consistent with geometric predictions from 1D (Figure 2.4). Finally, the amount of disruption increases with greater radii (Figure 2.10.C), as larger perturbations are able to influence neighboring sub-basins within the landscape. Generally, perturbation size and uplift rate are the most important parameters determining subsequent landscape response.

4.0 Discussion

Landscapes respond to perturbations that occur on a wide range of spatial and temporal scales. We analyze spatially localized, transient uplift perturbations and find they can affect landscapes nonlocally: the scale of landscape response to a particular size and location of disruption extends well beyond the perturbation. This behavior is distinct from landscape adjustment to large-scale climate or tectonics, and may be important for determining transient histories in terrain that regularly experiences local disruptions.

In both 1D and 2D models, transient topographic response to localized perturbations includes plateau formation by channel beheading and divide migration. Previous studies have characterized such topographic measures of transience through the lens of fluvial channel profiles (e.g., Kirby and Whipple, 2001; Royden and Perron, 2013; Willett et al., 2014) or hillslopes (e.g., Dibiase et al., 2012; Hurst et al., 2013). Here, we show the integration of both process classes demonstrates distinct regimes of fluvial versus hillslope control.

Landscape transient response to uplift perturbations is controlled by a competition between kinematic wave propagation that transmits information about uplift and erosion perturbations up fluvial channels, and migration of drainage divides that separate domains of

fluvial incision with lateral erosion velocities of opposite sign. These two wave-like adjustments occur on vastly different timescales, and vary strongly in space according to Hack's Law.

We analyze the competition between these two timescales for a Regime 3 1D model in Figure 2.11 (parameters in caption). We plot the maximum (yellow lines) and spatially-averaged (red lines) channel wavespeeds in the left and right basins along with the numerically-evaluated drainage divide migration speed (blue line). We see that the perturbation experiences leftward ridge migration as soon as it forms. When the initial drainage divide is captured by the perturbation, ridge migration direction switches and the model relaxes back to steady state.

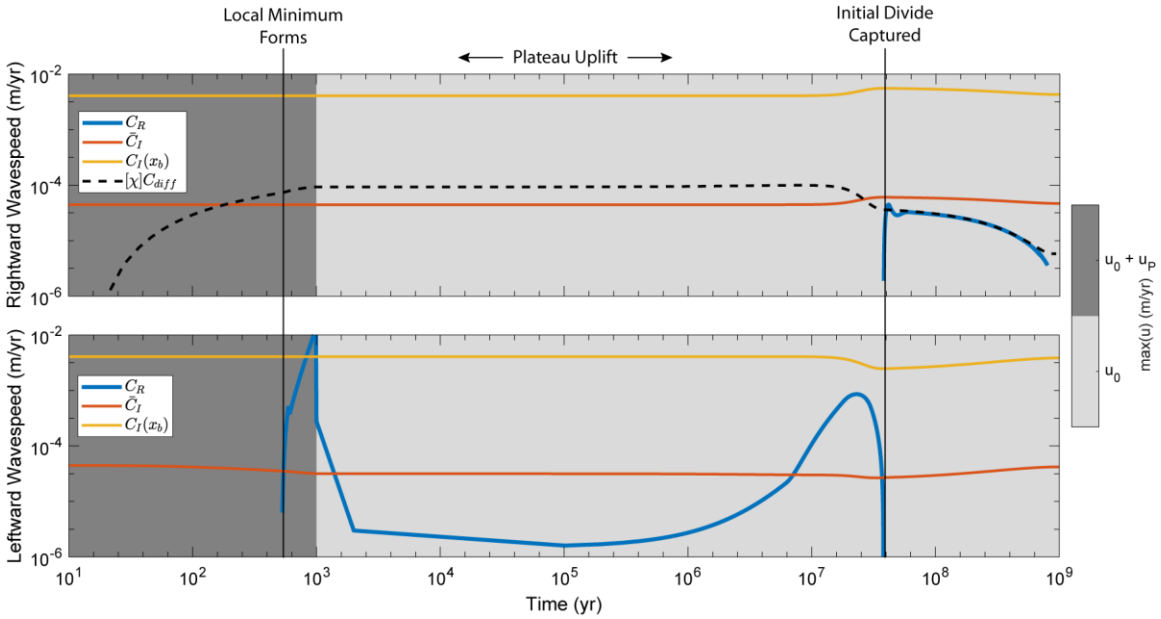

Figure 2.11 – Rightward (top panel) and leftward (bottom panel) 1D model wave speeds through time for Regime 3 model with parameters: $\boldsymbol{u_P = 5.6}$ m/yr, $\boldsymbol{t_P = 1000}$ yr, $\boldsymbol{R_P = 13.3}$ km, $\boldsymbol{x_P = 16.7}$ km. Blue lines represent main divide migration speeds ($\boldsymbol{C_R}$). Dashed line is divide migration speed from equation (2.26). Red and yellow lines are mean ($\boldsymbol{\overline{C_I}}$) and maximum ($\boldsymbol{C_I(x_b)}$) channel wave speeds. Panel shading is by maximum uplift rate in the domain.

Divide migration velocity C_R is determined by the difference in erosion rates on either side of a ridge (Mudd and Furbish, 2005). However, nonlocal and spatially variable geomorphic transport laws in the vicinity of ridges make calculating ridge velocity challenging. A solution to this is the dimensionless transformed version of the downstream distance x suggested by (Royden and Perron, 2013), defined (for constant erodibility K) as

$$\chi = \frac{1}{h_0} \int_{x_b}^{x_c} \left(\frac{A_0}{A(x)} \right)^M dx, \tag{2.27}$$

where h_0 and A_0 are a reference elevation and drainage area, respectively. Willett et al. (2014) propose that the jump in χ evaluated across a drainage divide, $[\chi] = \chi_R - \chi_L$ for χ_R calculated from (27) in the right basin, and χ_L calculated in the left basin, predicts the direction of ridge migration.

We find that, scaling $[\chi]$ by the rate of soil diffusion that controls transient response for $x < x_c$, ridge migration direction and magnitude can be predicted (black dashed line in Figure 2.11). When non-uniform uplift is absent, as in the final transient evolution of 1D models, ridge velocity is

$$C_R = [\chi] C_{diff}, \tag{2.28}$$

where $C_{diff} = D/x_c$ is a hillslope linear diffusion speed with x_c given by equation (2.9). We let $h_0 = 1$ m and determine A_0 empirically to be 0.09 m^2 for our simulations. This method of using the difference between the integrated channel profiles differs from that derived by Braun (2018) based on local channel head slopes.

Equation (2.28) suggests that differences in fluvial erosion across a divide alone is insufficient for predicting divide migration. Although we do not explicitly focus on the mechanics of hillslope processes, hillslope-channel coupling through ridge migration affects global aspects of model landscape response. Figure 2.12 shows time evolution of three Regime 3 1D models, identical to that in Figure 2.11 except for the value of D. We see that, although the early stages of landscape response dominated by transient uplift and plateau formation are nearly identical, later stages of ridge migration vary significantly both in rate of adjustment and transient divide height. As demonstrated by Figure 2.12.C, C_R as calculated by equation (2.28) accurately predicts the rate of ridge migration in each case. This provides an integrated physical interpretation of ridge migration velocity hypothesized by (Whipple et al., 2017b) on the basis of 2D simulations and

single-basin 1D models. Both knickpoint advection and hillslope soil transport play a major role in setting divide stability and migration rates (Figure 2.11, equation (2.28)).

We observe that localized uplift acts as a lens for upstream divides, both vertically amplifying (Figure 2.6.C) and laterally advecting ridges towards the perturbation (Figure 2.8). This behavior is distinct from perturbations that cause all drainage divides to migrate, as in response to a gradient in forcing imposed across the entire landscape (Bonnet, 2009; Willett et al., 2014). Although not analyzed explicitly, divide transience should also manifest in neighboring basin divides not shared with the perturbed basin, as changes in drainage area induce an erosional response in all downstream channels (Willett et al., 2014).

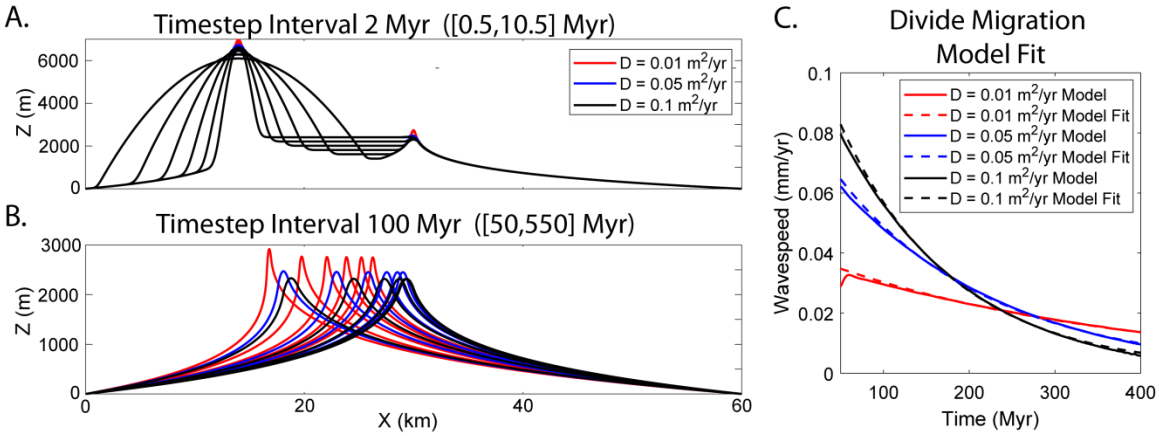

Figure 2.12 – Regime 3 models with same parameters as Figure 2.9, but for different values of soil diffusivity (***D***). (**A**) Model topography during localized uplift and plateau formation. (**B**) Ridge migration after local minima have eroded. (**C**) Main drainage divide rightward migration rates of model (solid lines) and fits from equation (2.26) (dashed lines) over timescales described in panel B. Comparable to upper-panel of Figure 2.9, after initial divide has been captured.

The results of our 1D and 2D models provide a new conceptual approach to inferring erosional histories from current topographic state. Although this study focused on perturbations formed by transient bedrock uplift, our results may also apply to other topographic perturbations. Large landslides can dam channel valleys on 1 – 100,000 yr timescales, creating local minima that stretch 1 – 100's of kilometers upstream (e.g., Mackey et al., 2011), within the range of scales explored here. Although these perturbations are short-lived, a quiescence of erosion upstream of the landslide would induce behavior similar to that observed in Regime 2 – small amounts of upstream divide amplification and migration towards to the perturbation before incision by dam-

breaching. Similarly, slow moving landslides and earthflows can provide locally higher sediment loads that modulate channel incision (Egholm et al., 2013), creating knickpoints similar to our Regime 1 models.

Other environments relevant to this study are continental magmatic landscapes, where localized and episodic uplift via intrusions and eruptions is common. For example, the Colorado Plateau, USA, contains numerous Oligocene laccolith groups that were emplaced on previously lower-relief topography (Gilbert, 1877). Our results suggest that sufficiently large-amplitude localized uplift will reorganize small catchments into radial drainage patterns, but pre-existing fluvial channels with large drainage areas may persist in time. Thus, drainage patterns surrounding these laccolith groups could encode the prior landscape form and rate of magmatic uplift through time on the Colorado Plateau.

The Cascades volcanic arc, USA, provides another example, where subduction-related tectonic uplift and a rain shadow-induced precipitation gradient are present. However, uplift perturbations in the form of volcanic edifices, lava flows, ash deposits (Hildreth, 2007), landslides (Pierson, 2009), and intrusion-related surface deformation (likely prevalent although poorly documented except in special cases, e.g., Wicks et al., 2002) are common. Within this complex environment, signatures of landscape evolution are difficult to diagnose, but our analyses suggest predictions to test.

For example, the dichotomy between high, relatively undissected High Cascades topography is often posited to reflect differences in hydrology that controls the efficiency of fluvial erosion (e.g., Jefferson et al., 2010). However, we have shown beheading of channels by magmatic intrusions can also produce plateau-like provinces. Likewise, although the main Cascades drainage divide is approximately parallel to the subduction zone, along-arc divide variations and downstream channel patterns reflect interplay between local volcanic disruptions, background tectonics, and erosion within the context of this model. Landscape evolution in volcanic terrains is poorly constrained compared to other tectonic environments (Karlstrom et al.,

2018), but we see an opportunity to use topographic form to infer long-term magmatic as well as erosional patterns.

5.0 Conclusion

We conclude by revisiting the problem posed by a spectrum of landscape perturbations at a range of length scales (Figure 2.1). Past studies have analyzed landscape response to large-scale processes such as tectonics, climate, and mantle upwelling. We analyze the effects of meso-scale uplift perturbations to landscape evolution, finding a spatially distributed and long-lasting topographic response.

6.0 Bridge

Chapter II explores the role of localized uplift perturbations on regional-scale landscape evolution. Using both a 1D and 2D landscape evolution numerical model, we analyze the effect of perturbation size, position, timescale, and uplift rate on basin morphology. We find that these effects can range from simple knickpoint propagation within channels to upstream plateau formation, regional divide migration, and even basin-scale drainage reorganization; generating morphologic changes that are often larger than the initial perturbation. Furthermore, nondimensional analysis of the model governing equations show that response is systematic with consideration to two nondimensional terms that convolve perturbation parameters and initial conditions.

The results of this study are applicable to a range of natural processes that perturb landscapes on scales similar to typical drainage basins. Such perturbations are particularly common in active volcanic regions, where magmatic intrusions and extrusions can rapidly build topography on the order of $\sim 1 - 10^3$ m/yr over short ($\sim 1 - 100$ year) timescales (e.g., de Saint-Blanquat et al., 2006; Castro et al., 2016). However, this chapter explored the effects of only one perturbation, whereas volcanic provinces often have multiple generations of magmatic bodies and volcanic extrusions emplaced into the crust and surface environment over millions of years (e.g.,

Nelson and Davidson, 1997; Hildreth, 2007; Karlstrom et al., 2018). In Chapter III, I use elastic models to explore the topographic signatures of one class of magmatic landscape construction, regional-scale intrusive magmatism. In particular, I analyze how intrusion geometry, depth, and spatial distributions contribute to topographic form, constraining the degree to which landscapes can inform long-term crustal magmatic history within volcanic settings.

CHAPTER III

REPEATED STOCHASTIC INTRUSIONS AND THE DEVELOPMENT OF MAGMATIC TOPOGRAPHY

1.0 Introduction

Volcanic provinces cover ~10% of Earth's terrestrial surface (Wilkinson et al., 2009), and record the long-term convolution of processes related to tectonics, climate, and magmatism (e.g., Jellinek et al., 2004; Hildreth, 2007; Sternai et al., 2016). On the surface, volcanic centers (fed by underlying crustal magma reservoirs) generate constructive and deconstructive topography on both local (e.g., edifices) and regional (e.g., flood basalts, ash deposits) scales. Such features are subsequently degraded through various erosional processes (e.g., Hayes et al., 2002; Ferrier et al., 2013; McGuire et al., 2014; Karlstrom et al., 2018), while also impacting landscape evolution over thousands to millions of years (e.g., Jefferson et al., 2010; O'Hara et al., 2019)

Within the crust, magmatic plumbing systems are expansive (Cashman and Giordano, 2014), ranging between 1 to 1000's of km^3 (De Saint Blanquat et al., 2011), and storing anywhere between 2 and 100 times the amount of magma that extrudes on the surface (White et al., 2006; Morriss et al., 2020). A growing consensus is that magmatic systems emplace as small bodies that can accumulate into larger chambers through thermal recharge over timescales shorter than heat dissipation through the crust (e.g., de Saint-Blanquat et al., 2006; Annen et al., 2015). This incremental assembly is consistent with the generation of long-lived, trans-crustal magmatic systems (Cashman et al., 2017; Sparks et al., 2019), with tiered, high-temperature zones containing crystal mush and distributed pockets of magma that form a complicated and time-evolving transport network between the mantle source and surface volcanoes (e.g., Schmidt et al., 2008; Till et al., 2019)

The province-scale distribution of volcanic edifices on the surface records the spatial and compositional characteristics of the underlying magmatic structure, reflecting the long-term

history of both mantle magma sources (e.g., Schmidt et al., 2008; Till et al., 2019) and magma-tectonic stresses (e.g, Maccaferri et al., 2014). Vents in monogenetic fields are often dispersed, following a Poisson spatial distribution (Baloga et al., 2007), unless structurally-controlled by local faulting (Connor and Hill, 1995). Conversely, long-lived magmatic centers have more clustered vent distributions (Karlstrom et al., 2015), suggesting magmatically-induced stress focusing within the upper-crust.

Various studies have analyzed the long-term thermal and compositional evolution of magmatic systems in the lower- to mid-crust through numerical modeling (e.g, Annen and Sparks, 2002). Such models have assumed a variety of intrusion emplacement geometries, such as sets of stacked sills (e.g, Annen et al., 2006) or stochastically-emplaced dikes of random orientation (e.g, Dufek and Bergantz, 2005). However, these models represent only one end-member of the crustal response to long-term magmatism; with elastic displacement from magmatic intrusions being another. Multiple studies have modeled surface deformation associated with assumed single intrusions within both active (e.g, Parks et al., 2015; Castro et al., 2016) and ancient (e.g., Pollard and Johnson, 1973) settings. However, the long-term elastic response to multiple generations of intrusions – and in particular the development of surface topography (landscape construction) associated with repeated, stochastic intrusions within the upper crust – remains unexplored.

A limiting constraint on the applicability of elastic models to study the long-term response to magmatism is whether the crust continues to behave elastically with the emplacement of multiple intrusions. However, a simple back-of-the-envelope approximation for the rheologic response of the crust to an emplaced intrusion suggests such analyses are plausible. The Deborah Number measures the ratio of timescale between crustal stress relaxation and magma injection ($De = T_{relax} \,/\, T_{inject}$), where the relaxation timescale can be approximated as the crust's viscosity divided by its Young's modulus ($T_{relax} = \gamma \,/\, E$) and the injection timescale is an

intrusion's volume divided by the incoming volumetric flux ($T_{inject} = V / Q$). The crust behaves elastically when $De > 1$, and viscously when $De < 1$. If we assume a Young's modulus of $1x10^{10}$ Pa (Turcotte and Schubert, 2010), a crustal viscosity of $1x10^{19}$ Pa s (lower than average upper crust, as might occur within a somewhat heated system; Karlstrom et al., 2010), as well as a relatively small-volume ($0.01\ x10^{9}$ km^3; corresponding to a ~1.3 km-radius sphere) intrusion, and a typical flux of $1x10^{-3}$ km/yr (De Saint Blanquat et al., 2011), De equates to ~3.2, which is within the elastic regime. In fact, this calculation suggests that as long as the volume of an intrusion is sufficiently small and is emplaced sufficiently rapidly, the crust will generally behave elastically regardless of viscosity (Karlstrom et al., 2017).

With this framework in place, various questions can be asked about the elastic response to trans-crustal magmatism: What is the topographic consequence of emplacing multiple small-scale magmatic intrusions within the crust? What can the surface tell us about the spatial and geometric distributions of intrusions? Do these intrusions contribute only to topographic relief, crustal thickening, or a combination of both?

Here, we explore these questions by analyzing the topographic signature associated with long-term intrusive activity within the crust. By applying single-intrusion models stochastically at regional scales, we determine the extent to which magmatic bodies of varying sizes, depths, and spatial distributions leave a surficial fingerprint. We then model these results with simplified approaches (single intrusions, thin plate flexure) to gain insight on how surface characteristics relate to the distribution of intrusions at depth. This allows us to demonstrate when it is possible to determine ensemble intrusion parameters from topography.

2.0 Methods

To understand the surficial signature of province-scale crustal magmatism, we simulate multiple single-body intrusions stochastically-emplaced within the upper crust. We isolate the effects of various intrusion sizes, depths, and spatial distributions on the transient evolution of

topography and crustal thickening by focusing only on surficial displacement and ignoring erosion. Below, we describe the numerical model setup, suite of model parameters explored, and model analyses.

2.1 Stochastic intrusion model

Processes associated with crustal magmatic emplacement are multifaceted (e.g., Tibaldi, 2015). The thermomechanical response of the crust to magmatic intrusions varies as a function of depth, temperature field, and crustal heterogeneity (e.g., Dufek and Bergantz, 2005; Annen et al., 2006; Rivalta et al., 2015), and is further influenced by the geochemical evolution of magma associated with differentiation, rejuvenation, and assimilation of wall rock (e.g., Annen et al., 2006).

We ignore many of these complexities and focus on a mechanical model that considers only the elastic crustal response to magmatism. Our calculation of relaxation timescale in the introduction suggests such an approach is reasonable, as small-volume intrusions will dominantly be emplaced within an elastic regime of the upper crust (Karlstrom et al., 2017). We assume the crust has homogeneous properties, despite the emplacement of multiple bodies within our model, and derive a model for the transient evolution of regional-scale magmatism by randomly sampling intrusion parameters from given distributions and emplacing them spatially within the crust, tracking both the surface displacements and cumulative intrusion thicknesses. Here, we outline the main components of the model.

2.1.1 Single intrusion surface displacement

Various elastic models for single intrusions exist, with model limitations set by the intrusion radius (R) and depth (d). For example, geodetic studies often model deep ($R \ll d$) intrusions using an inflating point source within the crust (i.e., the 'Mogi' model; Mogi, 1958; McTigue, 1987); whereas models based on laccoliths and other shallow ($R \gg d$) intrusions typically consider crustal flexure with a thin-plate-type model (e.g., Pollard and Johnson, 1973;

Galland and Scheibert, 2013). We use a model that effectively interpolates between these end-member regimes in the $R - d$ parameter space; the flexural response (w) associated with pressurization of a penny-shaped crack (Fialko et al., 2001) is

$$w(r) = \frac{2(1-\nu)\Delta P R}{\mu} \int_0^\infty \left[\left(1 + \xi \frac{d'}{R}\right) \mathbf{\Phi}(\xi) + \xi \frac{d'}{R}\, \mathbf{\Psi}(\xi) \right] e^{-\frac{\xi d'}{R}} J_0(\xi r)\, d\xi, \qquad (3.1)$$

where $r = \sqrt{(x - x_0)^2 + (y - y_0)^2}$ are radial coordinates from the intrusion center (x_0, y_0), x and y are Cartesian coordinates, ν and μ are the Poisson's ratio and shear modulus of the crust, and ΔP is the magma overpressure. For simplicity, we assume constant ν, μ, and ΔP values of 0.35, 2 x 10^4 MPa, and 40 MPa, respectively. J_0 is the zeroth-order Bessel function over coordinate ξ, $\mathbf{\Phi}$ and $\mathbf{\Psi}$ are image functions that are iteratively solved to satisfy free surface and crack plane boundary conditions (Fialko et al., 2001).

The formation of the penny-shaped crack inflation model assumes a flat free-air boundary condition in order calculate displacement. However, such an assumption is not valid within the framework of our model, where previous intrusions generate dispersed topography. These topographic loads alter the stress state of the crust and can impact the elastic response to inflation (e.g., Maccaferri et al., 2011). One solution to this is to account for the such stress states within the governing equations (e.g, McTigue and Stein, 1984). However, this further complicates the model and is computationally expensive. A second, simpler approach is to adjust the depth of the intrusion to account for overlying relief. Williams and Wadge (1998) found, for the inflating point-source model, that this adjustment generates approximately the same solution as altering the governing equations. Here, we follow this approach and calculate d' as the depth of the intrusion corrected to account for overlying topography (Z):

$$d' = d + Z(r = 0) - \min(Z). \qquad (3.2)$$

To analyze the connections between intrusions and surface displacements, we also model intrusion thicknesses. For simplicity in our analyses and numerical efficiency over thousands of intrusions, we parameterize the complicated algebraic expression for intrusion thickness from equation (3.1) as the semi-minor axis of an axisymmetric ellipsoidal body of radius R. The volume of the ellisoid is assumed to be the volume change (ΔV) associated with the pressurized crack (Fialko et al., 2001):

$$\Delta V = \frac{4\pi R^3(1-\nu)\Delta P}{\mu} \int_0^\infty \mathbf{\Phi}(\xi) J_0(\xi) d\xi. \tag{3.3}$$

Figure 3.1.A-B shows maximum surface displacements and maximum thicknesses of single intrusions within our explored $R - d$ parameter space. Figure 3.1.C shows the difference in maximum surface displacements (Δw) between the pressurized penny-shaped crack, inflating point source, and thin-plate flexure models. Overall differences between these models are small (< 1 m), except for the largest intrusive bodies within the shallow regime, where the intrusion lateral dimension is much larger than its depth and the pressured-crack model becomes inappropriate.

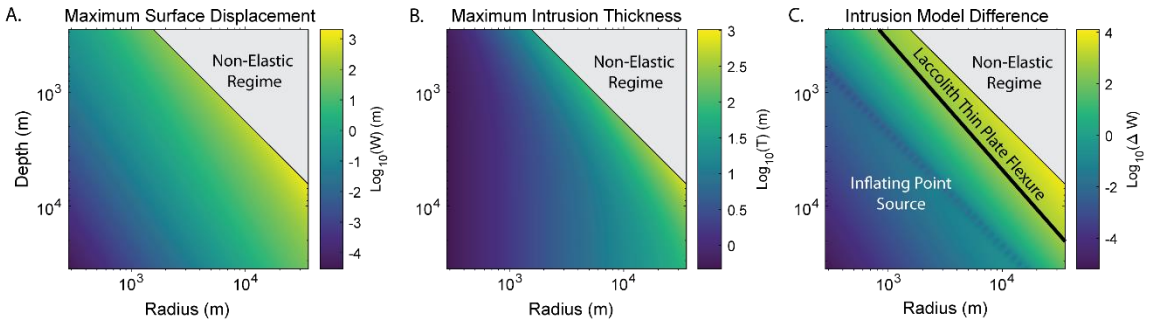

Figure 3.1 – Stochastic model $\boldsymbol{R - d}$ parameter space using the pressurized penny-shaped crack displacement model (Fialko et al., 2001). **A**: Maximum surface displacement. **B**: Maximum intrusion thickness. **C**: Displacement difference between pressurized penny-shaped crack and typical inflating point source (McTigue, 1987) and thin-plate flexure (Galland and Scheibert, 2013) models.

2.2 Model Simulations

We analyze the effects of intrusion parameter distributions using two sets of models. For all models, we intrude magmatic bodies into a periodic spatial grid that has a length of 63.75 km

in both x and y directions, and a grid resolution of 250 m. We sample from an intrusion $R - d$ parameter space ranging ~316 – 31,600 m, which falls within the size distributions of mapped intrusions (Cruden et al., 2017). For consistency across models, we intrude a total magmatic volume of 2000 km^3, within the estimated ranges of exposed plutonic provinces (De Saint Blanquat et al., 2011). Given our spatial grid size, this volume should generate ~ 500 m of mean elevation in all models. For both model sets, we assume a normal bivariate distribution of R and d with standard deviations of 0.01 m in log-log space and no covariance between the two parameters. We then analyze different intrusion distributions by varying the mean R and d values in log-log space (Figure 3.2).

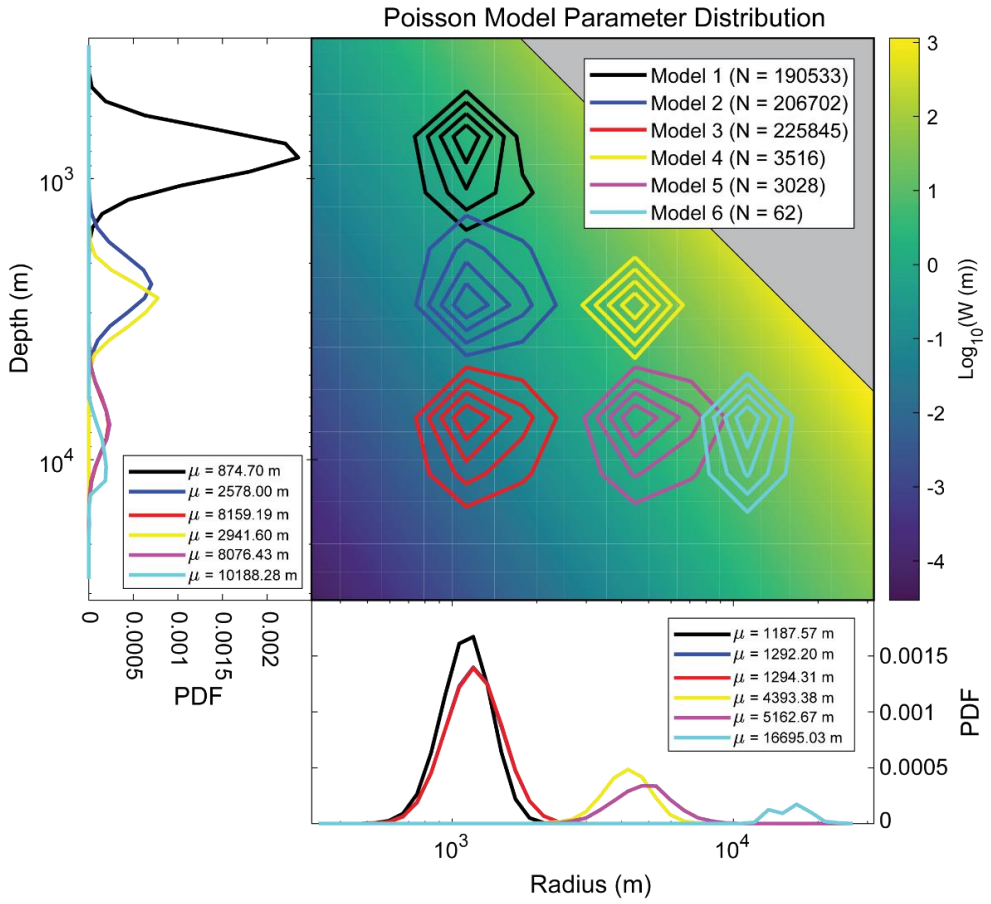

Figure 3.2 – Sampled $\boldsymbol{R - d}$ distributions for the Poisson spatial distribution model set. Within the 2D space, colored lines represent 20% contours of sampled values for each model; inset gives the total number of samples (N). Bottom and left panels show the probability density functions (PDFs) of sampled radius (bottom) and depth (left) values for each model; insets give the mean sampled value ($\boldsymbol{\mu}$). Gaussian spatial distribution model set follows same $\boldsymbol{R - d}$ distributions.

We explore the effects of intrusion spatial distributions on topographic form by examining two end-member distributions. In the first set of models, we assume intrusions have nearest-neighbor distances that follow a Poisson distribution, similar to monogenetic vent fields, and determine intrusion locations by randomly sampling a uniform distribution in both the x and y directions (Baloga et al., 2007). Thus, we model a system of nearly equal-sized intrusions at nearly equal depths that are randomly distributed horizontally. Figure 3.3 shows the final model topography and crustal cross-section of emplaced intrusions for six simulations using a Poisson intrusion spatial distribution.

Although monogenetic vent fields have been shown to follow a Poisson's distribution (e.g., Connor and Hill, 1995) , evolved magmatic systems (e.g., Mt. Mazama; Karlstrom et al., 2015) as well as shallow intrusions (e.g., The Henry Mountains; Gilbert, 1877) often generate more clustered volcanic terrain. The second set of models thus explores this clustering within the crust. We use the same R and d parameter distributions as the first model set (Figure 3.2). However, rather than a Poisson's distributions, we assume intrusions emplace as bivariate normal distributions in both the x and y directions with 10 km standard deviations, no covariance between the two directions, and mean locations that are centered on the model grid. This set of models thus simulates clustered intrusions of nearly-equal radius and depth within the crust. Figure 3.4 shows the final model topography and crustal cross section for six simulations that follow this intrusion spatial distribution.

2.3 Model Analysis

We analyze the connection between surface topography, crustal thickening (without relief generation), and the underlying magmatic intrusion distribution using a variety of techniques. First, we analyze the amount of relief and crustal thickening generated by radius and depth distributions for both the Poisson and Gaussian spatial distribution model sets. Afterwards, we explore the ability of elastic plate flexure to determine intrusion model parameters for the Poisson

spatial distribution models. Finally, we analyze how well single-intrusion models can match stochastic model parameters for the Gaussian spatial distribution models.

2.3.1 Elevation

We analyze the effect of intrusion geometric and spatial distributions on topography using two metrics. First, we assess the overall elevation increase of each model by calculating maximum and mean elevations. Afterwards, we compare the volume of topographic relief to the volume of crustal thickening within each model. We define the volume of relief (V_r) as the volume of material within the topographic range, integrated over the model domain ($X_d = Y_d =$ 31,600 m).

$$V_r = \int_0^{X_d} \int_0^{Y_d} (z - \min(z))\, dy\, dx, \tag{3.4}$$

and the volume of crustal thickening (V_T) as the volume of material between 0 m and the minimum height

$$V_T = \int_0^{X_d} \int_0^{Y_d} z\, dx\, dy - V_r. \tag{3.5}$$

Dividing equation (3.4) by equation (3.5) as

$$\zeta = \frac{V_r}{V_T}, \tag{3.6}$$

thus provides a useful metric for determining whether intrusion distributions contribute more to local ($\zeta > 1$, generating relief) or regional ($\zeta < 1$, generating thickening without relief) topography.

2.3.2 Interpretation of Poisson-distributed intrusions via elastic plate flexure

The relationship between buried loads at depth (such as intrusions) and topography has traditionally been studies in the framework of a thin elastic plate, where deformation (w) is assumed to be only vertical (e.g., McNutt, 1983). The relative simplicity of this framework is

appealing; we explore the extent to which our Poisson-distributed intrusion models can be approximated in terms of the deformation of an elastic plate with some thickness (T_e) in response to a load at the base of the plate as (Wessel, 1996)

$$D\nabla^4 w(x,y) = q_p(x,y) - B_x \frac{\partial^2 w(x,y)}{\partial x^2} - 2B_{xy} \frac{\partial^2 w(x,y)}{\partial x \partial y} - B_y \frac{\partial^2 (w,y)}{\partial^2 y}, \tag{3.7}$$

where B_x, B_y, and B_{xy} are in-plane forces in the x and y direction, and D is the flexural rigidity, defined as

$$D = \frac{ET_e^3}{12(1-\nu^2)}, \tag{3.8}$$

with Young's modulus E and Poisson's ratio ν.

Assuming displacement is of a magmatic origin, and accounting for other possible loads (q), the load at the base of the plate is

$$q_p(x,y) = q(x,y) - w(x,y)g(\rho_m - \rho_a). \tag{3.9}$$

where ρ_a and ρ_m are the densities of air and magma, respectively, and g is acceleration due to gravity.

Assuming the density of air is negligible ($\rho_a = 0$) and no lateral forces exist within the plate ($B_x = B_y = B_{xy} = 0$), substituting equation (3.9) into equation (3.7) gives

$$D\nabla w(x,y) + w(x,y)g\rho_m = q(x,y). \tag{3.10}$$

The 2D Fourier and inverse Fourier transform pair of a signal (f) is

$$\bar{f}(k_x, k_y) = \int_{-\infty}^{\infty} \int_{-\infty}^{\infty} f(x,y) e^{-2\pi i(xk_x + yk_y)} dx dy, \tag{3.11}$$

$$f(x,y) = \int_{-\infty}^{\infty} \int_{-\infty}^{\infty} \bar{f}(k_x, k_y) e^{2\pi i(xk_x + yk_y)} dk_x dk_y, \tag{3.12}$$

with wave numbers k_x and k_y in the x and y direction, respectively. Applying equation (3.11) to the elastic plate flexure equation transforms equation (3.10) into an algebraic equation as

$$2\pi \boldsymbol{k}^4 D\bar{w}(k_x, k_y) + g\rho_m \bar{w}(k_x, k_y) = \bar{q}(k_x, k_y), \tag{3.13}$$

where $\boldsymbol{k}$ is the radial wave number $\left(\boldsymbol{k} = \sqrt{k_x^2 + k_y^2}\right)$. Rearranging equation (3.13) thus gives

$$\bar{w}(k_x, k_y) = \phi \bar{q}(k_x, k_y), \tag{3.14}$$

where

$$\phi = \frac{1}{2\pi \boldsymbol{k}^4 D + g\rho_m}, \tag{3.15}$$

is the isostatic response function (IRF; Walcott, 1970). Equation (3.15) thus predicts the isostatic limitation of our models. Short-wavelength features, or an exceptionally rigid plate, cause ϕ to be 0, and thus no displacement occurs at the surface; whereas long-wavelength features, or a weak plate, cause the load to be compensated as $1 \,/\, \rho_m g$ (i.e. Airy compensation). The wavelength (λ_C) that corresponds to this compensation is defined as (Turcotte and Schubert, 2010)

$$\lambda_C = 2\pi \left(\frac{D}{\rho_m g}\right)^{\frac{1}{4}}. \tag{3.16}$$

To apply equation (3.15) to our models and determine an effective elastic thickness, we assume a single effective depth for our intrusion distribution and calculate the transfer function between intrusion thickness and relief (i.e., admittance; Krishna, 1996). We then find the best-fitting elastic thickness for each model by performing a grid search over the range $\sim 32 - 100{,}000$ m. The lower limit of our parameter search falls within the range of depths explored previously for shallow rhyolitic intrusions (Castro et al., 2016). For each thickness, we calculate ϕ using equation (3.15), then determine the misfit (δ) between ϕ and the admittance as

$$\delta = \sqrt{\sum_{i=1}^{K_x}\sum_{j=1}^{K_y}\left(\frac{\bar{z}(k_{x_i},k_{y_j})}{\bar{\tau}(k_x,k_y)} - \phi(\boldsymbol{k})\Gamma\right)^2}, \tag{3.17}$$

where $\bar{w}$ and $\bar{\tau}$ are the spectral components of relief and intrusion thickness, respectively, i and j are counters over wavenumbers k_{x_i} and k_{y_j}, respectively, with maximum numbers of K_x and K_y, and Γ is a conversion factor between pressure and thickness, which parameterizes the loading of a thin plate associated with a Poisson-distributed sequence of intrusions. For simplicity, we assume Γ is a constant value of $\rho_m g$, with $\rho_m = 2800$ kg/m^3. In reality, Γ likely scales with intrusion depth and radius distributions.

2.3.3 Interpretation of Gaussian-distributed intrusions via a single intrusion

While the Poisson spatial distribution models represent spatially-distributed crustal magmatism, the Gaussian spatial distribution models present more clustered intrusive bodies. Rather than apply plate flexure, we take an approach that is common in studies of landforms associated with shallow intrusions (e.g., Pollard and Johnson, 1973; Goulty and Schofield, 2008; Galland and Scheibert, 2013). Assuming model topography was generated by a single intrusion, we find the best-fit intrusion parameters that match the observed pattern of deformation by performing a grid search of the same $R - d$ intrusive ranges as our stochastic models (~316 – 31,600 m). We compare our models to the single-intrusion fit by calculating the Euclidean distance (δ_z) between the stochastic (Z) and single-intrusion (Z_s) model topographies

$$\delta_z = \sqrt{\sum_{m=1}^{N_x}\sum_{n=1}^{N_y}(Z(x_m,y_n) - Z_s(x_m,y_n))^2}. \tag{3.18}$$

with counters m and n over elements in the x and y directions, having max values of N_x and N_y, respectively. Furthermore, we assume effective magma overpressure is unknown, and thus find the best-fitting $R - d$ parameters for overpressure values ranging $10 - 200$ MPa. For all grid

searches, we use the inflating penny-shaped crack model (Fialko et al., 2001) to determine single-intrusion displacements.

3.0 Results

The Poisson and Gaussian spatial distributions generate vastly different topographies (Figures 3.3 and 3.4). While the Poisson distribution models generate spatially-scattered ridges and troughs of varying scales, the Gaussian distribution models create a single, near-axisymmetric landform. This variability in topographic form also determines the overall height of the model surfaces, with Gaussian distribution models having approximately three times more height than Poisson distribution model (Figure 3.5.A-B, solid lines). However, this increase in height does not necessarily equate to crustal thickening, as we will show. Despite these differences in landform height and distribution, mean elevations of ~500 m are consistent across all models (Figure 3.5.A-B, dashed line), as expected from the volumetric input of magma into the crust. Below, we discuss the results of the analyses described in the Methods section.

3.1 Topographic Analysis

Although large differences exist between the landforms generated by the Poisson and Gaussian spatial distributions, variations within each model set highlights the effect of intrusion radius and depth distributions on topography. Within the Poisson spatial distribution model set, the model intrusion mean radius-to-depth ratio (R/d) exerts a clear control on both relief (Figure 3.3) and overall height (Figure 3.5.A, solid lines) of the surface. This dependence on R/d does not exist for the Gaussian spatial distribution models (Figure 3.4). Rather, elevations appear to be dominantly controlled by only the mean model intrusion depth (Figure 3.5.B, solid lines).

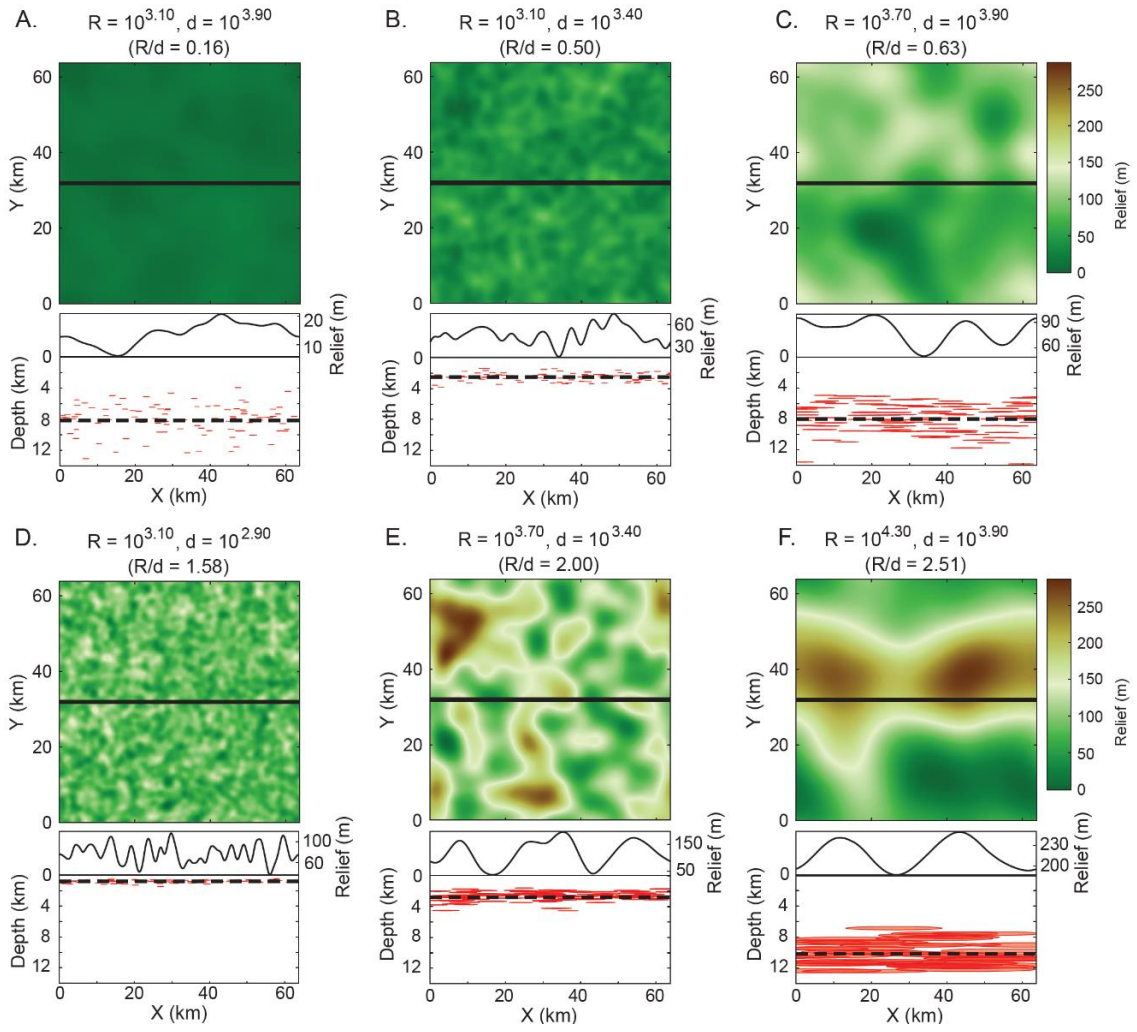

Figure 3.3 – Poisson spatial distribution model topography, ordered by $\boldsymbol{R / d}$. Top panels show model relief, set to the same scale. Bottom panels show cross-sections of both topography and crust through the black lines of top panels. Red ellipses signify locations of intrusions within the cross-section, with thicknesses vertically-exaggerated by 10%. Black-dashed lines show mean intrusion depth.

These trends between elevation and model intrusion parameters further extend to the amount of relief versus crustal thickening generated by intrusions (ζ; equation 3.6). ζ values are all less than 1 for the Poisson spatial distribution models (Figure 3.5.C), suggesting these intrusions contribute most to crustal thickening. Furthermore R / d values influence the distribution of volume, with largest R / d values creating more localized topography. Conversely, the Gaussian spatial distribution models have ζ values much greater than 1 (Figure 3.5.D), signifying magmatism contributes dominantly to relief, with almost no crustal thickening. Although ζ decreases with increasing mean model intrusion depth in the Gaussian spatial

distribution models, we cannot distinguish crustal thickening from flexure-related topography within the model spatial domain.

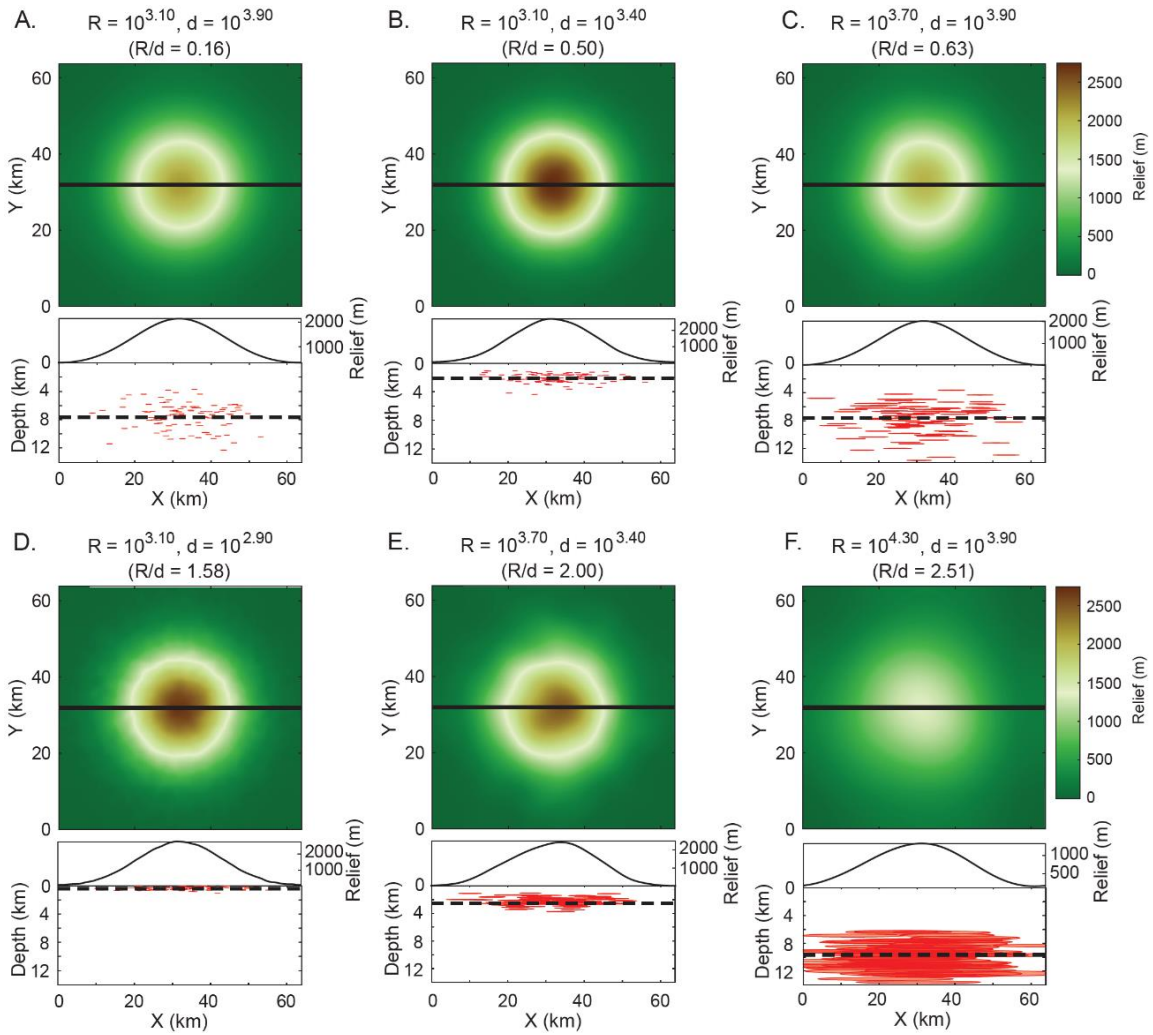

Figure 3.4 – Gaussian spatial distribution model topography, ordered by ***R / d***. Top panels show model relief, set to the same scale. Bottom panels show cross-sections of both topography and crust through the black lines of top panels. Red ellipses signify locations of intrusions within the cross-section, with thicknesses vertically-exaggerated by 10%. Black-dashed lines show mean intrusion depth.

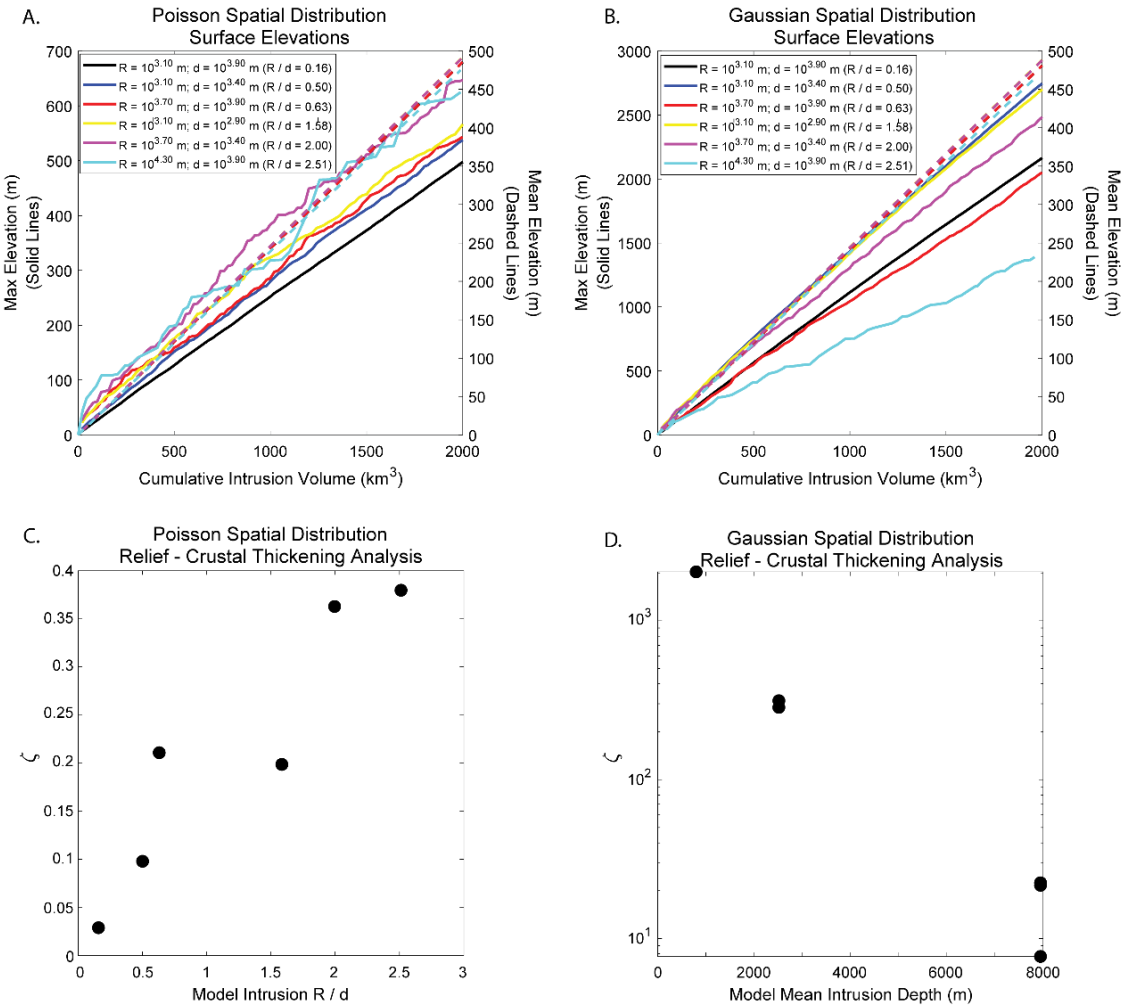

Figure 3.5 – Model topographic analysis. **A-B**: Max (solid lines) and mean (dashed lines) model elevations as a function of cumulative intrusive volume for (A) Poisson and (B) Gaussian spatial intrusion distribution models. Colors correspond to model parameters presented in legend. **C-D**: Ratios of volumes associated with topographic relief and crustal thicknesses (ζ; equation 3.6), ordered by mean model intrusion parameters for (C) Poisson and (D) Gaussian spatial intrusion distributions.

3.2 Plate Flexure Analysis

Overall, we find that the flexural plate model provides an adequate approximation for the displacements associated with regionally-dispersed crustal magmatism. Figure 3.6.A shows the grid search δ values (equation 3.17) over the analyzed elastic plate thickness parameter space, ordered by mean stochastic model intrusion depth on the y-axis. In all cases, the best-fitting elastic plate is thinner than the stochastic model intrusion depths. Figure 3.6.B suggests stochastic

model mean intrusion depths and best-fitting plate thicknesses are linearly-related, having a slope of ~0.28 and R^2 value of 0.97.

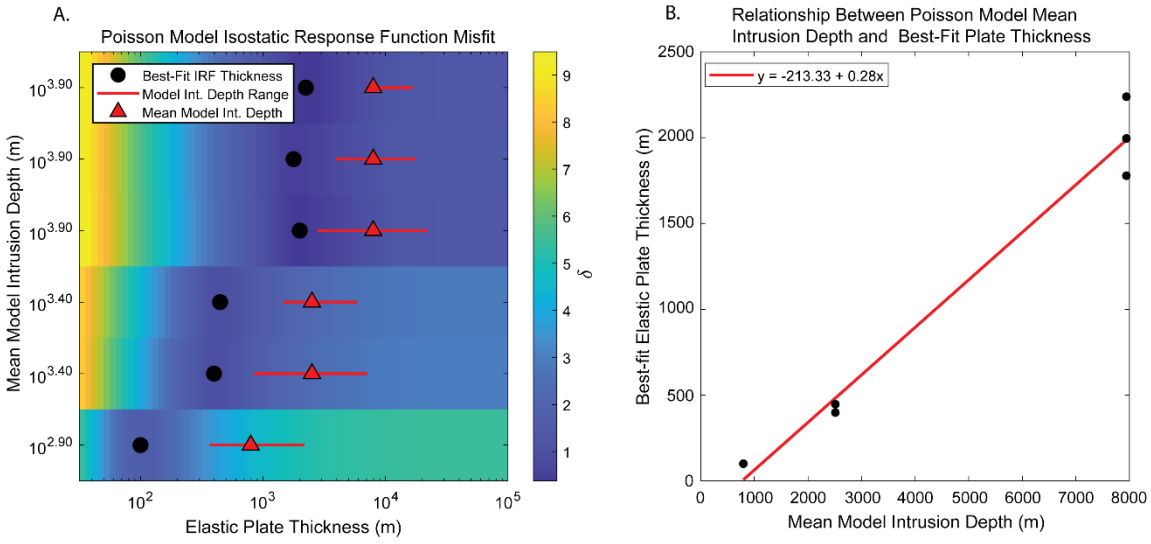

Figure 3.6 – Elastic plate flexure model fits to Poisson spatial intrusion distribution models. **A**: Misfit ($\boldsymbol{\delta}$; equation 3.17) between scaled isostatic response functions ($\boldsymbol{\phi}$; equation 3.15) and surface-thickness transfer functions. X-axis is tested elastic plate thickness, Y-axis is individual Poisson distribution models, ordered by mean model intrusion depth. Black dots are lowest misfit values for each model. Red lines show range of sampled model intrusion depths, with red triangles corresponding to the mean value. **B**: Best-fitting elastic plate thicknesses as a function the corresponding mean model intrusion depth. Red line shows linear regression of values, with equation provided in legend. R^2 value of linear fit is 0.97.

Figure 3.6 suggests model mean intrusion depth is the dominant parameter that influences elastic plate thickness. However, a variety of factors can influence this consistent offset between mean intrusion depth and plate thickness. These include 1) our assumption that intrusions dispersed within the crust can be approximated by a single effective depth; 2) spatial overlapping of intrusions, which can interfere with the spectral energy transfer between thicknesses at depth and surface displacements; and 3) the variability in randomly-selected intrusion parameters (i.e. depth, radius, volume).

Figure 3.7 provides context for how these factors can influence our results by comparing the scaled best-fitting response function ($\phi\Gamma$; equation 3.17) to the $Z - \tau$ admittance for each model, ordered by mean model intrusion depth. In all models, short-wavelength (~10^2 m) features provide good fits between admittance and the isostatic response function. Deviation between

these values occurs at moderate wavelengths (~10^3 m). Across all models, the magnitude of this deviation appears to be depth dependent. Finally, admittance and isostatic response function values begin to realign at approximately the flexural wavelength of the best-fitting elastic plate (Figure 3.7, red-dashed lines).

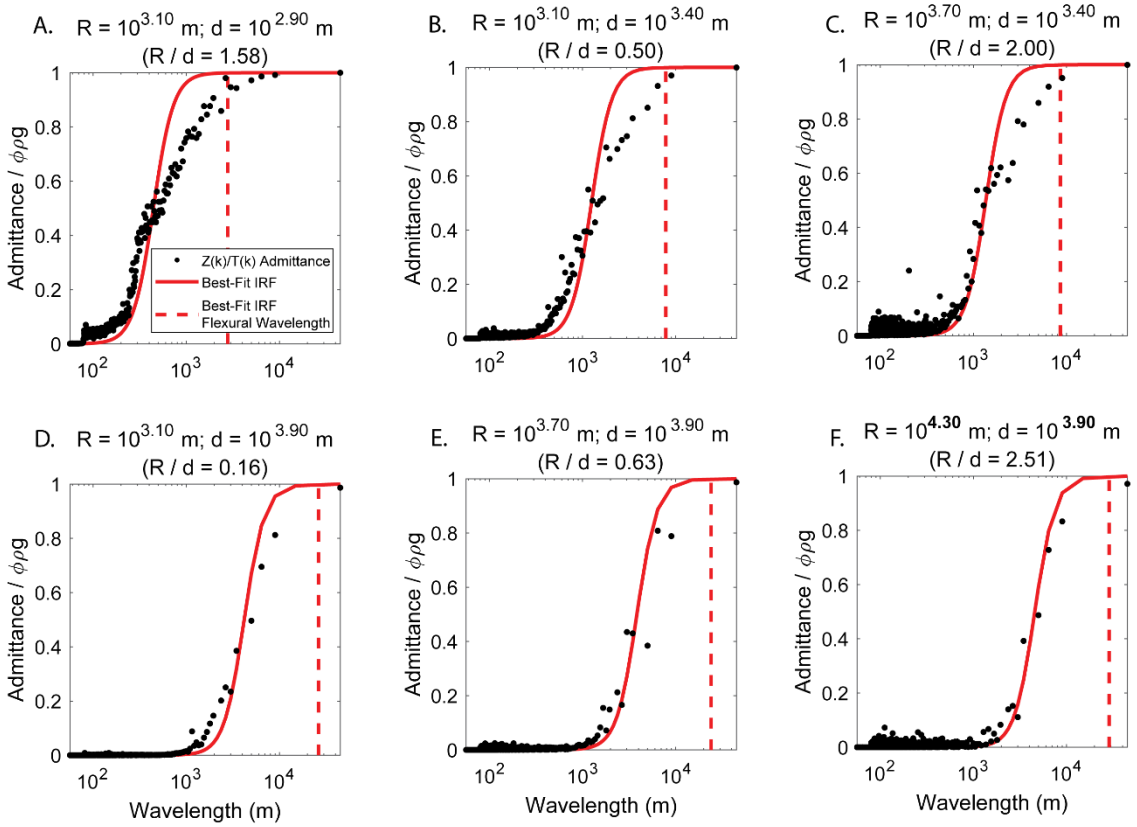

Figure 3.7 – Surface-thickness transfer function (black dots) and best-fitting isostatic response function (red lines) as a function of wavelength for each Poisson spatial intrusion distribution model, ordered by mean model intrusion depth. Red-dashed lines correspond to the flexural wavelength of the best-fitting elastic plate thickness ($\boldsymbol{\lambda_c}$; equation 3.16).

3.3 Single-Intrusion Analysis

Best-fitting single intrusions that match the topography of our Gaussian spatial distribution models significantly differ from the model intrusion input parameters. Figure 3.8 shows the best-fitting single intrusion parameters for the 10-200 MPa overpressure values as a set of box-and-whisker plots for each model, ordered by stochastic model intrusion $R\ /\ d$ ratios. Despite the depth-dependency on model elevations shown in Figure 3.5, we observe no consistent trend between stochastic model mean intrusion depths and best-fitting single intrusion depths

(Figure 3.8.B). This lack of dependence extends to both the intrusion radii parameters (Figure 3.8.A), as well as the $R\ /\ d$ values (Figure 3.8.C). However, we find that the minimum best-fitting single-intrusion radii are well-constrained by the average distance between intrusion locations and the center of the grid (Figure 3.8.A, red-dashed line). This suggests intrusion spatial distributions provide a limiting control on the ability to model densely-packed magmatic bodies as a single intrusion.

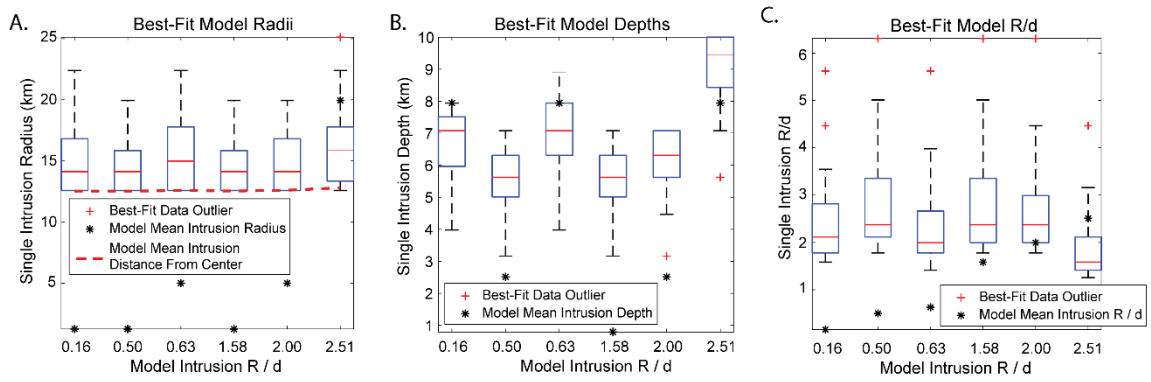

Figure 3.8 – Box-and-whisker plots of best-fitting single-intrusion model parameters to the Gaussian spatial intrusion distribution models for the intrusion overpressure 10-200 MPa values. X-axes are stochastic model mean ***R / d*** values, Y-axes are best-fitting single-intrusion parameter values. Black stars correspond to mean stochastic model parameter values. **A**: Intrusion radii. **B**: Intrusion depths. **C**: Intrusion ***R / d*** values. Red-dashed line in (A) corresponds to the stochastic model mean intrusion distances from the center of grid.

4.0 Discussion

Our results suggest topography encodes the long-term history of crustal magmatic systems, from which approximate system geometry and depth can be inferred. In particular, we find that dispersed magmatic bodies can be well-approximated by plate flexure models. This provides new insight into isostatic studies for interpreting the size, depth, and volume of magmatism within volcanic settings (e.g., McNutt, 1983; Blakely et al., 1997; Perkins et al., 2016b).

As intrusive bodies become more clustered, such as those at long-lived magmatic centers (e.g., Hildreth, 2007), horizontal overlap among intrusions within the crustal column presents a loss of information that limits interpretations from topography. Although intrusion depths and

sizes become uninterpretable from topography, we find that single-intrusion models can still constrain the approximate spatial extent of intrusions. This also gives credence to elasticity-based studies that model plutons as single intrusions (e.g., Pollard and Johnson, 1973; Michaut, 2011).

Within our models, we observe a distinct difference between when intrusions generate relief versus then they contribute to crustal thickening. Our results suggest the spatial extent of emplaced intrusions is the dominating process for this difference. If intrusions are constrained to a small area, their inflation culminates into a single, high-relief landform. However, if intrusions are dispersed, small-scale displacements of the surface over an entire region integrates into an overall thickening of the crust. Furthermore, due to our model constraints of defining depth relative to the surface, our models can be considered to be in a statistical steady-state, implying our results will be consistent regardless of the total magmatic volume. These results give some insight into the topographic and crustal volume distributions in volcanic provinces; suggesting that high-relief, focused volcanic centers may have more spatially-constrained underlying magmatic systems that contribute less to overall thickening than more-distributed volcanic zones (Hildreth, 2007; O'Hara et al., 2020).

In order to understand the first-order effects of intrusions on topography, a major process we ignored within our models was surface erosion. However, the relief and elevation gain generated by our models suggests stochastically-emplaced intrusions can have a large impact on landscape evolution. Within the framework of landscape evolution, surface displacement associated with magmatic intrusions act as a localized uplift term. O'Hara et al. (2019) analyzed the effects of single localized uplift perturbations on topographic evolution, finding three regimes of response which contribute to increasing landscape disruption. Here, the size of our intrusions, as well their surface displacement, lets us estimate their overall impact on landscapes.

Within the Poisson spatial distribution models, small-radius (~1 km) intrusions have planform areas (πR^2) that are similar to low-order basins, and generate very small amounts of

relief (< 1 m; Figure 3.1.A). Such intrusions thus correspond to very little surface disruption (Regime 1; O'Hara et al., 2019) on large scales, forming small knickpoints (i.e., local convexities) within river channels. As intrusion radius increases, generating higher relief, landscape disruption will become moderate (Regime 2; O'Hara et al., 2019), creating landforms that behead river channels and form internally-drained basins that uplift as plateaus. However, this disruption is not permanent, and the landform will eventually decay, leading to a basin configuration that is similar to pre-intruded topography. Finally, in the case of very large-radius (~10 km) intrusions, or for the Gaussian distribution models (where local accumulation of small intrusions generates high-relief landforms), the surface will experience a high degree of disruption (Regime 3; O'Hara et al., 2019). Besides beheading river channels and creating internally-drained basins, the landform will become the dominant topographic feature of the landscape, eventually becoming a long-term drainage divide and forcing permanent channel network reconfiguration within the basin.

Finally, although we do not model the thermal and geochemical evolution of crustal-magmatic systems, the stochastically-emplaced nature of our simulations effectively models the elastic response to pluton formation within the crust. Our results can thus provide new interpretations for the correspondence between intrusions at depth and the surface. For example, gravity surveys often employ isostatic response function to analyze compensating crustal thickness (e.g., Krishna, 1996) and heterogeneities in crustal density (e.g., McNutt, 1983). Our results indicate that applying such isostatic response functions to the admittance between topography and gravity may also provide estimates of depth and spatial extent distributions of crustal magmatic bodies in-situ.

Where applicable, geologic reconstruction of magmatically-deformed topography remains a gold standard that can also be used to interpret crustal magmatic systems. A prime example of this is the Henry Mountains (Utah, U.S.), a set of exposed Oligocene-aged laccoliths

located on the Colorado Plateau. Highly-bent sedimentary units along the flanks of the intrusions constrain the elastic deformation of overlying strata during emplacement (Gilbert, 1877; Jackson and Pollard, 1988), and has set the basis for common shallow-intrusion models used today (e.g., Goulty and Schofield, 2008; Galland and Scheibert, 2013). Reconstructing these units using structure-contour data (Gilbert, 1877) generates a surface that can be treated as topography. Applying our methodology, this surface can be inverted to infer depths, thickness, and force distributions of the intrusions. Such analyses are outside the scope of this study, but can be used to better constrain intrusion geometry distributions (e.g, Karlstrom et al., 2018).

5.0 Conclusion

We analyze the extent to which regional-scale magmatism leaves a long-term signature on topography. By expanding single-intrusion models in a stochastic emplacement framework, we simulate topographic response to multiple magmatic intrusions that have varying sizes, depths, and spatial distributions. We show that topographic relief and crustal thickening varies as a function of mean intrusion parameters, providing a simple proxy for analyzing crustal magmatism from topography. Furthermore, we find that the topographic response to distributed magmatism can be approximated using standard plate flexure equations, giving new interpretations for gravity-based data in volcanic settings. Finally, we show the limitations of analyzing intrusion parameters from topography, where spatially-overlapping intrusions present a loss of information to the surface. Despite this, we find that topography can still catalog the spatial extent of intrusive bodies. We postulate that combining our results with topographic analyses of landforms in volcanic provinces to separate signatures of volcanic, magmatic, and erosive processes may provide new methods to estimate crustal magma flux and magmatic system geometry from the surface.

6.0 Bridge

Chapter III explores the role of regional-scale magmatism in generating topography. I found quantitative relationships between distributions of intrusions and the land surface by modeling prolonged shallow crustal magmatism. Through these models, I find that topography can be used to approximate the size and depths intrusive bodies in some scenarios. However, I show that the spatial distribution of intrusions, and intrusion depth, provides a limiting constraint on the amount of information that can be discerned from topography. Combining the stochastic intrusion framework with the landscape evolution models described in Chapter II would provide further insight into understanding landscape response to regional-scale crustal magmatism. Figure 3.9 shows an example of this, where shallow magmatic intrusions were stochastically emplaced within an initial steady-state landscape for 6 Myr, such that uplift from the intrusions contributed a constant 25% to the regional uplift. Transient topography associated with these perturbations follow the results of Chapter II as well as the expectations described in the Discussion section of this chapter. The intrusions generate topographic highs that become increasingly-dissected by channel incision. Furthermore, these landforms behead river channels, generating plateau-like features in the upstream reaches of the basin they perturbed. Future work will expand on this sample model to explore how intrusion sizes, depths, spatial distributions, and emplacement rates impact the erosive response to regional-scale magmatism.

Chapters II and III both take a theoretical approach to understand how intrusive processes effect topographic form and evolution. However, how crustal magmatic structure of volcanic provinces relates to surface volcanism, as well as how these relationships evolve through time, remains unknown. Chapter IV explores these connections. Using a recently-published Quaternary vent database (Ramsey and Siebert, 2017), I estimate edifice volumes from topography within the Cascades Arc (western U.S.). I then compare vent spatial density and edifice volumes to regional geophysical datasets to analyze the relationship between the surface and subsurface. Finally, I

break down the temporal aspect of the Quaternary vent database to understand the evolution the crustal magmatic structure of the Cascades over the last 2.6 Myr.

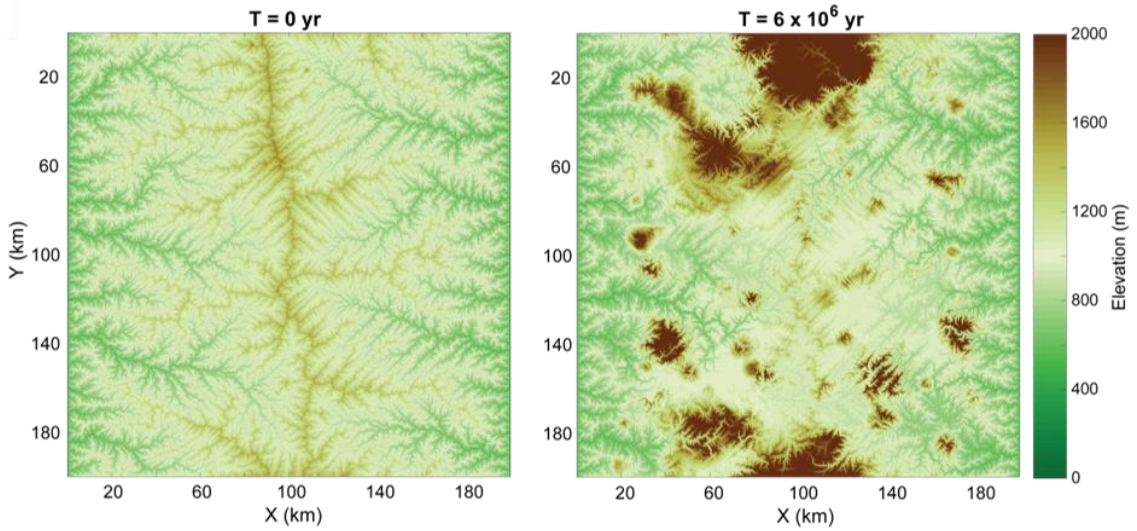

Figure 3.9 – Example stochastic intrusion landscape evolution model. Left panel shows the initial landscape configuration, with a divide along the center and sinks along the left and right sides of the model domain. Right panel shows transient topography after 6 Myr of uplift associated with stochastically-emplaced shallow intrusions.

CHAPTER IV

TIME-EVOLVING SURFACE AND SUBSURFACE SIGNATURES OF QUATERNARY VOLCANISM IN THE CASCADES ARC

From O'Hara, D., Karlstrom, L., and Ramsey, D. W. (2020). Time-evolving surface and subsurface signatures of Quaternary volcanism in the Cascades Arc. *Geology*.

1.0 Introduction

Diversity in the spacing, volume, and morphology of arc volcanoes (e.g. Tamura et al., 2002; George et al., 2016) implies diversity in underlying crustal magmatism. Mapping active structures through the crust to connect volcanism with deeper magmatic processes remains an outstanding challenge. Here, we combine a database of mapped Quaternary vents, surface topography, and diverse geophysical datasets within the Cascades Arc to probe relations between volcanism and underlying crustal structure. Building on prior efforts to synthesize geophysical (e.g., Weaver et al., 1989; Wells et al., 1998; Till et al., 2019) and geologic (e.g., Guffanti and Weaver, 1988; Hildreth, 2007) data in the Cascades, we analyze (1) arc-scale relations among geophysical datasets associated with magmatism; (2) how well volcanoes match geophysical subsurface magmatic signatures and (3) Quaternary time-variations of these relations.

1.1 The Cascades Arc

Volcanism in the N-S trending Cascades Arc is associated with eastward subduction of the Juan de Fuca plate under the North American Plate (Figure 4.1.A). We focus on the U.S. Cascades (~40° - 49°N). Quaternary volcanism consists of notable long-lived (~300-600 kyr; Calvert, 2019) stratovolcanoes aligned parallel to the trench, as well as voluminous off-axis volcanic fields encompassing thousands of vents extending as far as ~50-150 km normal to the trench (Guffanti and Weaver, 1988; Hildreth, 2007). Although clockwise rotation of western Oregon has migrated the arc on ~10 Myr timescales (Wells et al., 1998; du Bray and John, 2011), previous work has not documented consistent Quaternary vent migration (Hildreth, 2007).

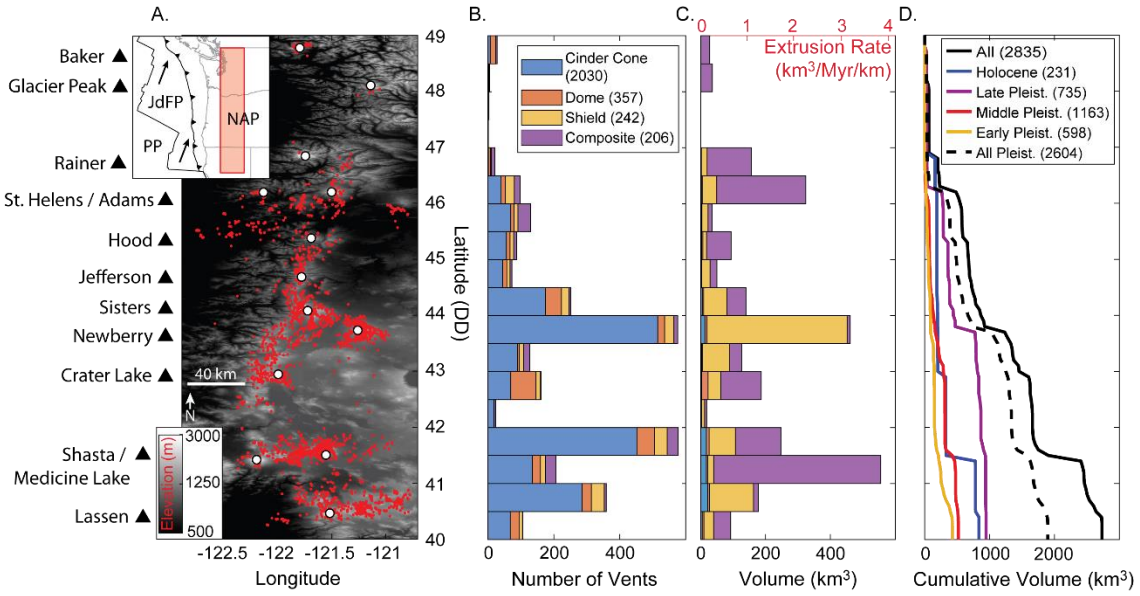

Figure 4.1 – **A:** Quaternary Cascades vent locations (red dots; Ramsey and Siebert, 2017) and main volcanic centers (white circles and black triangles) overlaid on topography (horizontally exaggerated). **B-C:** Along-arc histograms of (B) vents and (C) edifice-based extrusion rates (top axis) and edifice volumes (bottom axis) using 0.5° latitudinal bins (~56 km). Colors correspond to edifice morphology. **D:** Cumulative edifice volumes, separated by epoch of most recent eruption.

1.2 Data

Quaternary mapping of the Cascades reveals volcanic products that span the range of common edifice types and compositions observed on Earth (e.g., Sherrod and Smith, 2000; Hildreth et al., 2012). Ramsey and Siebert (2017) compiled a database containing 2999 vent locations (Figure 4.1.A), along with associated morphological classification and epoch age of the most recent eruption (Holocene, 0-0.01 Ma; Late Pleistocene, 0.01 – 0.1 Ma; Middle Pleistocene, 0.1 – 1.8 Ma; Early Pleistocene, 1.8 – 2.6 Ma).

We compile Cascades geophysical data sets that examine crustal attributes at <~20 km depths and may constrain magma structure. 1) Isostatic residual gravity anomaly data provide a depth-integrated measure of upper-crustal rock density (Blakely et al., 1997), correcting observed gravity for topography and compensating crustal root (Simpson et al., 1986). We do not seek signatures of magmatic crustal thickening (Karlstrom et al., 2014). 2) Seismic tomography involves a combination of rock composition, temperature, and fluid content (Zhao et al., 1992). A

number of tomographic models exist for the Cascades; we use 10s and 15s period phase velocity anomalies (ΔV_{ph}) from a surface-wave model based on both onshore and offshore data, which are sensitive to upper-crustal structures (Janiszewski et al., 2019). 3) Heat flow measurements reflect conductive and advective heat transport in the upper few kilometers of crust, with lateral heat advection by groundwater over ~10s of km-scale (Ingebritsen and Mariner, 2010). 4) Crustal rotation rates derived by regional GPS velocity field measurements record interseismic surface motions (McCaffrey et al., 2013) and approximate large-scale rotation rates over the past ~16 Myr (Wells and McCaffrey, 2013).

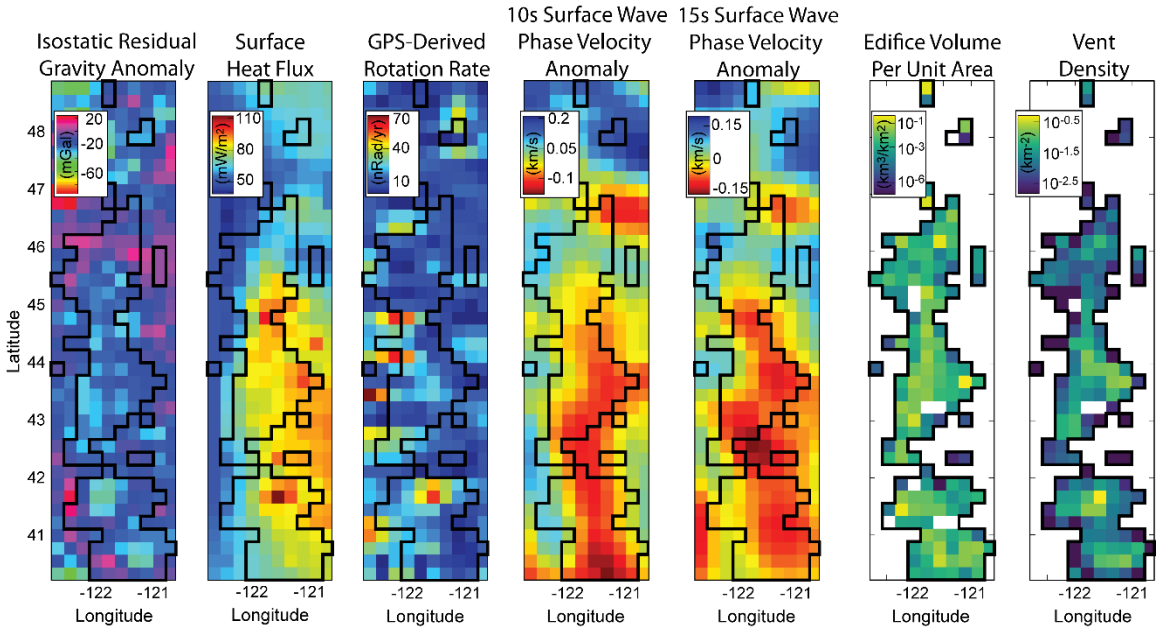

Figure 4.2 – Maps of all used datasets gridded to 25x25 km^2 grid resolution. Black lines encompass Quaternary vents. Largest edifice volume and number of vents within a cell is ~504 km^3 and 265 vents (Mt. Shasta and Medicine Lake, respectively).

2.0 Topographically-Determined Edifice Volumes

To identify surficial signatures of volcanism in the Cascades, we use 10m National Elevation Dataset DEMs (USGS, 2013) to determine topographic extents of volcanic edifices. Generally, edifices are positive topographic structures associated with vents, semi-circular in planview, with slopes higher than surrounding topography (including any satellite vents). Within this section, we discuss our methods for determining edifice boundaries from topography, the

accuracy of our method compared to previously-reported volumes, and our resulting volumes and extrusion rates for the Cascades Arc.

2.1 Edifice Boundary Identification

Volcano topographic boundaries and volumes are determined by the Modified Basal Outlining Algorithm (MBOA; Bohnenstiehl et al., 2012). MBOA first creates a set of topographic contours using a user-defined contour interval. Afterwards, it selects contours that meet a set of criteria; we require that 1) the contour must be closed within the map region (it cannot extend outside of the map), 2) it must be semi-circular both in terms of its overall geometry (we impose an ellipticity limit of 0.3) and must approximate an ellipse shape (using a misfit cutoff of 0.4), and 3) it must be the lowest-most contour of a group with at least 1 other contour contained within it. Once closed topographic contours are selected, MBOA modifies the contour by generating a series of 180 radial profiles centered on the peak of the enclosed topography. The intersections of each profile and the contour are then moved down-profile until the ratio of enclosed cross-sectional area to profile outline perimeter decreases. All points are then reconnected in map view, creating a basal outline around the topographic structure.

To account for edifices of varying scales that are often superimposed spatially, we augment MBOA with a semi-automated process that determines regions of interest and spatial scales with which to use MBOA on a local-scale DEM. Figure 4.3 provides an example of the process for the Three Sisters volcanic complex (OR). Starting with a 10m-resolution DEM (Figure 4.3.A), we calculate local topographic slopes over the region (Figure 4.3.B), and generate a hypsometric curve of surface slopes (i.e. a cumulative density function of the relationship between slope and area, normalized by the total map area; Figure 4.3.C). We postulate that the highest slopes are associated most with volcanic edifices, and find through experimentation that a slope value higher than the slopes that cover 80% of the map area generally picks out volcanoes (S_C; dashed line of Figure 4.3.C). Using this value, we generate a binary map of pixels with slope

values greater than S_C (Figure 4.3.D). We then perform a 2D low-pass filter on this map using 1000m and 300m cutoff wavelengths (Figure 4.3.E; Perron et al., 2008). Similar to MBOA, we then determine contours that meet criteria 1-3 in the above paragraph – these are now considered regions of interest. The DEM is cut around these regions and processed with MBOA, using a contour interval that is 5% of the total relief of the cut DEM, thus ensuring that criteria 3 can be met regardless of grid resolution. The boundaries determined by MBOA are then manually inspected and paired with database vents. Afterwards, edifice volumes are calculated as the integral of bounded topography, with small-scale structures such as parasitic cones subtracted from underlying edifices.

The result is a set of boundaries and associated volumes that encompass edifices of multiple scales and morphologic types (Figure 4.3.F), ranging from 10's of m-scale cinder cones to 10's of km-scale stratovolcanoes. Field analysis of select cinder cones around Newberry (OR) was conducted to determine the accuracy of DEM-derived boundaries to that expected from topography within an order of 10's of meters. We ignore topography associated with dispersed eruption deposits. Furthermore, we do not account for buried vents, nor for syn- or post-construction erosion; however, distributions of edifice volumes are similar for all epochs in our dataset (Figure 4.4), suggesting erosion does not bias our results.

We limit this analysis to cinder cones, domes, shield volcanoes, and composite volcanoes, giving a total of 2835 analyzed vents. Of these, we determine boundaries for 2105 vents. The remaining vents of considered types were not paired with topography because edifice boundaries could not be adequately determined at the 10m DEM resolution using our procedure. Often, this was due to the topography around an edifice being too noisy (i.e. containing high-amplitude, short-wavelength topographic features) or having an otherwise obscure topographic form (such as an underlying ridge), so that MBOA could not delimit the edifice from topography. In some cases, MBOA determined breached cinder cone boundaries that encompassed associated

lava flows and thus extended beyond the cone. These boundaries were also excluded from our analysis to keep volumes constrained to only edifices. To estimate volumes for all considered vent types, we assume that vents not paired with topography have volume equal to the average volumes of each morphologic type.

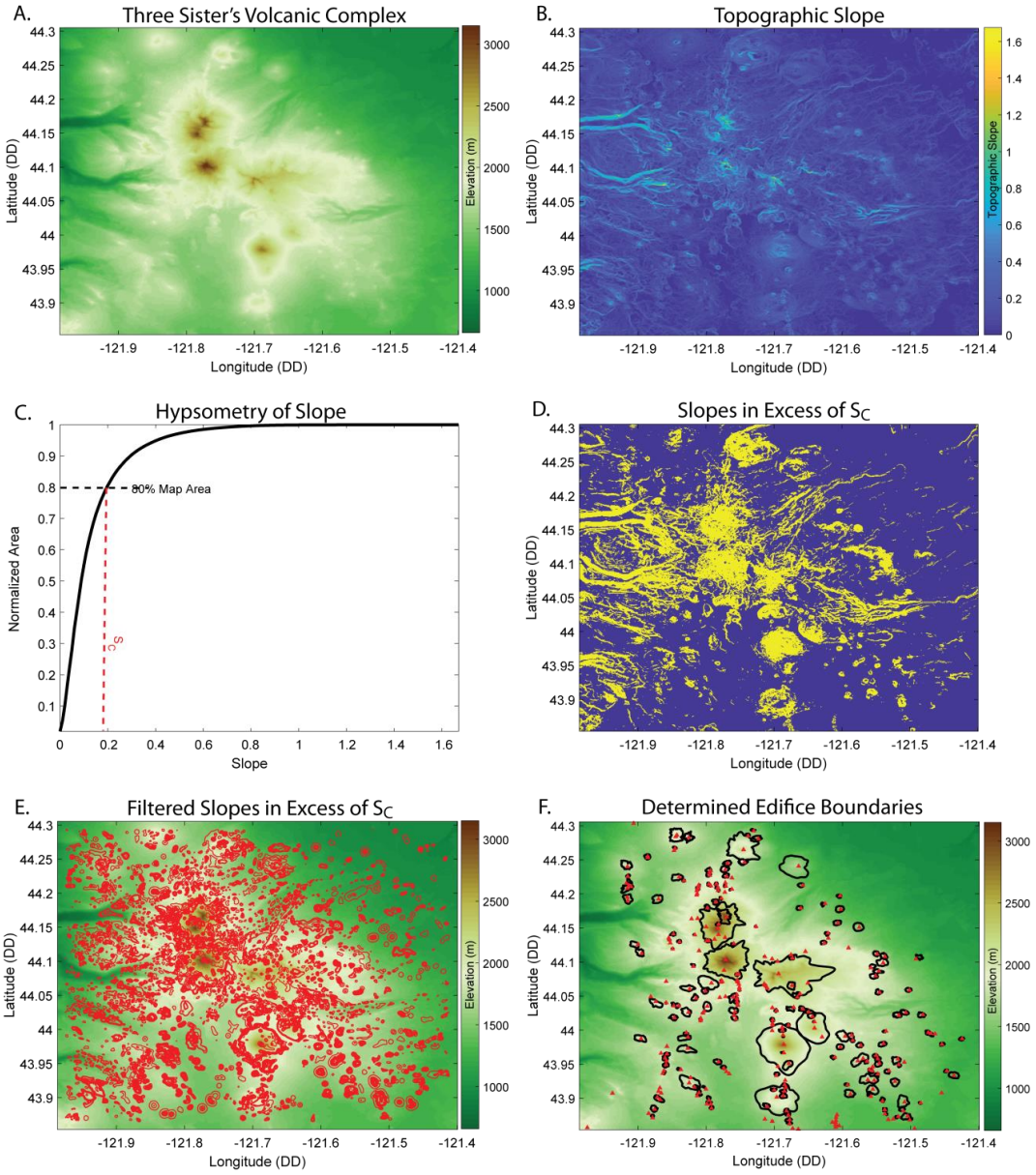

Figure 4.3 – Edifice boundary identification for the Three Sisters volcanic complex (OR). **A**: Raw elevation data. **B**: Map of topographic slopes. **C**: Hypsometric plot showing the normalized area – topographic slope relationship for the Three Sisters complex. Red-dashed line shows the critical slope $\boldsymbol{S_C}$ that corresponds to the 80th percentile of map area (black-dashed line). **D**: Binary map showing locations of slope values above (yellow) and below (blue) the critical value $\boldsymbol{S_C}$. **E**: Contours (red lines) of the low-pass filtered logical map (using a 300m filter wavelength). **F**: Selected edifice boundaries (black lines) from MBOA, red triangles are known vent locations. 223 out of 288 (77%) vents in the map area were paired with topographic contours.

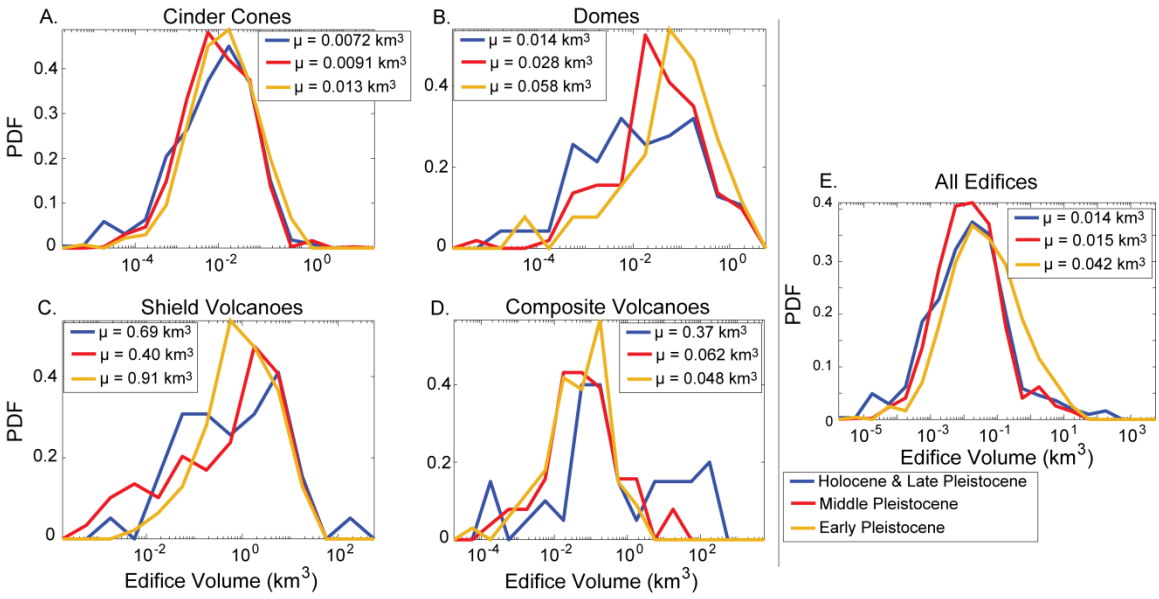

Figure 4.4 – Topography-derived edifice volume distributions for (**A**) cinder cones, (**B**) domes, (**C**) shield volcanoes, (**D**) composite volcanoes, and (**E**) all morphologic types, separated by epoch. Plot insets list mean volumes $\boldsymbol{\mu}$ for each epoch.

The other 165 vents within the database are fissure vents (110) and vents associated with phreatomagmatic eruptions (56). Although fissure vents can generate large-volume lava flows (e.g., Clynne and Muffler, 2010), the topography around the vent that can be defined as an edifice within our framework is small. For example, topographic volume determination of 14 fissure vents north of the Newberry caldera using our method generated values ranging ~$4x10^{-7}$ – $3x10^{-3}$ km^3, with a mean volume of ~$8x10^{-4}$ km^3. Similarly, phreatomagmatic eruptions often generate negative topography, such that volume cannot be determined using our method. Thus, these vents are excluded from our analysis.

2.2 Edifice Boundary Error Analysis

Determining the bounds of a volcanic edifice is, in general, a challenging and non-unique exercise. Various methods have been developed. Geologic mapping represents perhaps the most accurate method, provided eruptive contacts are visible and intact. Published geologic maps at sufficient resolution do not exist for large sections of the Cascades, but geologically determined volumes of major stratovolcanoes have been compiled (e.g., Hildreth, 2007, and references

therein). Determining boundaries from satellite-derived DEMs provides a more comprehensive and self-consistent method, and one that can be applied to any volcanic region. In addition to the method described here, NETVOLC (Euillades et al., 2013) is another algorithm that identifies edifice boundaries from DEMs. Rather than using radial profiles to determine changes in slope, NETVOLC combines topographic curvature, aspect, and local slope to generate a weighted cost map that is iteratively analyzed in polar coordinates around an approximated volcano center point to determine the boundary associated with the lowest cost.

We assess the accuracy of our method by comparing our topographically-determined edifice volumes to those determined by geologic mapping and NETVOLC, as reported by Hildreth (2007) and Grosse et al. (2014), respectively. Table 4.1 lists the values of each study for reported edifices, as well as the percent difference of our values relative to previously-reported values, such that negative values indicate larger volumes estimated by this study. We determine outliers between datasets as those that have a percent difference value outside a standard 1.5 interquartile range between the 1st and 3rd quartile.

The most striking outliers are Mt. Baker and the Lassen Volcanic Center, where our algorithm significantly over-estimates volumes compared to other studies, and the Belknap shield, where our algorithm significantly under-estimates volumes. These discrepancies can be explained by the automatically-defined regions of interest determined by regional slope hypsometry within our algorithm. For example, Figure 4.5 shows the identified boundary for Lassen. Based on regional slopes, our automated algorithm determined a region of interest (and thus edifice boundary) that encompassed the Lassen domefield (Figure 4.5, black line) (Clynne and Muffler, 2010), from which a volume of ~77.4 km^3 was estimated (excluding volumes of smaller, overlapping edifices). However, manually choosing a smaller region of interest, while keeping all other parameters the same, causes MBOA to define a boundary only around Lassen Peak (Figure 4.5, red line). This smaller boundary gives a volume estimate of 2.7 km^3, which is

more comparable to those reported by Hildreth (2007) and Grosse et al. (2014) (2.5 and 2.1 km^3, respectively).

Name	State	O'Hara et al. (this study) Volume (km^3)	Hildreth (2007) Volume (km^3)	Grosse et al. (2014) Volume (km^3)	% Volume Difference (km3)	
					Hildreth (2007)	Grosse et al. (2014)
Mt. Baker	WA	144.9	15	36.8	-866.00	-293.75
Glacier Peak	WA	15.3	30	22	49.00	30.45
Mt. Rainier	WA	126.6	130	99	2.62	-27.88
Mt. Adams	WA	165.1	210	48	21.38	-243.96
Mt. St. Helens	WA	36.6	25	16.2	-46.40	-125.93
Mt. Hood	OR	58.2	60	71	3.00	18.03
Mt. Jefferson	OR	22.5	20	27.1	-12.50	16.97
Three Fingered Jack	OR	10	10		0.00	
Mt. Washington	OR	4.8	15		68.00	
Belknap shield	OR	0.07	10	6.1	99.30	98.85
Black Butte	OR	6.3	10		37.00	
Black Crater	OR	3.2	7		54.29	
North & Middle Sister	OR	8.5	27	6.1	68.52	-39.34
South Sister	OR	8.3	20	8.8	58.50	5.68
Broken Top	OR	11.5	10		-15.00	
Mt. Bachelor	OR	10.4	25	4.2	58.40	-147.62
Newberry	OR	294.7		120		-145.58
Maiden Peak	OR	12.2	12		-1.67	
Diamond Peak	OR	18	15		-20.00	
Odell Butte	OR	4.8	7		31.43	
Cappy Mountain	OR	1.9	25		92.40	
Mt. Bailey	OR	14.5	15		3.33	
Mt. Mazama	OR	83.4	120		30.50	
Mt. McLoughlin	OR	9.9	13		23.85	
Mt. Shasta	CA	171.5	450	147	61.89	-16.67
Mt. Magee	CA	13.9	10		-39.00	
Lassen Volc Center	CA	77.4	2.5	2.1	-2996.00	-3585.71
				Mean Absolute Difference:	183.08	342.60
				Mean Absolute Difference (Without Outliers):	32.10	92.66

Table 4.1 – Volume comparisons of edifices between this study and those reported by Hildreth (2007) and Grosse et al. (2014). Negative percent volume differences indicate volumes reported in this study are greater than those previously reported, red text indicates outliers in the percent volume difference of each comparison. Note that we use the Hildreth volumes for all vents listed here in calculations performed in the main text.

Similarly, the Belknap shield has slope values that are small compared to surrounding topography, such that our algorithm picked a region of interest that encompassed only the topography near the vent, causing a lower volume estimation compared to previous studies. This provides useful context to understand why our method generates erroneous values. Our method assumes topographic attributes that are common to most edifices: a quasi-conical primary landform with steep slopes that may have smaller superimposed vents. The method fails when it encounters complex edifice morphologies, such as when slopes are not steep (e.g., the Belknap shield), or when satellite topographic features of similar scale obscure the primary landform (e.g., the Lassen domefield)

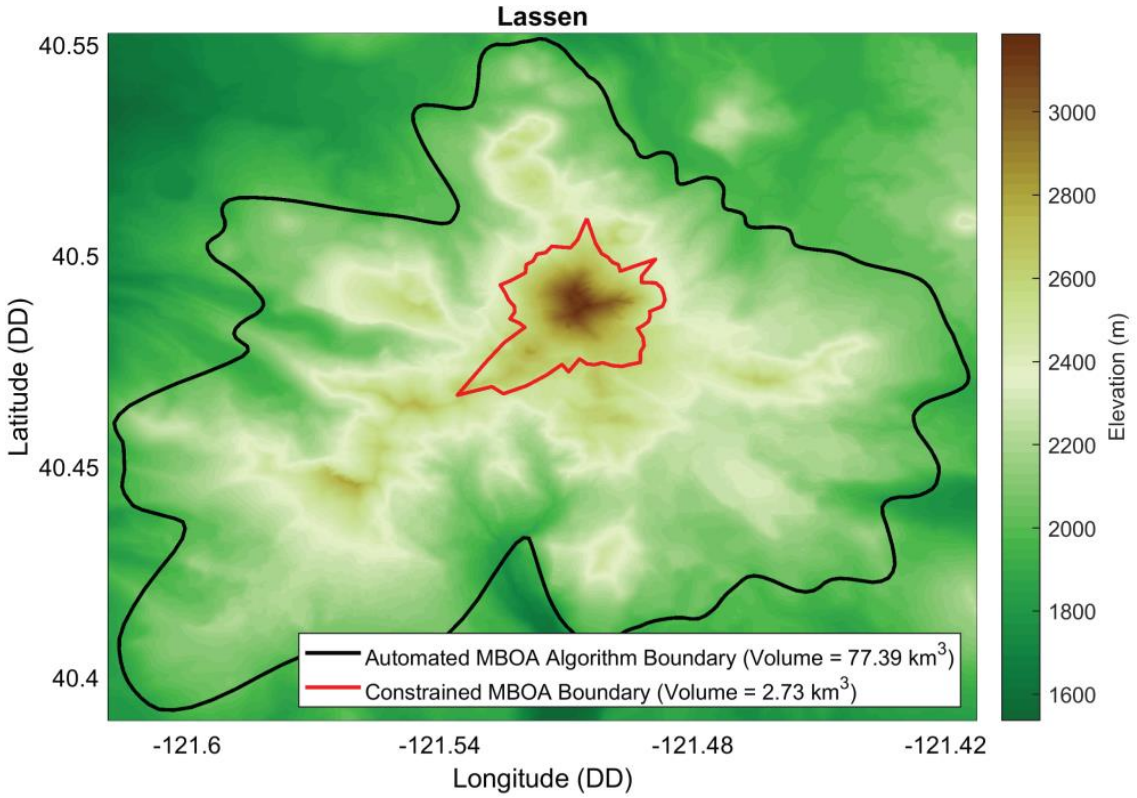

Figure 4.5 – MBOA edifice boundaries for Lassen. Black line shows the automated boundary selection used for this study (i.e., Lassen domefield); red line shows the boundary generated by a smaller region of interest (i.e., Lassen Peak).

Despite these outliers, we find our volume estimates compare well with those previously reported. Figure 4.6 shows the distribution of these differences as histograms, labels correspond to edifices with the largest volume differences. Our volume estimates differ from Hildreth (2007)

in mean absolute percent differences by ~32% and from Grosse et al. (2014) by ~92%. There seems to be no consistent trend in these differences. However, volumes generated by MBOA are generally larger compared to NETVOLC, and more closely match those reported by Hildreth (2007). This lack of consistency suggests there is room for more accurate edifice boundary identification and volume estimation methodologies that can incorporate both geologic and topographic data. For the purposes of arc-scale comparison between thousands of edifices, our method is a transparent and self-consistent edifice boundary identification tool. However, assuming detailed geologic mapping is generally more accurate, we use estimates in Hildreth (2007) and Bacon and Lanphere (2006) for major stratovolcano volumes in the subsequent analyses, acknowledging the important role of auxiliary data in volume estimates where available.

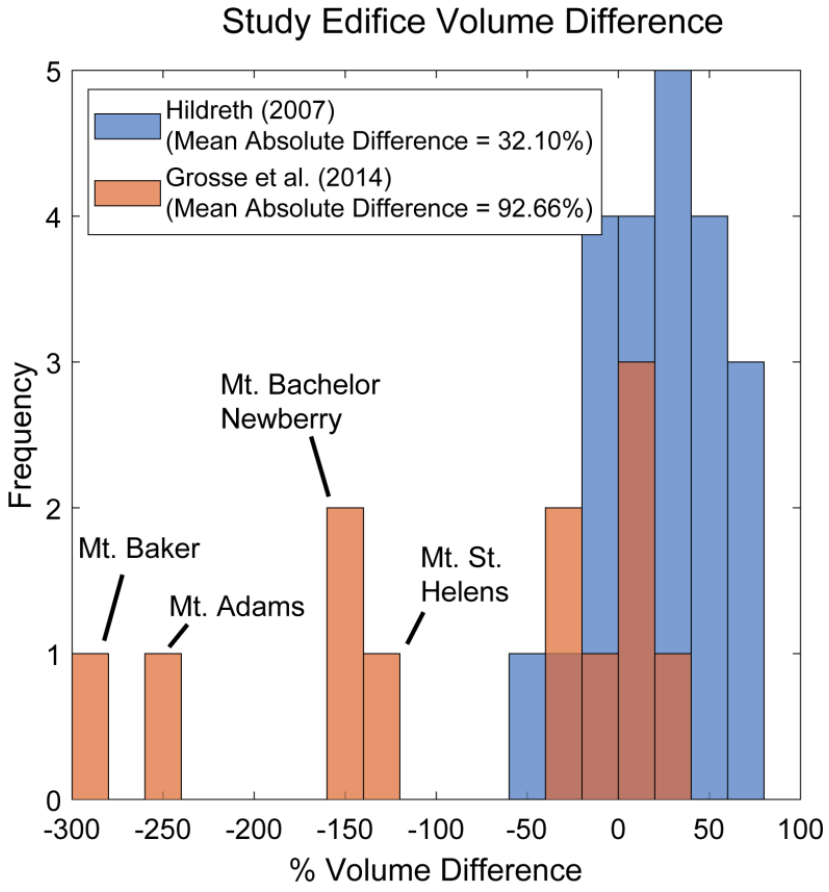

Figure 4.6 – Percent volume differences between this study and others, ignoring outliers listed in Table 4.1. Negative volume difference indicates larger volumes calculated by our method.

2.3 Cascades Edifice Volumes

Using our method, we calculate a total minimum Quaternary edifice volume of ~2730 km^3, implying a minimum extrusion rate of ~1.05 km^3/km/Myr for the ~1000 km length of the study area and 2.6 Myr of the Quaternary (Tables 4.2-3). Figure 4.1.B-C shows the spatial distribution of edifice numbers, volumes, and extrusion rates. Figure 4.1.D shows the cumulative arc-scale volume of edifices by epoch.

Our estimated volumes are nearly identical to the ~2570 km^3 estimated by Sherrod and Smith (1990) that included erupted deposits within the U.S. Cascades. Hildreth (2007) updated this, estimating Quaternary erupted volume of the entire Cascades to be ~ 6400 km^3. If Hildreth's estimate is correct, then current edifice volumes account for ~50% of total Cascades output. Although glacial erosion is variably significant (Hildreth, 2007), if we assume that missing volume comes mostly from deposits, total extruded volumes are roughly twice the volume of edifices alone.

Vent Type	Number of Database Vents	Vents Paired with Topography	Paired Percentage	Paired Mean Volume (km^3)	Total Volume (km^3)	Total Arc Extrusion Rate (km^3/Myr/km)
Cinder Cone	2030	1501	73.9	0.06	103	0.040
Dome	357	250	70.0	0.21	67	0.026
Shield	242	193	79.8	4.57	1020	0.393
Composite Volcano	206	161	78.2	8.16	1549	0.596

Table 4.2 – Table listing vent database and collected edifice value statistics separated by edifice type. Paired Mean Volume is the mean topographically derived volume for each morphologic type that had a determined topographic boundary; Total Volume is the sum of all volumes within the database, including the topographically derived volumes and mean volumes used for vents that did not have a defined topographic boundary. Total Arc Extrusion Rate is calculated as Total Volume / 2.6 Myr / 1000 km (timespan of Quaternary and along-arc study area length).

Vent Epoch	Number of Database Vents	Vents Paired with Topography	Paired Percentage	Paired Mean Volume (km^3)	Total Volume (km^3)
Holocene	219	121	55.3	0.09	20
Pleistocene (Ambiguous)	85	67	78.8	0.03	2
Late Pleistocene	661	413	62.5	0.06	43
Middle Pleistocene	1011	827	81.8	0.07	72
Early Pleistocene	411	323	78.6	0.08	33

Table 4.3 – Table listing monogenetic vent database and collected edifice value statistics separated by epoch. Paired Mean Volume and Total Volume are same as those defined for Table 4.2.

3.0 Subsurface Structures

We analyze the Quaternary crustal magma structure within the Cascades by synthesizing and correlating multiple datasets. The geophysical datasets vary in spatial resolution and scale: the isostatic residual gravity anomaly data (Kucks, 1999) spans the entire continental U.S.A. and has a grid resolution of ~5 km; surface heat flux (Ingebritsen and Mariner, 2010), interseismic GPS-derived rotation rates (McCaffrey et al., 2013), and seismic surface-wave phase velocity (Janiszewski et al., 2019) datasets are all limited to the Pacific Northwest and (for seismic data) the surrounding offshore region, with grid resolutions of ~3km, ~6km, and ~33km, respectively.

To compare gridded regional data of different resolutions, we interpolate all datasets to the same resolution. Choosing the lowest resolution dataset would be the most conservative choice (~33 km; seismic surface-wave phase velocities), but some details of the finer-resolution grids may be lost. We therefore strike a balance in resolution, choosing a 25x25 km^2 grid spacing (Figure 4.2) which is within the range of dataset resolutions and approximately twice the median diameter of all stratovolcanoes within the study area.

After interpolating the geophysical datasets to a common grid, we incorporate edifice volumes and vent densities into our analysis by calculating the logarithmic value of total edifice volume and number of vents per grid cell area (625 km^2; Figure 4.2). We then analyze the

relationships between the gridded regional datasets, vent distributions, and edifice volumes by performing correlation analyses between datasets. The correlation coefficient (C) between two datasets (A and B) is defined as (Kutner et al., 2005)

$$C(A,B) = \frac{1}{N_o - 1}\sum_{i=1}^{N}\left[\left(\frac{A_i - \mu_A}{\sigma_A}\right)\left(\frac{B_i - \mu_B}{\sigma_B}\right)\right], \quad (4.1)$$

where N_o is the number of observations, and μ and σ are mean and standard deviation of each dataset, respectively. The range of the correlation coefficient is ($-1 \leq C \leq 1$), where positive values indicate a positive relationship between the datasets, negative values indicate a negative relationship, and 0 indicates no relationship. The correlation p-value represents the statistical significance to reject the null hypothesis of no correlation between two datasets; we use a typical value of 0.05.

We first assess structures not associated explicitly with vents (Figure 4.7.A) by considering regional gridded datasets alone, over the area plotted in Figure 4.1.A. Next, we linearly interpolate gridded data to the analyzed 2835 vent locations to identify structures underneath volcanoes (Figure 4.7.B). Finally, we subdivide vent data further into epochs (Figure 4.7.C-F). For comparison across the interpolated-data correlation matrices, we calculate a mean absolute C. Because the vent database records only the most recent eruption for an edifice, we limit temporal analysis to monogenetic vents to mitigate bias from long-lived volcanoes. Figures 4.8-12 show the bivariate plots and linear regression analysis of each dataset interpolated to all Quaternary vents and monogenetic vents of each individual epoch. Plot insets provide the linear regression equation, regression R^2 value, and correlation coefficient.

3.1 Correlation Results

Both the number and magnitude of correlations substantially increase amongst regional datasets when interpolated to vents compared to regional grids alone (Figures 4.7.A-B). The most significant relations are consistent with a magmatic origin (Figure 4.7.G). For example, magma-

driven temperature or melt anomalies should contribute to lower seismic velocities and isostatic residual gravity, while increasing surface heat flux. These relations are all observed (Figure 4.7.B), and additionally correspond to higher vent density, larger edifices, and increased elevations (e.g., Cao et al., 2016; Deng et al., 2017). Rotation rate is uncorrelated to other regional gridded data, yet strongly covaries when interpolated to vents, suggesting magmatic influence on crustal deformation near volcanoes. We therefore interpret correlations between vent density and these geophysical datasets as defining magmatic structures in the upper crust linked to volcanic expression.

Correlation magnitudes are generally higher for Holocene versus Early Pleistocene vents (Figure 4.7.C,F). In spite of coarse temporal resolution, this decrease suggests older edifices no longer overlie active magmatic structures, especially considering monogenetic vents are most numerous in the earliest epochs (Table 4.3).

3.2 Sensitivity Tests

To assess the effect of grid resolution on our results, we conduct a sensitivity test of the dataset correlations. We use the mean absolute correlation coefficient (Mean $|C|$; Figure 4.7) between gridded and interpolated data correlation matrices as metrics of grid resolution. Furthermore, we determine the difference between each interpolated-data correlation matrix and the gridded-data correlation matrix by calculating a Euclidian distance (D_E), defined as

$$D_E = \sqrt{\sum_{i=1}^{N_C} (C_C(i) - C_G(i))^2}, \tag{4.2}$$

where C_C and C_G are the i'th correlation coefficient of the interpolated-data and gridded-data correlation matrices, respectively, and N_C is total number of independent correlation coefficients between datasets. The mean $|C|$ thus provides an overall assessment of the correlation coefficient

matrix, while D_E measures the total distance between the gridded and interpolated data correlation matrices for each grid resolution.

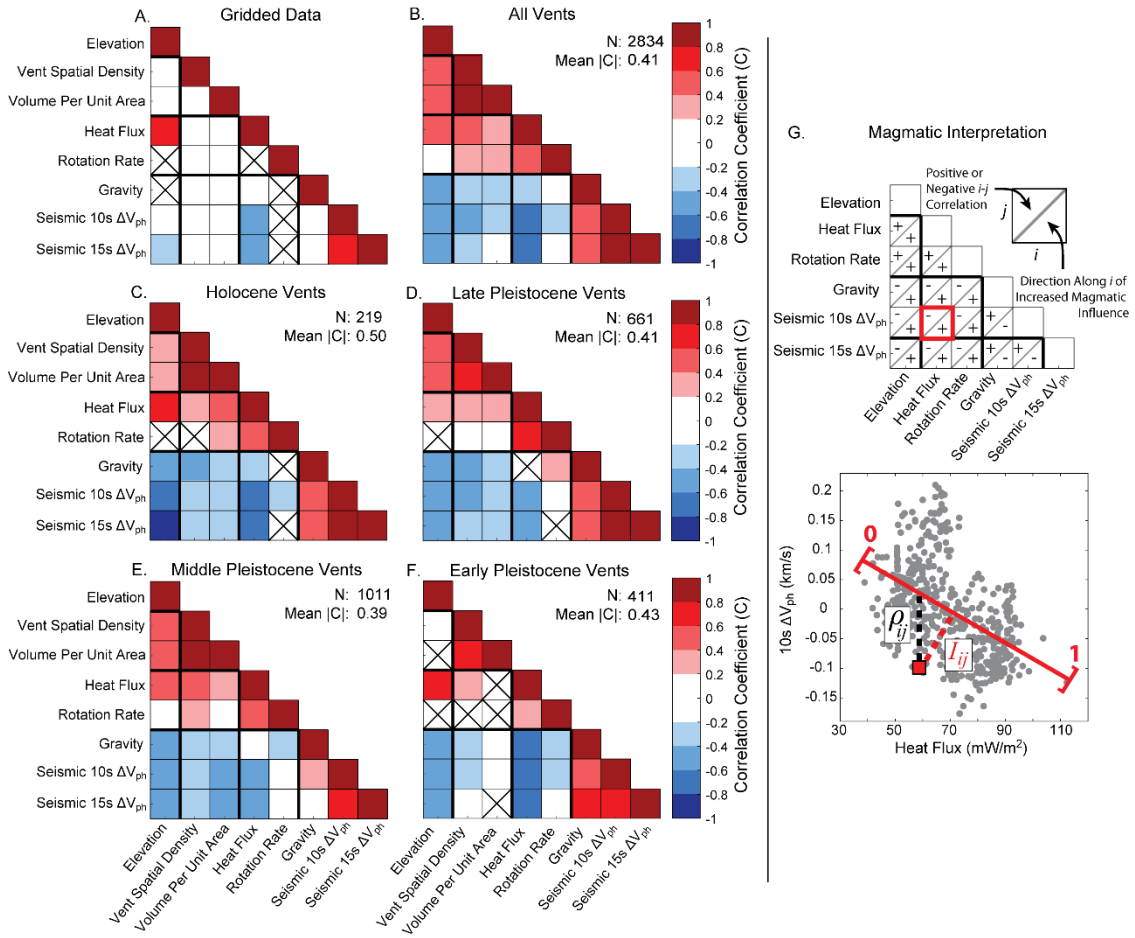

Figure 4.7 – A-F: Data correlation coefficient matrices. Rows and columns correspond to datasets; X's indicate p-values > 0.05. **A:** Regional data evaluated over the area in Figure 4.1.A gridded to 25 km. **B-F**: Same data as (A), interpolated to (B) all Quaternary vents, (C) Holocene monogenetic vents, (D) Late Pleistocene monogenetic vents, (E) Middle Pleistocene monogenetic vents, and (F) Early Pleistocene monogenetic vents. **G:** Top panel: Interpretations of bivariate relations that signify crustal magmatism, including the expected correlation sign and direction along dataset $\boldsymbol{i}$ of increasing magmatic influence. Bottom panel: Example bivariate relation interpolated to all Quaternary vents (gray dots). Black-dashed line shows Studentized residual $\boldsymbol{\rho_{ij}}$ at a point (red square). Red-dashed line is the weighting factor $\boldsymbol{I_{ij}}$ used in equation (4.4).

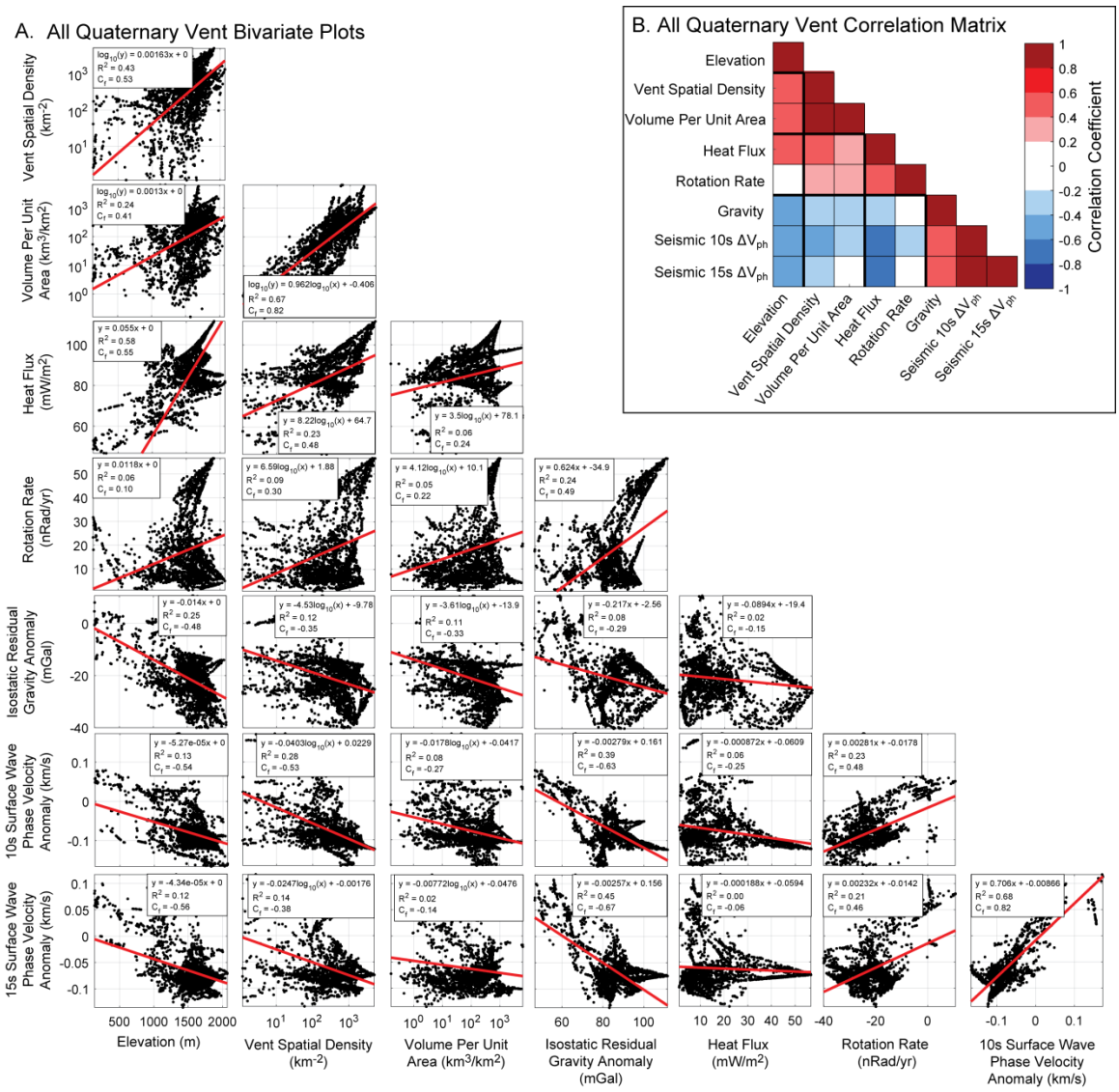

Figure 4.8 – **A**: Bivariate plots of gridded and topographically-derived data interpolated to all Quaternary vents with plot rows and columns corresponding to datasets. Within each bivariate plot, red lines are linear regression model of the data, with insets displaying the linear regression equation, R^2 value, and correlation coefficient (*C*; Equation 4.1). Thickened-bordered plots have a correlation p-value greater than 0.05. **B**: Correlation coefficient matrix for all Quaternary vents described in Figure 4.7.

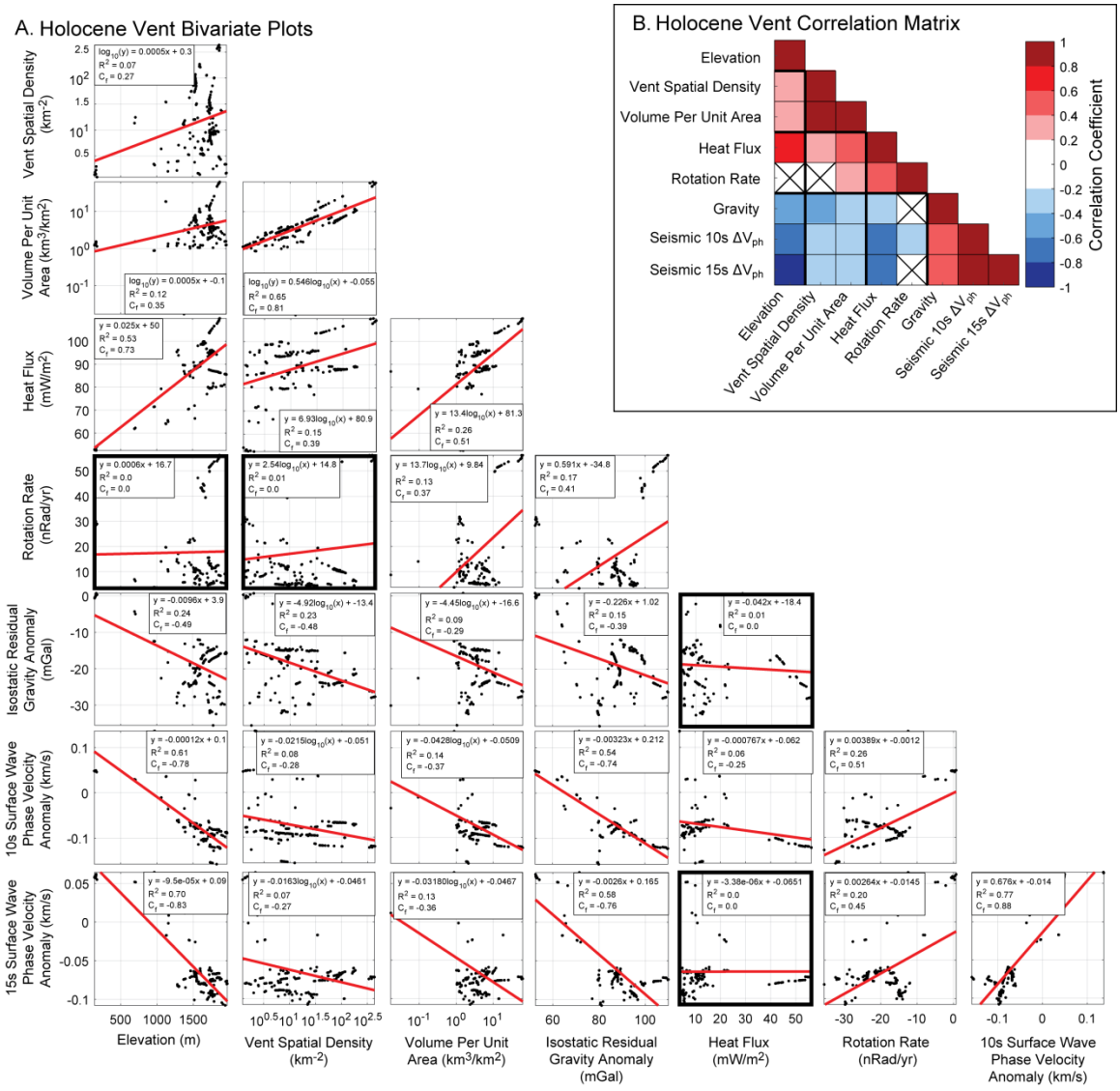

Figure 4.9 – **A**: Bivariate plots of gridded and topographically-derived data interpolated to monogenetic Holocene vents with plot rows and columns corresponding to datasets. Within each bivariate plot, red lines are linear regression model of the data, with insets displaying the linear regression equation, R^2 value, and correlation coefficient (*C*; Equation 4.1). Thickened-bordered plots have a correlation p-value greater than 0.05. **B**: Correlation coefficient matrix for all Quaternary vents described in Figure 4.7.

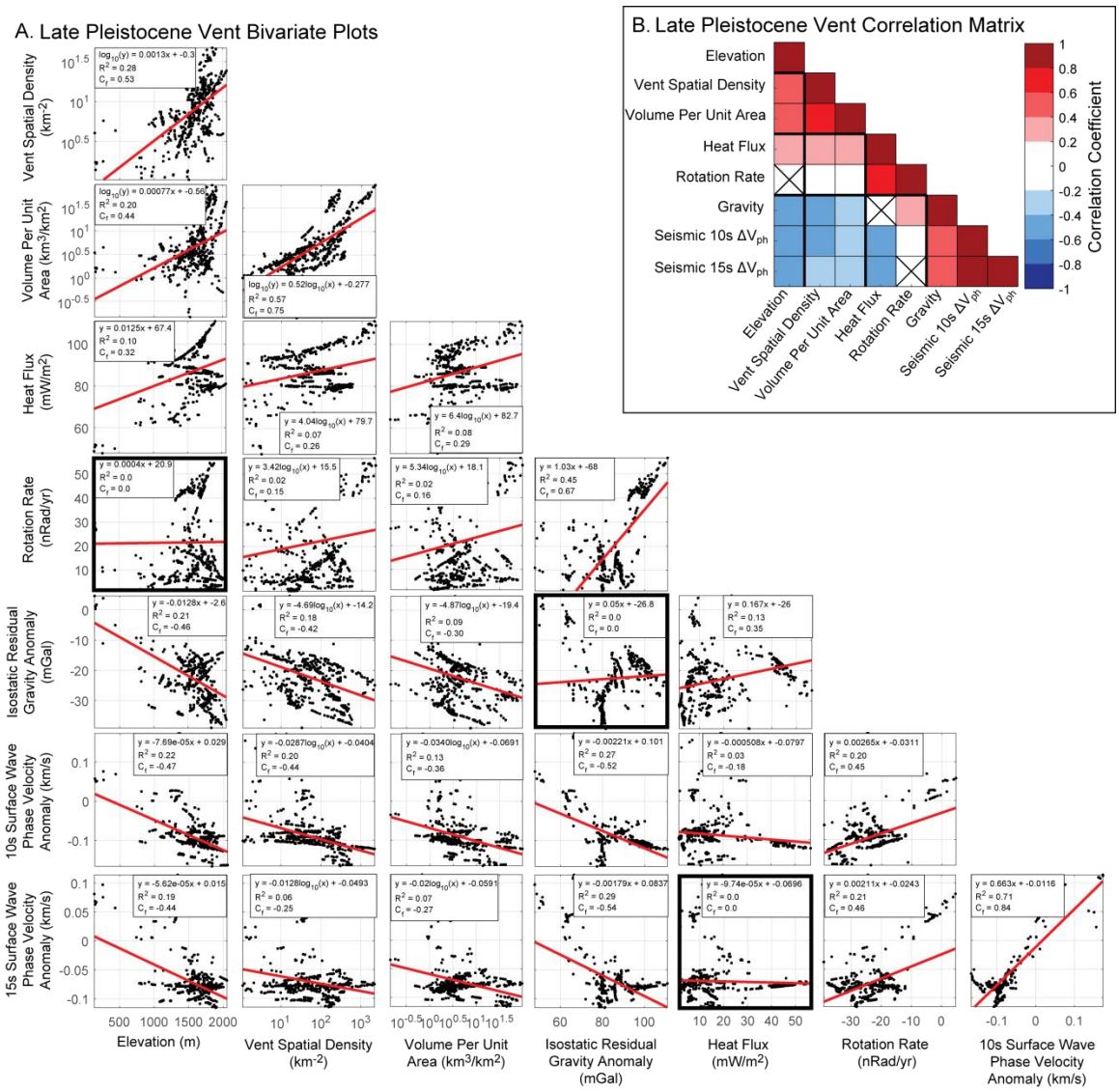

Figure 4.10 – **A**: Bivariate plots of gridded and topographically-derived data interpolated to monogenetic Late Pleistocene vents with plot rows and columns corresponding to datasets. Within each bivariate plot, red lines are linear regression model of the data, with insets displaying the linear regression equation, R^2 value, and correlation coefficient (*C*; Equation 4.1). Thickened-bordered plots have a correlation p-value greater than 0.05. **B**: Correlation coefficient matrix for all Quaternary vents described in Figure 4.7.

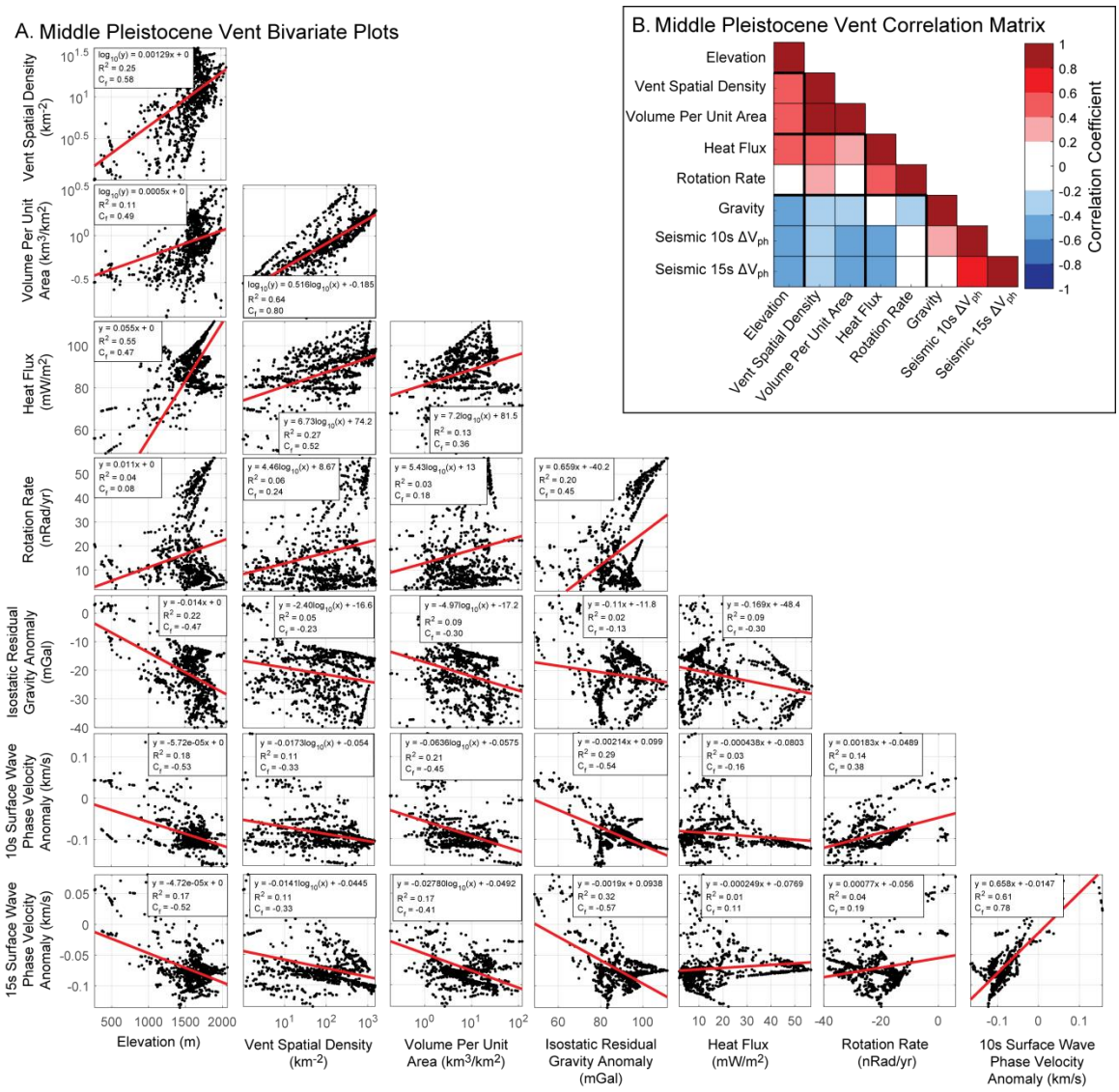

Figure 4.11 – **A**: Bivariate plots of gridded and topographically-derived data interpolated to monogenetic Middle Pleistocene vents with plot rows and columns corresponding to datasets. Within each bivariate plot, red lines are linear regression model of the data, with insets displaying the linear regression equation, R^2 value, and correlation coefficient (*C*; Equation 4.1). Thickened-bordered plots have a correlation p-value greater than 0.05. **B**: Correlation coefficient matrix for all Quaternary vents described in Figure 4.7.

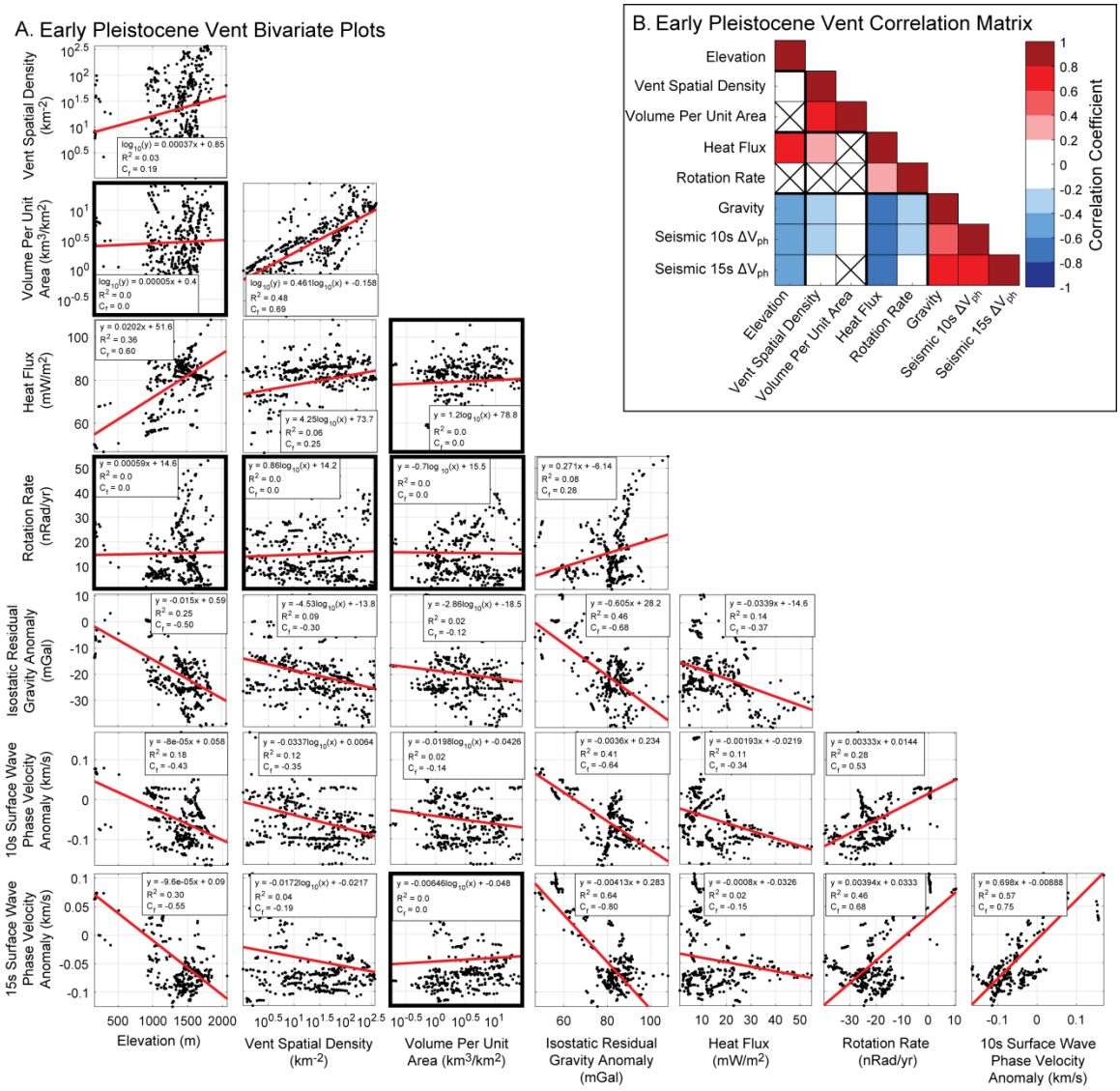

Figure 4.12 – **A**: Bivariate plots of gridded and topographically-derived data interpolated to monogenetic Early Pleistocene vents with plot rows and columns corresponding to datasets. Within each bivariate plot, red lines are linear regression model of the data, with insets displaying the linear regression equation, R^2 value, and correlation coefficient (C; Equation 4.1). Thickened-bordered plots have a correlation p-value greater than 0.05. **B**: Correlation coefficient matrix for all Quaternary vents described in Figure 4.7.

Figure 4.13 shows the values of these metrics for datasets interpolated to all Quaternary vents and monogenetic vents of each epoch using grid resolutions ranging 10-40 km. Overall, we find that grid resolution has a low impact on the absolute magnitudes and relative temporal magnitudes of these metrics. Holocene vent interpolations seem most sensitive to grid resolution. Across all interpolated datasets, coarser grid resolutions cause lower D_E as gridded and interpolated data approach similar correlation values.

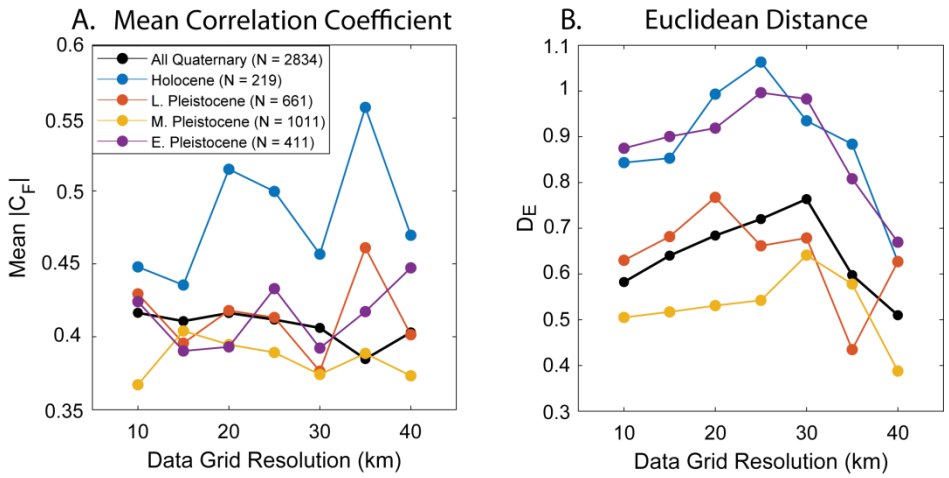

Figure 4.13 – Sensitivity tests of vent correlation matrices for a variety of interpolated grid resolutions. Colors correspond to dataset epochs. **A**: Mean absolute correlation coefficient. **B**: Euclidean distance ($\boldsymbol{D_E}$; Equation 4.2) between regional gridded data and interpolated data correlation matrices.

4.0 What are the Subsurface Signatures of Arc Volcanoes?

Figure 4.7 indicates surface-subsurface correlations exist at volcanic edifices, but does not reveal arc-scale patterns. We examine this spatial structure using independent metrics of surface and subsurface data. We assess surface data with a volume-weighted Gaussian kernel function λ(x,y) that measures spatial vent density and edifice volumes as a probability density function (e.g., Connor et al., 2019), defined as

$$\lambda(x,y) = \frac{\Delta x^2}{2\pi h^2 V} \sum_{e=1}^{N_V} v_e \exp\left[-\left(\frac{v_e d_e(x,y)}{4h}\right)^2\right], \tag{4.3}$$

where h is a kernel bandwidth (25 km), Δx is grid resolution (25 km), N_v is total number of vents, and $d_e(x,y)$ is the Euclidean distance between point (x,y) and a vent (x_e, y_e). v_e is the volume of an individual edifice and V is the summed volume of all edifices.

We also measure the extent to which subsurface data provide a coherent indication of magmatic structure, but models that relate data physically (e.g., gravitational admittance or Nafe-Drake curve) are not similarly comparable. Therefore, we assess a relative extent of magmatic influence between datasets with linear bivariate relations. We assume the magnitude of the correlation coefficient C_{ij} reflects arc-averaged significance (Figure 4.7.A-F), then scale a given

location with a number $I_{ij}(x, y)$ between 0 and 1 measuring the likely magmatic significance for vent-interpolated data at that point relative to the entire dataset (Figure 4.7.G). Finally, we use a Studentized residual between bivariate data and a linear regression of the vent-interpolated bivariate relation (ρ_{ij}; Figure 4.7.G) to down-weight points that fall off the regional trend. The combined magmatic signature of all datasets is then calculated as

$$G(x, y) = \sum_{i=1}^{N_D} \sum_{j=i+1}^{N_D} \frac{|C_{ij}| I_{ij}(x, y)}{1 + |\rho_{ij}(x, y)|}, \tag{4.4}$$

where N_D is the total number of datasets. Equation (4.4) thus combines both arc- and local-scale covariations of multiple geophysical datasets.

Correlation of geophysical data measured by G is largest in central Oregon and generally increases to the south, with more subdued peaks associated with the Caribou and Simcoe volcanic fields, Medicine Lake, Mt. Mazama, and Mt. Hood (Figure 4.14.A). This pattern is mimicked but more focused in λ (Figure 4.14.B), in part because weighting vents by volume localizes λ around the large edifices. Broad monogenetic vent fields are also prominent, illustrating the significant distributed volcanism in the central and southern Cascades.

Finally, we note that edifice volumes and vent spatial density distributions covary, both peaking around the Mt. Shasta/Medicine Lake latitude. The extent of variation relative to this area thus measures distributed versus focused styles of volcanism. Normalized vent number and edifice volume distributions are plotted in Figure 4.14.C-D, along with their difference (β). Positive β implies volumes distributed across more edifices, while negative β indicates volume is focused around fewer vents. As expected, volcanic fields such as Caribou, Medicine Lake, and Simcoe are distributed; while areas such as Mt. Shasta and Glacier Peak are more focused (Figure 4.14.D). Vent focusing in areas otherwise dominated by distributed volcanism occurs at Mt. Mazama and Newberry volcano.

5.0 Arc-Scale Magma Transport

To characterize regional-scale spatial variability in surface volcanism, we compare maximum λ and β among epochs (Figure 4.15; Holocene included with Late Pleistocene). These temporal bins are larger than the major Cascades edifice total ages (Calvert, 2019) and so constrain transient patterns of volcanic effusion on million-year timescales.

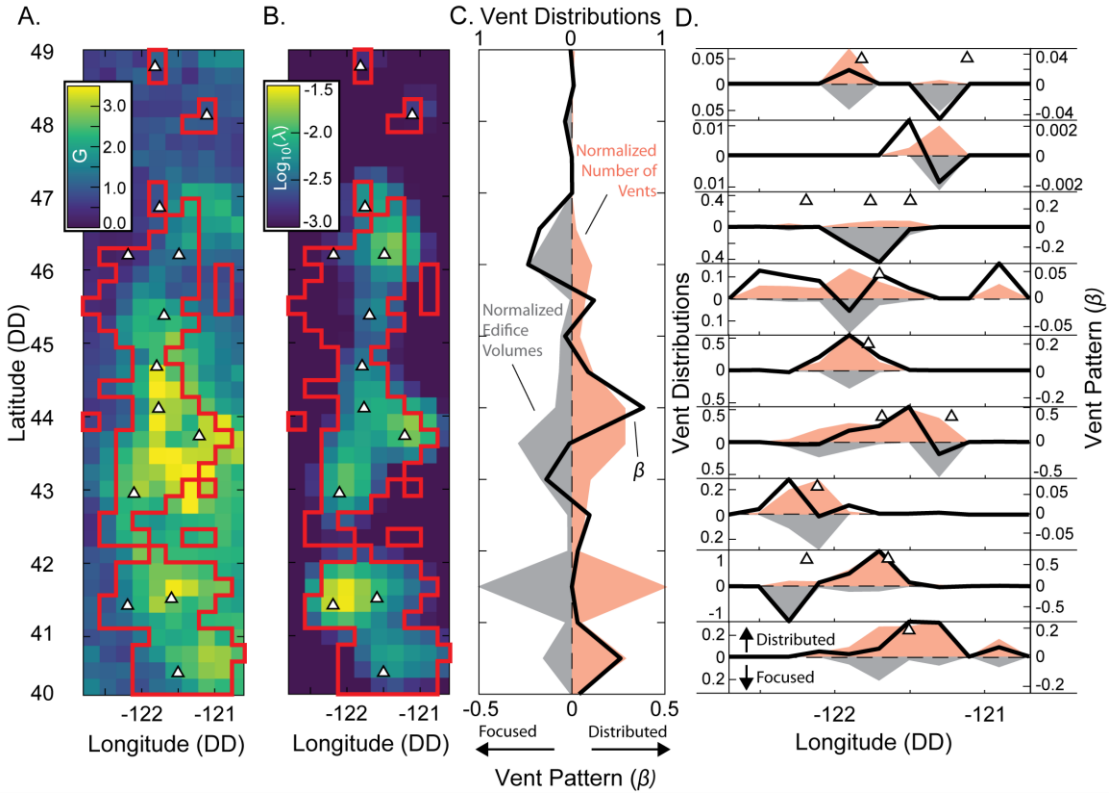

Figure 4.14 – A: Geophysical dataset correlation grid $\boldsymbol{G}$ for Quaternary vent distribution. **B:** Volume-weighted Gaussian kernel density vent distribution $\boldsymbol{\lambda}$. **C:** Along-arc normalized distributions of vent number (red shading), edifice volumes (gray shading), and their difference ($\boldsymbol{\beta}$, black line) in 0.5° latitude bins. **D:** Across-arc vent distributions in 0.2° longitude bins associated with 1.0° latitude swaths. Red lines in A-B outline cells containing vents.

Figure 4.15 indicates arc-scale patterns of volcanism style and magnitude vary throughout the Quaternary. Along-arc patterns of volcanic output are consistent between epochs (Figure 4.15.A). High λ values cluster in ≤100 km-scale areas, highlighting long-lived magmatic centers (Guffanti and Weaver, 1988; Hildreth, 2007). Although lower λ values occur in the Early Pleistocene at most of these centers, we cannot disentangle true flux variations from vent

exposure bias. However, a maximum in λ at the latitude of Lassen Peak in the Early Pleistocene likely indicates decreased eruptive output through time in that region.

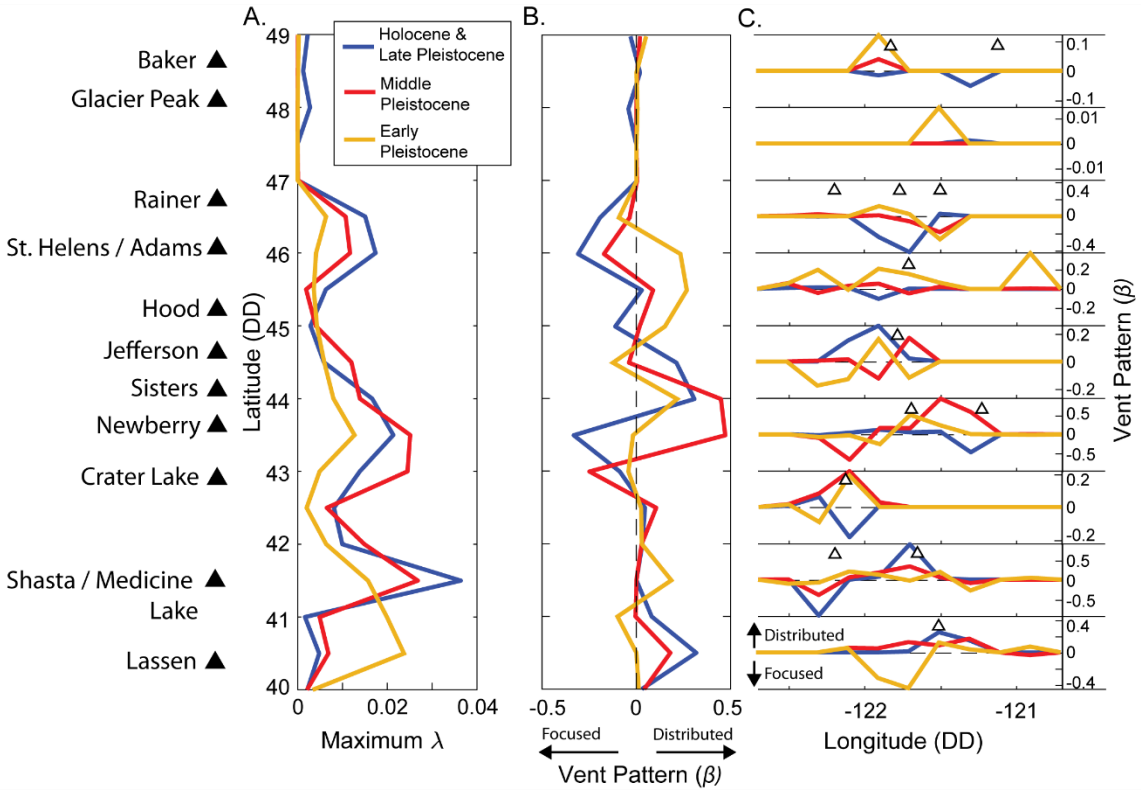

Figure 4.15 – A-B: 0.5° latitudinal bins of maximum $\boldsymbol{\lambda}$ and $\boldsymbol{\beta}$ separated by epoch. **C:** 0.2° longitudinal bins of $\boldsymbol{\beta}$ in 1.0° latitudinal swaths of the arc.

Along- and across-arc β values hint at changes in volcanic style through time (Figure 4.15.B-C). Vent patterns are not uniform throughout the arc, although a general tendency seems to be northward evolution towards more focusing. Particularly intriguing are two locations where volcanism shifts in style across the arc at the same latitude. Mt. Shasta has tended towards focused vents while Medicine Lake in the rear-arc has become more distributed through time. Exactly the opposite temporal progression is observed ~300 km north at Newberry volcano and Three Sisters. Although precise dates are lacking, both on- and off-arc axis volcanism may occur simultaneously (Germa et al., 2019).

We speculate that focusing of rising magma is a self re-enforcing process throughout the crust. Radial focusing of vents at Mt. Mazama over ~40 kyr may have been influenced by

thermomechanical feedbacks between volcano loading, pressurized magma storage zones, and rising dikes (Karlstrom et al., 2015). Such organizing processes could operate over 10s of km length scales (Pinel and Jaupart, 2000; Karlstrom et al., 2009) where such vent clustering is observed elsewhere. Tectonic extension, increasing in magnitude south and eastward along the arc (Guffanti and Weaver, 1988; Schmidt et al., 2008), should promote distributed volcanism and counterbalance focusing. Deeper variations in magma influx to the lower crust (Till et al., 2019) may also influence overlying crustal transport.

6.0 Conclusion

We demonstrate the efficacy by which edifice volumes can be remotely derived from DEMs, as well as arc-scale signatures that relate volcanism to the subsurface. Combining edifice volumes with geophysical inference of shallow crustal structure, we generate a suite of linear predictors for active magmatic transport pathways under volcanoes along with two metrics that elucidate crustal magmatic structures and spatiotemporal variations in magmatism throughout the arc. The temporal resolution and broad array of subsurface constraints compiled here thus provides a baseline for future efforts to map and model crustal magma transport in the Cascades and other volcanic provinces.

CHAPTER V

CONCLUSIONS

Bridging the fields of Geomorphology and Volcanology to analyze the relationships between processes that are often analyzed independently an unexplored corner of geoscience. My work has helped answer some of the fundamental questions related to the connections between crustal magmatism and topography. In particular, I find that 1) regional-scale crustal magmatism generates topography that encodes aspects of the deep magmatic flux; 2) localized uplift perturbations (such as those associated with magmatic intrusions) can generate transient responses on scales larger than the initial perturbation, and alter the steady-state configuration of landscapes; and 3) patterns of edifice sizes and spatial distributions reflect transient magma plumbing system development within the subsurface over million-year timescales in the Cascades arc.

Many questions remain to be explored to fully understand the correspondence between surface and subsurface processes. Does landscape evolution on the surface impact transient crustal magma system growth and configuration? Can edifice morphology be used to disentangle the processes associated with constructive and destructive processes? How do climate, tectonics, and magmatism interact in volcanic landscape development? Further work is needed to answer these questions; however, this dissertation sets a baseline for future theoretical observational studies.

REFERENCES CITED

Chapter I

Annen, C., Blundy, J. D., Leuthold, J., & Sparks, R. S. J. (2015). Construction and evolution of igneous bodies: Towards an integrated perspective of crustal magmatism. *Lithos*, 230, 206–221. https://doi.org/10.1016/j.lithos.2015.05.008

Grosse, P., van Wyk de Vries, B., Petrinovic, I. A., Euillades, P. A., & Alvarado, G. E. (2009). Morphometry and evolution of arc volcanoes. *Geology*, 37(7), 651–654. https://doi.org/10.1130/G25734A.1

Hooft, E. E. E., Nomikou, P., Toomey, D. R., Lampridou, D., Getz, C., Christopoulou, M. E., O'Hara, D., Arnoux, G. M., Bodmer, M., Gray, M., Heath, B. A., & VanderBeek, B. P. (2017). Backarc tectonism, volcanism, and mass wasting shape seafloor morphology in the Santorini-Christiana-Amorgos region of the Hellenic Volcanic Arc. *Tectonophysics*, 712–713, 396–414. https://doi.org/10.1016/j.tecto.2017.06.005

Janiszewski, H. A., Gaherty, J. B., Abers, G. A., Gao, H., & Eilon, Z. C. (2019). Amphibious surface-wave phase-velocity measurements of the Cascadia subduction zone. *Geophysical Journal International*, 217(3), 1929-1948.

Karlstrom, L., Richardson, P. W., O'Hara, D., & Ebmeier, S. K. (2018). Magmatic Landscape Construction. *Journal of Geophysical Research: Earth Surface*, 123(8), 1710–1730. https://doi.org/10.1029/2017JF004369

Priest, G. R. (1990). Volcanic and tectonic evolution of the Cascade volcanic arc, central Oregon. *Journal of Geophysical Research: Solid Earth*, 95(B12), 19583–19599.

Sherrod, D. R., & Smith, J. G. (2000). *Geologic map of upper Eocene to Holocene volcanic and related rocks of the Cascade Range, Oregon*. US Geological Survey Washington, DC.

Vanorio, T., Virieux, J., Capuano, P., & Russo, G. (2005). Three-dimensional seismic tomography from P wave and S wave microearthquake travel times and rock physics characterization of the Campi Flegrei Caldera. *Journal of Geophysical Research: Solid Earth*, 110(3), 1–14. https://doi.org/10.1029/2004JB003102

Chapter II

Anderson, R. E., Eargle, D. H., & Davis, B. O. (1973). *Geologic and Hydrologic Summary of Salt Domes in Gulf Coast Region of Texas, Louisiana, Mississippi, and Alabama*. 1–282.

Black, B. A., Perron, J. T., Hemingway, D., Bailey, E., Nimmo, F., & Zebker, H. (2017). Planetary topography: Global drainage patterns and the origins of topographic relief on Earth, Mars, and Titan. *Science*, 356(6339), 727–731. https://doi.org/10.1126/science.aag0171

Bonnet, S. (2009). Shrinking and splitting of drainage basins in orogenic landscapes from the migration of themain drainage divide. *Nature Geoscience*, 2(11), 766–771. https://doi.org/10.1038/ngeo666

Braun, J., Robert, X., & Simon-Labric, T. (2013). Eroding dynamic topography. *Geophysical Research Letters*, 40(8), 1494–1499. https://doi.org/10.1002/grl.50310

Braun, J. (2018). A review of numerical modeling studies of passive margin escarpments leading to a new analytical expression for the rate of escarpment migration velocity. *Gondwana Research*, 53, 209–224. https://doi.org/10.1016/j.gr.2017.04.012

Braun, J., & Willett, S. D. (2013). A very efficient O(n), implicit and parallel method to solve the stream power equation governing fluvial incision and landscape evolution. *Geomorphology*, 180–181, 170–179. https://doi.org/10.1016/j.geomorph.2012.10.008

Castro, J. M., Cordonnier, B., Schipper, C. I., Tuffen, H., Baumann, T. S., & Feisel, Y. (2016). Rapid laccolith intrusion driven by explosive volcanic eruption. *Nature Communications*, 7, 1–7. https://doi.org/10.1038/ncomms13585

Corry, C. E. (1988). Laccoliths: mechanics of emplacement and growth. *Geological Society of America Special Paper*, 220. https://doi.org/10.1016/0191-8141(90)90024-s

de Saint-Blanquat, M., Habert, G., Horsman, E., Morgan, S. S., Tikoff, B., Launeau, P., & Gleizes, G. (2006). Mechanisms and duration of non-tectonically assisted magma emplacement in the upper crust: The Black Mesa pluton, Henry Mountains, Utah. *Tectonophysics*, 428(1–4), 1–31. https://doi.org/10.1016/j.tecto.2006.07.014

Dibiase, R. A., Heimsath, A. M., & Whipple, K. X. (2012). Hillslope response to tectonic forcing in threshold landscapes. *Earth Surface Processes and Landforms*, 37(8), 855–865. https://doi.org/10.1002/esp.3205

Duvall, A. R., & Tucker, G. E. (2015). Journal of Geophysical Research : Earth Surface Dynamic Ridges and Valleys in a Strike-Slip Environment. *Journal of Geophysical Research: Earth Surface*, 120, 1–11. https://doi.org/10.1002/2015JF003618

Egholm, D. L., Knudsen, M. F., & Sandiford, M. (2013). Lifespan of mountain ranges scaled by feedbacks between landsliding and erosion by rivers. *Nature*, 498(7455), 475–478. https://doi.org/10.1038/nature12218

England, P., & Molnar, P. (1990). Late cenozoic uplift of mountain ranges and global climate change : chicken or egg? *Nature*, 346(July), 29–34.

Gilbert, G. K. (1877). *Geology of the Henry Mountains*.

Goren, L., Willett, S. D., Herman, F., & Braun, J. (2014). Coupled numerical-analytical approach to landscape evolution modeling. *Earth Surface Processes and Landforms*, 39(4), 522–545. https://doi.org/10.1002/esp.3514

Guzzetti, F., Ardizzone, F., Cardinali, M., Rossi, M., & Valigi, D. (2009). Landslide volumes and landslide mobilization rates in Umbria, central Italy. *Earth and Planetary Science Letters*, 279(3–4), 222–229. https://doi.org/10.1016/j.epsl.2009.01.005

Hack, J. T. (1957). Studies of longitudinal stream profiles in Virginia and Maryland. *USGS Professional Paper 249*, 97.

Harel, M. A., Mudd, S. M., & Attal, M. (2016). Global analysis of the stream power law parameters based on worldwide 10 Be denudation rates. *Geomorphology*, 268, 184–196. https://doi.org/10.1016/j.geomorph.2016.05.035

Hildreth, W. (2007). *Quaternary magmatism in the Cascades - Geologic perspectives*. US Geological Survey Professional Paper, 1744, 1–125. https://doi.org/10.3133/pp1744

Hurst, M. D., Mudd, S. M., Yoo, K., Attal, M., & Walcott, R. (2013). Influence of lithology on hillslope morphology and response to tectonic forcing in the northern Sierra Nevada of California. *Journal of Geophysical Research: Earth Surface*, 118(2), 832–851. https://doi.org/10.1002/jgrf.20049

Jaccard, P. (1901). Étude comparative de la distribution florale dans une portion des Alpes et des Jura. *Bulletin de La Société Vaudoise Des Sciences Naturelles*, 37, 547–579.

Jefferson, A., Grant, G. E., Lewis, S. L., & Lancaster, S. T. (2010). Coevolution of hydrology and topography on a basalt landscape in the Oregon Cascade Range, USA. *Earth Surface Processes and Landforms*, 35(7), 803–816. https://doi.org/10.1002/esp.1976

Karlstrom, L., Richardson, P. W., O'Hara, D., & Ebmeier, S. K. (2018). Magmatic Landscape Construction. *Journal of Geophysical Research: Earth Surface*, 123(8), 1710–1730. https://doi.org/10.1029/2017JF004369

Kirby, E., & Whipple, K. (2001). Quantifying differential rock-uplift rates via stream profile analysis. *Geology*, 29(5), 415–418.

Lague, D., Rennes, G., Rennes, U., Umr, C., & Cedex, R. (2014). The stream power river incision model: evidence, theory and beyond. *Earth Surface Processes and Landforms* 61(November 2013), 38–61. https://doi.org/10.1002/esp.3462

Larsen, I. J., & Montgomery, D. R. (2012). Landslide erosion coupled to tectonics and river incision. *Nature Geoscience*, 5(7), 468–473. https://doi.org/10.1038/ngeo1479

Mackey, B. H., Roering, J. J., & Lamb, M. P. (2011). Landslide-dammed paleolake perturbs marine sedimentation and drives genetic change in anadromous fish. *Proceedings of the National Academy of Sciences* 108(47), 18905–18909. https://doi.org/10.1073/pnas.1110445108

Mudd, S. M., & Furbish, D. J. (2005). Lateral migration of hillcrests in response to channel incision in soil-mantled landscapes. *Journal of Geophysical Research: Earth Surface*, 110(4), 1–18. https://doi.org/10.1029/2005JF000313

Nelson, S. T., & Davidson, J. P. (1997). The Petrogenesis of the Colorado Plateau Laccoliths and Their Relationship to Regional Magmatism. *Laccolith Complexes of Southeastern Utah: Time of Emplacement and Tectonic Setting - Workshop Proceedings*, C, 85–100.

Perkins, J. P., Finnegan, N. J., Henderson, S. T., & Rittenour, T. M. (2016). Topographic constraints on magma accumulation below the actively uplifting Uturuncu and Lazufre volcanic centers in the Central Andes. *Geosphere*, 12(4), 1078–1096. https://doi.org/10.1130/GES01278.1

Perron, J. T., Kirchner, J. W., & Dietrich, W. E. (2009). Formation of evenly spaced ridges and valleys. *Nature*, 460(7254), 502–505. https://doi.org/10.1038/nature08174

Perron, J. T., & Fagherazzi, S. (2012). The legacy of initial conditions in landscape evolution. *Earth Surface Processes and Landforms*, 37(1), 52–63. https://doi.org/10.1002/esp.2205

Pierson, T. C. (2009). InSAR detection of renewed movement of a large ancient land-slide in the Columbia River Gorge, Washington. *Portland GSA Annual Meeting*.

Pollard, D. D., & Johnson, A. M. (1973). Mechanics of growth of some laccolithic intrusions in the Henry mountains, Utah, II. *Tectonophysics*, 18(3–4), 311–354. https://doi.org/10.1016/0040-1951(73)90051-6

Roering, J. J., Kirchner, J. W., & Dietrich, W. E. (2001). Hillslope evolution by nonlinear, slope-dependent transport: Steady state morphology and equilibrium adjustment timescales. *Journal of Geophysical Research*, 106(B11), 26787. https://doi.org/10.1029/2001JB900018

Royden, L., & Perron, J. T. (2013). Solutions of the stream power equation and application to the evolution of river longitudinal profiles. *Journal of Geophysical Research: Earth Surface*, 118(2), 497–518. https://doi.org/10.1002/jgrf.20031

Seidl, M. A., & Dietrich, W. E. (1992). The Problem of Channel Erosion into Bedrock. *Functional Geomorphology*, 23, 101–124.

Shen, X., Anagnostou, E. N., Mei, Y., & Hong, Y. (2017). A global distributed basin morphometric dataset. *Scientific Data*, 4, 1–8. https://doi.org/10.1038/sdata.2016.124

Stock, J. D., & Montgomery, D. R. (1999). Geologic constraints on bedrock river incision using the stream power law. *Journal of Geophysical Research*, 104(B3), 4983. https://doi.org/10.1029/98JB02139

Strahler, A. N. (1957). Quantitative analysis of watershed geomorphology. *Eos, Transactions American Geophysical Union*, 38(6), 913–920. https://doi.org/10.1029/TR038i006p00913

Sweeney, K. E., Roering, J. J., Almond, P., & Reckling, T. (2012). How steady are steady-state landscapes? Using visible-near-infrared soil spectroscopy to quantify erosional variability. *Geology*, 40(9), 807–810. https://doi.org/10.1130/G33167.1

Sweetkind, D. S., & Blackwell, D. D. (1989). Fission-track evidence of the Cenozoic thermal history of the Idaho batholith. *Tectonophysics*, 157(4), 241–250. https://doi.org/10.1016/0040-1951(89)90142-X

Tucker, G. E., & Bras, R. L. (1998). Hillslope processes, drainage density, and landscape morpholog. *Water Resources Research*, 34(10), 2751–2764.

Whipple, K. X., Forte, A. M., DiBiase, R. A., Gasparini, N. M., & Ouimet, W. B. (2017). Timescales of landscape response to divide migration and drainage capture: Implications for the role of divide mobility in landscape evolution. *Journal of Geophysical Research: Earth Surface*, 122(1), 248–273. https://doi.org/10.1002/2016JF003973

Whipple, K. X., DiBiase, R. A., Ouimet, W. B., & Forte, A. M. (2017). Preservation or piracy: Diagnosing low-relief, high-elevation surface formation mechanisms. *Geology*, 45(1), 91–94. https://doi.org/10.1130/G38490.1

Whipple, K. X., & Tucker, G. E. (1999). Dynamics of the stream-power river incision model: Implications for height limits of mountain ranges, landscape response timescales, and research needs. *Journal of Geophysical Research: Solid Earth*, 104(B8), 17661–17674. https://doi.org/10.1029/1999JB900120

Wicks, C. W., Dzurisin, D., Ingebritsen, S., Thatcher, W., Lu, Z., & Iverson, J. (2002). Magmatic activity beneath the quiescent Three Sisters volcanic center, central Oregon Cascade Range, USA. *Geophysical Research Letters*, 29(7), 26-1-26–4. https://doi.org/10.1029/2001GL014205

Wilkinson, B. H., McElroy, B. J., Kesler, S. E., Peters, S. E., & Rothman, E. D. (2009). Global geologic maps are tectonic speedometers - Rates of rock cycling from area-age frequencies. *Bulletin of the Geological Society of America*, 121(5–6), 760–779. https://doi.org/10.1130/B26457.1

Willett, S. D. (2010). Erosion on a line. *Tectonophysics*, 484(1–4), 168–180. https://doi.org/10.1016/j.tecto.2009.09.011

Willett, S. D., & Brandon, M. T. (2002). On steady states in mountain belts. *Geology*, 30(2), 175–178. https://doi.org/10.1130/0091-7613(2002)030<0175:OSSIMB>2.0.CO;2

Willett, S. D., McCoy, S. W., Taylor Perron, J., Goren, L., & Chen, C. Y. (2014). Dynamic reorganization of River Basins. *Science*, 343(6175). https://doi.org/10.1126/science.1248765

Yang, R., Willett, S. D., & Goren, L. (2015). In situ low-relief landscape formation as a result of river network disruption. *Nature*, 520(7548), 526–529. https://doi.org/10.1038/nature14354

Chapter III

Annen, C., & Sparks, R. S. J. (2002). Effects of repetitive emplacement of basaltic intrusions on thermal evolution and melt generation in the crust. *Earth and Planetary Science Letters*, 203(3–4), 937–955. https://doi.org/10.1016/S0012-821X(02)00929-9

Annen, C., Blundy, J. D., Leuthold, J., & Sparks, R. S. J. (2015). Construction and evolution of igneous bodies: Towards an integrated perspective of crustal magmatism. *Lithos*, 230, 206–221. https://doi.org/10.1016/j.lithos.2015.05.008

Annen, C., Blundy, J. D., & Sparks, R. S. J. (2006). The genesis of intermediate and silicic magmas in deep crustal hot zones. *Journal of Petrology*, 47(3), 505–539. https://doi.org/10.1093/petrology/egi084

Baloga, S. M., Glaze, L. S., & Bruno, B. C. (2007). Nearest-neighbor analysis of small features on Mars: Applications to tumuli and rootless cones. *Journal of Geophysical Research: Planets*, 112(3), 1–17. https://doi.org/10.1029/2005JE002652

Blakely, R. J., Christiansen, R. L., Guffanti, M., Wells, R. E., Donnelly-Nolan, J. M., Muffler, L. J. P., Clynne, M. A., & Smith, J. G. (1997). Gravity anomalies, Quaternary vents, and Quaternary faults in the southern Cascade Range, Oregon and California: Implications for arc and backarc evolution. *Journal of Geophysical Research: Solid Earth*, 102(B10), 22513–22527.

Cashman, K. V., & Giordano, G. (2014). Calderas and magma reservoirs. *Journal of Volcanology and Geothermal Research*, 288, 28–45. https://doi.org/10.1016/j.jvolgeores.2014.09.007

Cashman, K. V., Sparks, R. S. J., & Blundy, J. D. (2017). Vertically extensive and unstable magmatic systems: A unified view of igneous processes. *Science*, 355(6331). https://doi.org/10.1126/science.aag3055

Castro, J. M., Cordonnier, B., Schipper, C. I., Tuffen, H., Baumann, T. S., & Feisel, Y. (2016). Rapid laccolith intrusion driven by explosive volcanic eruption. *Nature Communications*, 7, 1–7. https://doi.org/10.1038/ncomms13585

Connor, C. B., & Hill, B. E. (1995). Three nonhomogeneous Poisson models for the probability of basaltic volcanism: application to the Yucca Mountain region, Nevada. *Journal of Geophysical Research*, 100(B6). https://doi.org/10.1029/95jb01055

Cruden, A. R., McCaffrey, K. J. W., & Bunger, A. P. (2017). Geometric Scaling of Tabular Igneous Intrusions: Implications for Emplacement and Growth. In Advances in Volcanology (pp. 11–38). https://doi.org/10.1007/11157_2017_1000

de Saint-Blanquat, M., Habert, G., Horsman, E., Morgan, S. S., Tikoff, B., Launeau, P., & Gleizes, G. (2006). Mechanisms and duration of non-tectonically assisted magma emplacement in the upper crust: The Black Mesa pluton, Henry Mountains, Utah. *Tectonophysics*, 428(1–4), 1–31. https://doi.org/10.1016/j.tecto.2006.07.014

De Saint Blanquat, M., Horsman, E., Habert, G., Morgan, S., Vanderhaeghe, O., Law, R., & Tikoff, B. (2011). Multiscale magmatic cyclicity, duration of pluton construction, and the paradoxical relationship between tectonism and plutonism in continental arcs. *Tectonophysics*, 500(1–4), 20–33. https://doi.org/10.1016/j.tecto.2009.12.009

Dufek, J., & Bergantz, G. W. (2005). Lower crustal magma genesis and preservation: A stochastic framework for the evaluation of basalt-crust interaction. *Journal of Petrology*, 46(11), 2167–2195. https://doi.org/10.1093/petrology/egi049

Ferrier, K. L., Huppert, K. L., & Perron, J. T. (2013). Climatic control of bedrock river incision. *Nature*, 496(7444), 206–209. https://doi.org/10.1038/nature11982

Fialko, Y., Khazan, Y., & Simons, M. (2001). Deformation due to a pressurized horizontal circular crack in an elastic half-space, with applications to volcano geodesy. *Geophysical Journal International*, 146(1), 181–190. https://doi.org/10.1046/j.1365-246X.2001.00452.x

Galland, O., & Scheibert, J. (2013). Analytical model of surface uplift above axisymmetric flat-lying magma intrusions: Implications for sill emplacement and geodesy. *Journal of Volcanology and Geothermal Research*, 253, 114–130. https://doi.org/10.1016/j.jvolgeores.2012.12.006

Gilbert, G. K. (1877). *Geology of the Henry Mountains*.

Goulty, N. R., & Schofield, N. (2008). Implications of simple flexure theory for the formation of saucer-shaped sills. *Journal of Structural Geology*, 30(7), 812–817. https://doi.org/10.1016/j.jsg.2008.04.002

Hayes, S. K., Montgomery, D. R., & Newhall, C. G. (2002). Fluvial sediment transport and deposition following the 1991 eruption of Mount Pinatubo. *Geomorphology*, 45(3–4), 211–224. https://doi.org/10.1016/S0169-555X(01)00155-6

Hildreth, W. (2007). *Quaternary magmatism in the Cascades - Geologic perspectives*. US Geological Survey Professional Paper, 1744, 1–125. https://doi.org/10.3133/pp1744

Jackson, M. D., & Pollard, D. D. (1988). The laccolith-stock controversy: New results from the southern Henry Mountains, Utah. *Bulletin of the Geological Society of America*, 100(1), 117–139. https://doi.org/10.1130/0016-7606(1988)100<0117:TLSCNR>2.3.CO;2

Jefferson, A., Grant, G. E., Lewis, S. L., & Lancaster, S. T. (2010). Coevolution of hydrology and topography on a basalt landscape in the Oregon Cascade Range, USA. *Earth Surface Processes and Landforms*, 35(7), 803–816. https://doi.org/10.1002/esp.1976

Jellinek, A. M., Manga, M., & Saar, M. O. (2004). Did melting glaciers cause volcanic eruptions in eastern California? Probing the mechanics of dike formation. *Journal of Geophysical Research: Solid Earth*, 109(9), 1–10. https://doi.org/10.1029/2004JB002978

Karlstrom, L., Dufek, J., & Manga, M. (2010). Magma chamber stability in arc and continental crust. *Journal of Volcanology and Geothermal Research*, 190(3–4), 249–270. https://doi.org/10.1016/j.jvolgeores.2009.10.003

Karlstrom, L., Paterson, S. R., & Jellinek, A. M. (2017). A reverse energy cascade for crustal magma transport. *Nature Geoscience*, 10(8), 604–608. https://doi.org/10.1038/NGEO2982

Karlstrom, L., Richardson, P. W., O'Hara, D., & Ebmeier, S. K. (2018). Magmatic Landscape Construction. *Journal of Geophysical Research: Earth Surface*, 123(8), 1710–1730. https://doi.org/10.1029/2017JF004369

Karlstrom, L., Wright, H. M., & Bacon, C. R. (2015). The effect of pressurized magma chamber growth on melt migration and pre-caldera vent locations through time at Mount Mazama, Crater Lake, Oregon. *Earth and Planetary Science Letters*, 412, 209–219.

Krishna, M. R. (1996). Isostatic response of the Central Indian Ridge (Western Indian Ocean) based on transfer function analysis of gravity and bathymetry data. *Tectonophysics*, 257(2-4 SPEC. ISS.), 137–148. https://doi.org/10.1016/0040-1951(95)00114-x

Maccaferri, F., Bonafede, M., & Rivalta, E. (2011). A quantitative study of the mechanisms governing dike propagation, dike arrest and sill formation. *Journal of Volcanology and Geothermal Research*, 208(1–2), 39–50. https://doi.org/10.1016/j.jvolgeores.2011.09.001

Maccaferri, F., Rivalta, E., Keir, D., & Acocella, V. (2014). Off-rift volcanism in rift zones determined by crustal unloading. *Nature Geoscience*, 7(4), 297–300. https://doi.org/10.1038/ngeo2110

McGuire, L. A., Pelletier, J. D., & Roering, J. J. (2014). Development of topographic asymmetry: Insights from dated cinder cones in the western United States. *Journal of Geophysical Research: Earth Surface*, 119(8), 1725–1750.

McNutt, M. K. (1983). Influence of plate subduction on isostatic compensation in northern California. *Tectonics*, 2(4), 399–415. https://doi.org/10.1029/TC002i004p00399

McTigue, D. F. (1987). Elastic stress and deformation near a finite spherical magma body: Resolution of the point source paradox. *Journal of Geophysical Research*, 92(B12), 12931. https://doi.org/10.1029/jb092ib12p12931

McTigue, D. F., & Stein, R. S. (1984). Topographic amplification of tectonic displacement: implications for geodetic measurement of strain changes. *Journal of Geophysical Research*, 89(B2), 1123–1131. https://doi.org/10.1029/JB089iB02p01123

Michaut, C. (2011). Dynamics of magmatic intrusions in the upper crust: Theory and applications to laccoliths on Earth and the Moon. *Journal of Geophysical Research*, 116(B5), B05205. https://doi.org/10.1029/2010JB008108

Mogi, K. (1958). Relations between the eruptions of various volcanoes and the deformations of the ground surfaces around them. *Bulletin of the Earthquake Research Institute* (36), 99–134. https://doi.org/10.1016/j.epsl.2004.04.016

Morriss, M. C., Karlstrom, L., Nasholds, M. W. M., & Wolff, J. A. (2020). The chief Joseph dike swarm of the Columbia river flood basalts, and the legacy data set of William H. Taubeneck. *Geosphere*, 16(4), 1793–1817. https://doi.org/10.1130/GES02173.1

O'Hara, D., Karlstrom, L., & Ramsey, D. W. (2020). Time-evolving surface and subsurface signatures of Quaternary volcanism in the Cascades arc. *Geology*. https://doi.org/10.1130/g47706.1

O'Hara, D., Karlstrom, L., & Roering, J. J. (2019). Distributed landscape response to localized uplift and the fragility of steady states. *Earth and Planetary Science Letters*, 506, 243–254.

Parks, M. M., Moore, J. D. P., Papanikolaou, X., Biggs, J., Mather, T. A., Pyle, D. M., Raptakis, C., Paradissis, D., Hooper, A., Parsons, B., & Nomikou, P. (2015). From quiescence to unrest: 20 years of satellite geodetic measurements at Santorini volcano, Greece. *Journal of Geophysical Research: Solid Earth*, 120(2), 1309–1328. https://doi.org/10.1002/2014JB011540

Perkins, J. P., Ward, K. M., De Silva, S. L., Zandt, G., Beck, S. L., & Finnegan, N. J. (2016). Surface uplift in the Central Andes driven by growth of the Altiplano Puna Magma Body. *Nature Communications*, 7, 1–10. https://doi.org/10.1038/ncomms13185

Pollard, D. D., & Johnson, A. M. (1973). Mechanics of growth of some laccolithic intrusions in the Henry mountains, Utah, II. *Tectonophysics*, 18(3–4), 311–354. https://doi.org/10.1016/0040-1951(73)90051-6

Ramsey, D. W., & Siebert, L. (2017). Spatial and Temporal Database Compilation of Holocene Volcanic Vents in the Western Conterminous United States. *IAVCEI Scientific Assembly Abstracts*.

Rivalta, E., Taisne, B., Bunger, A. P., & Katz, R. F. (2015). A review of mechanical models of dike propagation: Schools of thought, results and future directions. *Tectonophysics*, 638(C), 1–42. https://doi.org/10.1016/j.tecto.2014.10.003

Schmidt, M. E., Grunder, A. L., & Rowe, M. C. (2008). Segmentation of the Cascade Arc as indicated by Sr and Nd isotopic variation among diverse primitive basalts. *Earth and Planetary Science Letters*, 266(1–2), 166–181.

Sparks, R. S. J., Annen, C., Blundy, J. D., Cashman, K. V., Rust, A. C., & Jackson, M. D. (2019). Formation and dynamics of magma reservoirs. *Philosophical Transactions of the Royal Society A: Mathematical, Physical and Engineering Sciences*, 377(2139). https://doi.org/10.1098/rsta.2018.0019

Sternai, P., Caricchi, L., Castelltort, S., & Champagnac, J. D. (2016). Deglaciation and glacial erosion: A joint control on magma productivity by continental unloading. *Geophysical Research Letters*, 43(4), 1632–1641. https://doi.org/10.1002/2015GL067285

Tibaldi, A. (2015). Structure of volcano plumbing systems: A review of multi-parametric effects. *Journal of Volcanology and Geothermal Research*, 298, 85–135. https://doi.org/10.1016/j.jvolgeores.2015.03.023

Till, C. B., Kent, A. J. R., Abers, G. A., Janiszewski, H. A., Gaherty, J. B., & Pitcher, B. W. (2019). The causes of spatiotemporal variations in erupted fluxes and compositions along a volcanic arc. *Nature Communications*, 10(1), 1350.

Turcotte, D. L., & Schubert, G. (2010). *Geodynamics* (2nd ed.). Cambridge University Press.

Walcott, R. I. (1970). Isostatic response to loading of the crust in Canada. *Canadian Journal of Earth Sciences*, 7(2), 716–727. https://doi.org/10.1139/e70-070

Wessel, P. (1996). Analytical solutions for 3-D flexural deformation of semi-infinite elastic plates. *Geophysical Journal International*, 124(3), 907–918. https://doi.org/10.1111/j.1365-246X.1996.tb05644.x

White, S. M., Crisp, J. A., & Spera, F. J. (2006). Long-term volumetric eruption rates and magma budgets. *Geochemistry, Geophysics, Geosystems*, 7(3). https://doi.org/10.1029/2005GC001002

Wilkinson, B. H., McElroy, B. J., Kesler, S. E., Peters, S. E., & Rothman, E. D. (2009). Global geologic maps are tectonic speedometers - Rates of rock cycling from area-age frequencies. *Bulletin of the Geological Society of America*, 121(5–6), 760–779. https://doi.org/10.1130/B26457.1

Williams, C. A., & Wadge, G. (1998). The effects of topography on magma chamber deformation models: Application to Mt. Etna and radar interferometry. *Geophysical Research Letters*, 25(10), 1549–1552. https://doi.org/10.1029/98GL01136

Chapter IV

Bacon, C. R., & Lanphere, M. A. (2006). Eruptive history and geochronology of Mount Mazama and the Crater Lake region, Oregon. *Bulletin of the Geological Society of America*, 118(11–12), 1331–1359. https://doi.org/10.1130/B25906.1

Blakely, R. J., Christiansen, R. L., Guffanti, M., Wells, R. E., Donnelly-Nolan, J. M., Muffler, L. J. P., Clynne, M. A., & Smith, J. G. (1997). Gravity anomalies, Quaternary vents, and Quaternary faults in the southern Cascade Range, Oregon and California: Implications for arc and backarc evolution. *Journal of Geophysical Research: Solid Earth*, 102(B10), 22513–22527.

Bohnenstiehl, D. R., Howell, J. K., White, S. M., & Hey, R. N. (2012). A modified basal outlining algorithm for identifying topographic highs from gridded elevation data, Part 1: Motivation and methods. *Computers & Geosciences*, 49, 308–314.

Calvert, A. T. (2019). Inception ages, growth spurts, and lifespans of Cascade Arc volcanoes. *AGU Fall Meeting Abstracts*.

Cao, W., Paterson, S., Saleeby, J., & Zalunardo, S. (2016). Bulk arc strain, crustal thickening, magma emplacement, and mass balances in the Mesozoic Sierra Nevada arc. *Journal of Structural Geology*, 84, 14–30. https://doi.org/10.1016/j.jsg.2015.11.002

Clynne, M. A., & Muffler, L. J. P. (2010). Geologic Map of Lassen Volcanic National Park and Vicinity, California. In *Scientific Investigations Map*.

Deng, F., Connor, C. B., Malservisi, R., Connor, L. J., White, J. T., Germa, A., & Wetmore, P. H. (2017). A Geophysical Model for the Origin of Volcano Vent Clusters in a Colorado Plateau Volcanic Field. *Journal of Geophysical Research: Solid Earth*, 122(11), 8910–8924. https://doi.org/10.1002/2017JB014434

du Bray, E. A., & John, D. A. (2011). Petrologic, tectonic, and metallogenic evolution of the Ancestral Cascades magmatic arc, Washington, Oregon, and northern California. *Geosphere*, 7(5), 1102–1133. https://doi.org/10.1130/GES00669.1

Euillades, L. D., Grosse, P., & Euillades, P. A. (2013). NETVOLC: An algorithm for automatic delimitation of volcano edifice boundaries using DEMs. *Computers and Geosciences*, 56(July), 151–160. https://doi.org/10.1016/j.cageo.2013.03.011

George, O. A., Malservisi, R., Govers, R., Connor, C. B., & Connor, L. J. (2016). Is uplift of volcano clusters in the Tohoku Volcanic Arc, Japan, driven by magma accumulation in hot zones? A geodynamic modeling study. *Journal of Geophysical Research: Solid Earth*, 121(6), 4780–4796. https://doi.org/10.1002/2016JB012833

Germa, A., Perry, C., Quidelleur, X., Calvert, A., Clynne, M., Connor, C. B., Connor, L. J., Malservisi, R., & Charbonnier, S. (2019). Temporal relationship between the Lassen volcanic center and mafic regional volcanism. *Bulletin of Volcanology*, 81(7). https://doi.org/10.1007/s00445-019-1296-7

Grosse, P., Euillades, P. A., Euillades, L. D., & van Wyk de Vries, B. (2014). A global database of composite volcano morphometry. *Bulletin of Volcanology*, 76(1), 1–16. https://doi.org/10.1007/s00445-013-0784-4

Guffanti, M., & Weaver, C. S. (1988). Distribution of late Cenozoic volcanic vents in the Cascade Range: Volcanic arc segmentation and regional tectonic considerations. *Journal of Geophysical Research: Solid Earth*, 93(B6), 6513–6529.

Hildreth, W. (2007). *Quaternary magmatism in the Cascades - Geologic perspectives*. US Geological Survey Professional Paper, 1744, 1–125. https://doi.org/10.3133/pp1744

Hildreth, W., Fierstein, J., & Calvert, A. (2012). Geologic map of the Three Sisters volcanic clusters, Cascade Range, Oregon. *U.S. Geol. Surv. Scientific Investigations Map*, 3186, 3186.

Ingebritsen, S. E., & Mariner, R. H. (2010). Hydrothermal heat discharge in the Cascade Range, northwestern United States. *Journal of Volcanology and Geothermal Research*, 196(3–4), 208–218.

Ito, G., & Martel, S. J. (2002). Focusing of magma in the upper mantle through dike interaction. *Journal of Geophysical Research: Solid Earth*, 107(B10), ECV 6-1-ECV 6-17. https://doi.org/10.1029/2001jb000251

Janiszewski, H. A., Gaherty, J. B., Abers, G. A., Gao, H., & Eilon, Z. C. (2019). Amphibious surface-wave phase-velocity measurements of the Cascadia subduction zone. *Geophysical Journal International*, 217(3), 1929-1948.

Karlstrom, L., Lee, C. T. A., & Manga, M. (2014). The role of magmatically driven lithospheric thickening on arc front migration. *Geochemistry, Geophysics, Geosystems*, 15(6), 2655–2675. https://doi.org/10.1002/2014GC005355

Karlstrom, L., Dufek, J., & Manga, M. (2009). Organization of volcanic plumbing through magmatic lensing by magma chambers and volcanic loads. *Journal of Geophysical Research: Solid Earth*, 114(10), 1–16. https://doi.org/10.1029/2009JB006339

Karlstrom, L., Wright, H. M., & Bacon, C. R. (2015). The effect of pressurized magma chamber growth on melt migration and pre-caldera vent locations through time at Mount Mazama, Crater Lake, Oregon. *Earth and Planetary Science Letters*, 412, 209–219.

Kucks, R. P. (1999). *Isostatic residual gravity anomaly data grid for the conterminous US*.

Kutner, M. H., Nachtsheim, C. J., Neter, J., & Li, W. (2005). *Applied Linear Statistics Models* (5th ed.). McGraw-Hill/Irwin.

McCaffrey, R., King, R. W., Payne, S. J., & Lancaster, M. (2013). Active tectonics of northwestern US inferred from GPS-derived surface velocities. *Journal of Geophysical Research: Solid Earth*, 118(2), 709–723.

Perron, J. T., Kirchner, J. W., & Dietrich, W. E. (2008). Spectral signatures of characteristic spatial scales and nonfractal structure in landscapes. *Journal of Geophysical Research: Earth Surface*, 113(4), 1–14. https://doi.org/10.1029/2007JF000866

Pinel, V., & Jaupart, C. (2000). The effect of edifice load on magma ascent beneath a volcano. *Philosophical Transactions of the Royal Society A: Mathematical, Physical and Engineering Sciences*, 358(1770), 1515–1532. https://doi.org/10.1098/rsta.2000.0601

Ramsey, D. W., & Siebert, L. (2017). Spatial and Temporal Database Compilation of Holocene Volcanic Vents in the Western Conterminous United States. *IAVCEI Scientific Assembly Abstracts*.

Schmidt, M. E., Grunder, A. L., & Rowe, M. C. (2008). Segmentation of the Cascade Arc as indicated by Sr and Nd isotopic variation among diverse primitive basalts. *Earth and Planetary Science Letters*, 266(1–2), 166–181.

Sherrod, D. R., & Smith, J. G. (1990). Quaternary extrusion rates of the Cascade Range, northwestern United States and southern British Columbia. *Journal of Geophysical Research*, 95(B12), 94–103.

Sherrod, D. R., & Smith, J. G. (2000). *Geologic map of upper Eocene to Holocene volcanic and related rocks of the Cascade Range, Oregon*. US Geological Survey Washington, DC.

Simpson, R. W., Jachens, R. C., Saltus, R. W., & Blakely, R. J. (1985). A new isostatic residual gravity map of the conterminous United States. *1985 SEG Annual Meeting*, SEG 1985, 91(5), 197–198. https://doi.org/10.1190/1.1892727

Tamura, Y., Tatsumi, Y., Zhao, D., Kido, Y., & Shukuno, H. (2002). Hot fingers in the mantle wedge: New insights into magma genesis in subduction zones. *Earth and Planetary Science Letters*, 197(1–2), 105–116. https://doi.org/10.1016/S0012-821X(02)00465-X

Till, C. B., Kent, A. J. R., Abers, G. A., Janiszewski, H. A., Gaherty, J. B., & Pitcher, B. W. (2019). The causes of spatiotemporal variations in erupted fluxes and compositions along a volcanic arc. *Nature Communications*, 10(1), 1350.

U.S.G.S. (2013). *The National Elevation Dataset*.

Weaver, C. S., Blackwell, D. D., & Jacobson, M. L. (1989). *Proceedings of workshop XLIV; geological, geophysical, and tectonic setting of the Cascade Range* (L. J. P. Muffler (ed.)). https://doi.org/10.3133/ofr89178

Wells, R.E., Weaver, C. S., & Blakely, R. J. (1998). Fore-arc migration in Cascadia and its neotectonic significance. *Geology*, 26(8), 759–762. https://doi.org/10.1130/0091-7613(1998)026<0759:FAMICA>2.3.CO;2

Wells, R. E., & McCaffrey, R. (2013). Steady rotation of the Cascade arc. *Geology*, 41(9), 1027–1030. https://doi.org/10.1130/G34514.1

Zhao, D., Hasegawa, A., & Horiuchi, S. (1992). Tomographic imaging of P and S wave velocity structure beneath northeastern Japan. *Journal of Geophysical Research*, 97(B13). https://doi.org/10.1029/92jb00603